

MULTIMODE OPTICAL FIBER BRAGG GRATINGS

MULTIMODE OPTICAL FIBER BRAGG GRATINGS: MODELING , SIMULATION AND EXPERIMENTS

By

**JINSONG ZHANG,
Ph.D., M.Sc., B.Sc., Physics**

A Thesis

Submitted to the School of Graduate Studies

in Partial Fulfillment of the Requirements

for the Degree

Master of Applied Science

McMaster University

© Copyright by Jinsong Zhang, May 2004

MASTER OF APPLIED SCIENCE (2004)

McMaster University

(Electrical and Computer Engineering)

Hamilton, Ontario

**TITLE: Multimode Optical Fiber Bragg Gratings:
Modeling, Simulation and Experiments**

**AUTHOR: Jinsong Zhang, Ph.D. (Institute of Plasma Physics,
Chinese Academy of Sciences)
M.Sc. (Institute of Plasma Physics,
Chinese Academy of Sciences)
B.Sc. (Chengdu University of Science
and Engineering)**

SUPERVISOR: Prof. Wei Ping Huang (Electrical & Computer Engineering)

CO-SUPERVISOR: Prof. Chang Qing Xu (Engineering Physics)

NUMBER OF PAGES: xiv, 164

Abstract

Telecommunication networks based on optical fiber technology have become a major information-transmission system, satisfying the growing demand for bandwidth due to increased internet traffic and other applications such as video on demand, etc. Fiber Bragg gratings (FBGs), in recent years, have emerged as critical components for enabling high-capacity transmission since their response can be tailored to meet the needs of specific applications. FBGs are currently the focus of intense research interest in both the fiber communications and sensing fields.

Optical fiber Bragg grating structures in single-mode fiber (SMFBGs) have been studied extensively since the discovery of photosensitivity in germanium-doped silica fiber. They have been used in numerous applications ranging from wavelength-selective filtering in wavelength-division-multiple-access (WDMA) systems to temperature and strain sensing. To a lesser extent, Bragg gratings in multimode fibers have also received attention because of easy coupling with light sources. Most of the MMFBGs related research work has demonstrated the formation of a Bragg grating in a graded-index MMF and briefly reported the measured transmission spectrum. So far, there are few theoretical studies on Bragg gratings in multimode fibers.

In this thesis, we investigate Bragg gratings in multimode optical fibers both theoretically and experimentally. A comprehensive numerical model for MMFBGs has been established and the corresponding computer simulation software (MMFBG simulator combined with mode solver) developed. The optical properties of MMFBGs were systematically studied for the first time using our own MMFBG numerical software package. It effectively assists the design modeling for MMFBG-based optical devices. Bragg gratings in multimode fiber were also investigated experimentally. Our theoretical simulation results show good agreement with experiments and offer the insightful explanations for the underlying physics of the device.

First, the guided modes were modeled and simulated for step index multimode fibers and graded index multimode fibers with emphasis on parabolic fiber structure. These are popular, standard and commercially available MM fibers, and employed throughout our

experiments. This allows us for the simulation of fiber characteristics such as cut-off wavelength, mode effective index, propagation constants and optical field distribution. It also allows for calculation of mode coupling coefficients by overlap integral between any chosen guided modes. Therefore, it serves as a powerful model for the design and analysis of optical fibers.

Second, the generalized MMFBG coupled mode theory formalism is derived. The physical mechanism of the behavior of MMFBGs is studied and discussed. The general solution to the MMF Bragg grating problem is achieved by Runge-Kutta, Newton-Raphson and shooting numerical methods. Our theoretical treatment, in particular, offers the advantages which can deal with not only self-coupling but also more complicated cross-coupling interactions and can solve arbitrary large number of mode coupling problems throughout the entire spectra simultaneously for multimode FBGs, thus allowing for a precise and quantitative study of MMFBGs. Such an intensive multimode fiber Bragg grating physical modeling and simulations have not been reported previously. It provides an effective means for the design and analysis of optical fiber devices based on Bragg gratings.

Third, the optical properties of multimode FBGs were studied experimentally. Numerical predications of the grating spectral characteristics under fabrication and experimental condition are calculated. The results of the numerical calculations are compared with experimentally measured spectra of multimode gratings written by ultraviolet irradiation of deuterium-sensitized fiber with grating reflectivities ranging from 78% to 99.39%. Good agreement is obtained between the theoretical simulations and the experimental results. Thus, we provide quantitative explanations for the observed experimental phenomena. These explanations give both physical insight and a more complete understanding of the nature of the interaction between the wave propagation and multimode fiber gratings. Furthermore, the spectral simulation of the actual experiments prepares a theoretical guidance for the advanced experimental investigation and also presents a step toward MMFBG device design.

Finally, the optical properties of MMFBGs were also studied theoretically. To our knowledge, this is the first detailed analysis and thorough investigation on grating characteristics in MMF. It is demonstrated that the transmission and reflection spectra of

fiber Bragg gratings in multimode optical fibers strongly depend on the length of grating, index modulation, period of grating, mode excitation condition and physical structure of MMF. The simulation results allow us to deeply comprehend and visualize the more sophisticated behavior within a multimode fiber grating, and will also allow us to confidently predict and evaluate the performance of more complex structure MMFBGs. It provides the fundamental principles for designing the targeted spectrum performance and settles the theoretical rationale for realizing the practical applications.

Overall, the comprehensive numerical model and MMFBG solver package developed in this thesis opens a clear and broad window for understanding MMFBG mechanisms from the physical point of view. Various simulation results and spectral characteristics have been researched and discussed under both ideal and experimental conditions for the purpose of experimental analysis and device design. The results of our study indicate that a new class of potential applications based on MMFBGs can be expected in optical fiber sensors and advanced communication systems.

Key Words: Multimode Fiber Bragg Grating (MMFBG), Multimode Fiber (MMF), Coupled Mode Theory (CMT), Optical Characteristics, Optical Fiber Communications.

Acknowledgements

First of all, I gratefully acknowledge the continuous support, guidance and understanding during this time provided by my supervisor Dr. Weiping Huang and my co-supervisor Dr. Changqing Xu without whom this work would not have been possible. Dr. Huang and Dr. Xu's broad knowledge and erudite wisdom, serious research attitude and excellent academic insight, as well their great supervising me in both theoretical and experimental fields were essential to the completion of this work and will inevitably benefit me in my whole life. I am deeply indebted to my supervisors: Dr. Huang and Dr. Xu.

In particular, I am greatly appreciative of Dr. Xun Li for sharing his extensive physical brilliance and abundant experience; and also, for his enthusiasm and encouragement throughout this work.

Part of the research has been carried out in collaboration with Engineering Physics Department. I am especially grateful to Honggang Yu for fruitful collaboration working with FBG's experiments. I am also very grateful to Dr. Yong Wang and Jian Yang for constructive suggestion on experiments and Mr. Matthew. D. Minnick for his kindly help.

A special thank to Dr. Gengxiang Cheng, Chengling Xu, Yu Chen, Linping Sheng, Ningning Feng and Rona Zhou for their extremely inspiring and valuable discussions, as well as their generous assistance.

In addition, I also thank all my fellow office-mates and friends at both photonics research groups of ECE and Engineering Physics Departments for interesting discussions all these years.

The last but not the least, I would like to extend my sincere gratitude to the personnel in the Department of Electrical and Computer Engineering.

Thanks a bunch everybody who has given me kind help and concern.

TABLE OF CONTENTS

ABSTRACT	iii
ACKNOWLEDGEMENTS	vi
CHAPTER ONE: INTRODUCTION	1
1.1 General Description	1
1.2 Thesis Motivation and Objectives	4
1.3 Organizational Outline	7
CHAPTER TWO: INTRODUCTION TO FIBER BRAGG GRATINGS	10
2.1 Basic Concepts	10
2.2 Brief Historical Perspective	12
2.3 Types of Fiber Gratings	14
2.4 Basic Theory of FBGs - Coupled Mode Theory	17
2.5 Applications of Fiber Bragg Gratings	22
2.6 Summary	27
CHAPTER THREE: MODELING AND SIMULATION OF GUIDED MODES IN OPTICAL FIBERS	28
3.1 Mode Modeling and Simulation for Step Index Fibers	29
3.1.1 Maxwell's Equations	29
3.1.2 The Scalar Wave Equation for the Modal Fields	30
3.1.3 The Eigenvalue Equation for Propagation Constants	32
3.1.4 Numerical Implementation and Simulation Results	34
3.1.5 Fractional Modal Power in the Core	40
3.2 Mode Modeling and Simulation for Graded Index Fibers	42
3.2.1 Modal Analysis of Parabolic Index Fibers	43
3.2.2 Linearly Polarized Modes	46
3.2.3 Computer Simulation and Results Discussion	47
3.2.4 Excitation of Guided Modes	53
3.3 Summary	54
CHAPTER FOUR: MODELING AND SIMULATION OF FBGS IN MULTIMODE FIBER STRUCTURES	56
4.1 Establishment of Coupled-Mode Theory Formulations for MMFBGs	57
4.1.1 General Coupled Mode Equations	58
4.1.2 Bragg Gratings in Multimode Fibers — Part I. Electromagnet Derivations of the CMT formulations for Independent Mode MMFBG	61
4.1.3 Bragg Gratings in Multimode Fibers — Part II. Electromagnetic Derivations of the CMT formulations for Mode coupling MMFBG	67
4.2 Applied Numerical Computation Methods for MMFBGs	73
4.2.1 Runge-Kutta Method for Solving Initial Value Problems	74
4.2.2 Shooting Method for Solving Boundary Value Problems	75

4.2.3 Newton-Raphson Method for Constructing Shooting Algorithm	77
4.3 Solution of the Coupled Mode Equations for MMFBGs	79
4.4 Model Validation and Physical Interpretation	84
4.5 Summary	88
CHAPTER FIVE: EXPERIMENTAL STUDY AND ANALYSIS FOR MMFBGS	91
5.1 Experimental Setup	91
5.2 Experimental Results	92
5.3 Modeling and Simulation for Experiments	93
5.3.1 Mode Construction	94
5.3.2 FBG Spectral Response Simulation	95
5.4 Comparison and Discussion	96
5.5 Current Limitations and Future Experiments	107
5.6 Summary	110
CHAPTER SIX: THEORETICAL INVESTIGATION OF OPTICAL CHARACTERISTICS FOR MMFBGS	112
6.1 Theoretical Modeling and Simulation	112
6.2 Analysis of MMFBGs Optical Characteristics	114
6.2.1 On the Refractive Index Change	115
6.2.2 On the Grating Period	119
6.2.3 On the Length of the Grating	121
6.2.4 On the Mode Excitation Condition	123
Single-mode/Multimode Fiber Launch	
Equal Mode Population Distribution	
Gaussian Mode Population Distribution	
6.2.5 On the Optical Fiber Structure	130
Comparison between SMFBGs and MMFBGs	
Comparison between SI MMFBGs and GI MMFBGs	
6.3 Summary	137
CHAPTER SEVEN: CONCLUSIONS	140
7.1 Thesis Summary and Conclusions	140
7.2 Future Work and Suggestions	148
APPENDIX	
A. Bessel Functions and Modified Bessel Functions	154
B. Bracketing and Bisection	155
C. Normalized Cutoff Frequencies V_c for Various LP_{lm} Modes	156
REFERENCES	157
FINISHED PAPERS SUBMITTED FOR PUBLICATIONS	164

List of Figures

Fig. 1-1 Hypothetical optical network illustrating the use of FBG's to enhance functionality and performance.	4
Fig. 1-2 Optical-powered hydraulic valve system.	5
Fig. 2-1 A schematic representation of an intra-core Bragg grating, with the planes of the modulated index of refraction shown along with reflected and transmitted light beams.	11
Fig. 2-2 Schematic of apparatus for producing and measuring fiber filters.	13
Fig. 2-3 Ray-optic illustration of (a) core-mode Bragg reflection by a FBG and (b) cladding-mode coupling by a fiber transmission grating.	15
Fig. 2-4 A corrugated section of a waveguide (upper). The incident and reflected intensities inside the corrugated section (lower).	18
Fig. 2-5 Er-doped fiber laser pumped with a 650-nm wavelength laser.	23
Fig. 2-6 A variety of reflector configurations used to enhance amplifier performance.	23
Fig. 2-7 Fiber chromatic dispersion compensation using a linearly chirped FBG reflector.	24
Fig. 2-8 Composite passive optical network with an eight-channel FBG demultiplexer.	25
Fig. 2-9 Transmission spectrum of a fiber Grating with a titled fringe pattern.	26
Fig. 2-10 Polarization rocking filter schematic showing the operating principle.	26
Fig. 3-1 Geometry, refractive-index profile, and typical rays in: (a) a multimode step-index fiber, (b) a single-mode step-index fiber, and (c) a multimode graded-index fiber.	28
Fig. 3-2 Root finding of solving the eigenvalue equation (3.28) for $V = 6.58998$. There are 10 subfigure in two rows, five columns each column corresponds to one order.	34
Fig. 3-3 Radial distributions of the fundamental LP_{01} mode in the transverse plane (a) Semi-logarithm E field (b) The electrical field amplitude (c) The modal field intensity. The parameters have been selected as: $n_1 = 1.46$, $n_2 = 1.45854$, $a = 5\mu\text{m}$.	36

Fig. 3-4 Radial distributions of the LP ₀₁ and LP ₁₁ modes (a) Semi-logarithm E field (b) The electrical field amplitude (c) The modal field intensity. The parameters are: $n_1 = 1.46$, $n_2 = 1.45854$, $a = 12\mu\text{m}$.	36
Fig. 3-5 Radial distributions of some lower-order modes in a step index fiber (a) Semi-logarithm E field (b) The electrical field amplitude (c) The modal field intensity. The parameters are set to be: $n_1 = 1.46$, $n_2 = 1.4348$, $a = 5.04\mu\text{m}$.	36
Fig. 3-6 The propagation constants as a function of wavelength in few mode fiber.	37
Fig. 3-7 The propagation constants as a function of wavelength in multimode fiber.	37
Fig. 3-8 Normalized propagation constant b as function of normalized frequency V for the guided modes of the optical fiber.	39
Fig.3-9 Fractional power contained in the core as a function of the frequency parameter V .	42
Fig.3-10 Fractional power contained in the cladding as a function of the frequency parameter V .	42
Fig. 3-11 Power-law refractive index profile $n^2(r)$ for different values of p .	43
Fig. 3-12 Radial distributions of lower-order and higher-order modes in multimode fiber (a) Semi-logarithm E field (b) The electrical field amplitude (c) The modal field intensity.	48
Fig.3-13 The propagation constants as a function of wavelength in a multimode parabolic graded-index fiber.	48
Fig.3-14 An broadened window of the propagation constants dependence on wavelength in a multimode step-index fibers whose full screen image shown previously in Fig. 3-7.	49
Fig. 3-15 Comparison of the propagation constant β_ν between step-index fiber and graded-index fiber on the mode index $\nu = 1, 2, \dots, M$.	52
Fig. 4-1 Core refractive index distribution of fiber Bragg gratings.	57
Fig. 4-2 Coordinates system for fiber gratings.	57
Fig. 4-3 Shooting method for two-point boundary value problem.	76
Fig. 4-4 Block diagram of the numerical algorithm for theoretical simulations.	79

Fig. 4-5 Solutions to four modes FBG CMEs: Reflection and Transmission spectra.	80
Fig. 4-6 Spectral response of the Bragg grating: (a)-(d) for decomposition analysis full spectra in Fig 4-5, respectively.	82
Fig. 4-7 Solutions to fifty-seven modes FBG CMEs: Reflection and Transmission Spectra.	83
Fig.4-8 Comparison of a typical reflection spectrum of a single mode fiber Bragg grating (SMFBG) (a) numerical spectrum, and (b) analytical spectrum.	85
Fig.4-9 Comparison of a typical reflection spectrum of a two-mode FBG: (a) numerical simulation of the FBG, and (b) analytical solution of the FBG.	85
Fig. 4-10 The numerically calculated reflection response of the four-mode MMFBG with weak cross coupling.	86
Fig. 4-11 Analytical solution of the four-mode MMFBG with only self coupling MMFBG.	86
Fig. 4-12 A quality factor Q diagram illustrating the coupling physical insight for a four-mode FBG. (a)-(e) are the Q factor analysis corresponding to the five major reflection peaks, respectively.	88
Fig. 5-1 Experimental setup of the reflectivity measure in MMF Bragg gratings	92
Fig.5-2 Intensity distribution of electrical fields in GI-MMF structure.	94
Fig.5-3 The dependence of b on V in graded-index multimode fiber.	94
Fig.5-4 The propagation constants as a function of wavelength in GI-MMF.	94
Fig. 5-5 An example for MMFBG without mode scrambler (a) illustration of mode excitation extraction (b) distribution of mode excitation condition.	95
Fig. 5-6 An example for MMFBG with mode scrambler (a) illustration of mode excitation extraction (b) distribution of mode excitation condition.	95
Fig. 5-7 Comparison of experimentally measured and theoretically calculated MMFBG reflection spectra with maximum reflectivity of (a) $R = 91\%$ and (b) $R = 99.39\%$. The dashed lines show the measured response, and the solid lines show the calculated results, with a 0.01nm resolution.	98
Fig. 5-8 Topographic maps that illustrate (a) coupling coefficient deployment, and (b) phase-matching condition, or Bragg reflection condition.	101

Fig. 5-9 Comparison of experimentally measured and theoretically calculated MMFBG reflection spectra with excitation conditions of (a) SMF-MMF launching without scrambler and (b) SMF-MMF launching with mode scrambler. The dashed lines show the measured response, and the solid lines show the calculated results, with a 0.01nm resolution. 103

Fig. 5-10 Experimentally measured MMFBG reflectivity spectra for mode scrambling excitation with (a) absent, (b) slight, (c) medium, and (d) strong modulation, respectively. 105

Fig. 5-11 Corresponding calculated reflectivity spectra of Fig. 5-10 (d) assuming a 0.01nm wavelength-resolution simulating. Here, we neglect subpeaks effect with the same explanation as Fig. 5-7 (b). 106

Fig. 6-1 Transmission and reflection response from uniform MMF Bragg grating for different index of refraction change (a) $\Delta n = 5 \times 10^{-5}$, (b) $\Delta n = 2 \times 10^{-4}$, and (c) $\Delta n = 1 \times 10^{-3}$, which, for convenience, are referred to in the text as weak, medium, and strong, respectively. 116

Fig.6-2 Corresponding Q factor diagrams of the strong uniform grating appearing in Fig.6-1(c). 118

Fig. 6-3 Spectral profile from varying period MMF Bragg gratings for the following period values of (a) $\Lambda = 0.535\mu\text{m}$, and (b) $\Lambda = 0.531\mu\text{m}$ over the 10mm length of the gratings. 120

Fig. 6-4 Reflected and transmitted spectra from uniform MMF Bragg grating 1mm in length for comparison with the spectral response of 10mm grating length in Fig. 6-3 (b). 122

Fig. 6-5 Calculated grating reflectivity spectra in graded-index MMF under three different excitation conditions. Plots are modes for fairly strong grating of (a) single-mode/multimode fibre launch, (b) equal mode population distribution, and (c) equal MPD excitation for a weak Bragg grating, (d) Gaussian mode population excitation. The accompanying sidelobe structure may be viewed as a “Fabry-Perot” effect. 124

Fig. 6-6 Effective medium picture for a (non)uniform grating. 126

Fig. 6-7 Plots of five types of Gaussian excitation profiles showing the intensity of gaussian distribution evolves from lower order to higher order, with mode changing occurrence. 128

Fig. 6-8 Comparison of transmission and reflection spectra of a Bragg grating in step-index MMF for different Gaussian mode excitation. Here, (a)-(e) spectral response correspond to five type Gaussian profiles appearing in Fig. 6-7 (a)-(e). 129

Fig. 6-9 The single mode fiber Bragg grating spectra with (a) equal MPD excitation, and (b) Gaussian profile excitation, indicating the resemblance of the spectral shape under different excitation conditions. 131

Fig. 6-10 The multimode fiber Bragg grating spectra with (a) equal MPD excitation, and (b) Gaussian profile excitation, indicating the transformation of the spectral shape under different excitation conditions. 132

Fig. 6-11 Reflection spectra under single- mode/multimode fiber launch from (a) parabolic-index profile MMFBG, and (b) step-index profile MMFBG. 134

Fig. 6-12 Response in decibels from (a) the same MMFBG as Fig. 6-12 (a), and (b) the same MMFBG as Fig. 6-12 (b). 134

Fig. 6-13 Corresponding excitation characteristics of GI uniform MMFBGs appearing in Figs. 6-11 (a) and 6-12 (a), in which (a) is radial distributions of the electric field amplitude of the core modes in GI MMFBGs, and (b) is the associated mode power distributions as a function of the mode number in GI MMFBGs. 136

Fig. 6-14 Corresponding excitation characteristics of SI uniform MMFBGs appearing in Figs. 6-11 (b) and 6-12 (b), in which (a) is radial distributions of the electric field amplitude of the core modes in SI MMFBGs, and (b) is the associated mode power distributions as a function of the mode number in SI MMFBGs. 136

List of Tables

Table 2-1 Types and characteristics of several fiber gratings	16
Table 2-2 Telecommunication Applications	22
Table 2-3 Other Applications	22
Table 3-1 Variations of b , U , and W for the fundamental mode of the step index fiber	38
Table 3-2 Normalized Cutoff Frequencies V_c for Various LP_{lm} Modes (Appendix C)	156
Table 3-3 Propagation constant values corresponding to Fig. 3-14	50
Table 4-1 Excitation conditions for separate mode analysis	81
Table 6-1 Physical characteristics of varying gratings used in the numerical simulations	113
Table 6-2 Physical configurations of varying excitation conditions used in the numerical simulations	113
Table 6-3 Physical properties of varying fibers used in the numerical simulations	113

CHAPTER ONE: INTRODUCTION

1.1 General Description

The spectacular growth of the internet, the new forms of digital data transportation services, and the worldwide deregulations in the telecommunications industry during the late 90's have caused an explosive growth in optical fiber communication systems. Fiber-optic communication networks operate at rates with necessary bandwidths unachievable by electronic signal generation. Traditionally, fiber-optics has been developed for the long-haul of wide area network (WAN), but now local area network (LAN) and metro area network (MAN) systems are beginning to employ fiber-optic gear [1]. Today, the term "fiber-optics" is synonymous with "telecommunications".

Optical networks enable high-capacity interconnections between producers and consumers of information located at most places on the earth. Demand for increased band-width resulting from new services and users has stimulated innovations in the lightwave industry, including the intriguing prospect of directly connecting all network users via gigabit-per-second optical links. Allocating communication channels to partitions in the optical frequency spectrum has established wavelength division multiplexed (WDM) transmission as a conventional method of increasing capacity and enables optical methods of implementing network functions. Commercial point-to-point WDM lightwave systems operating in the 1550-nm wavelength region may have 8, 16, or more channels, each carrying 2.5 to 10 Gb/s traffic with proposals of finer granularity, e.g., 64 channels at 622 Mb/s appearing. Furthermore the traditional point-to-point link will be supplanted with networks that include optical add/drop or cross-connect capability. In local access, information delivery to the subscriber residence is now predominately through copper wire or wireless connections; direct links with optical fibers in passive optical networks (PON's) is emerging as a competing technology [2].

Accompanying this evolution of the optical network infrastructure, with special emphasis on WDM transmission, there is a growing demand for new in-line fiber-optic components with various functionalities such as modulation, splitting, fitting, etc. Normally these functions are performed by taking the light out of the fiber, processing it using bulk optical components, and then coupling the light back into the fiber [3]. This would involve interruption of the light beam as it propagates in the fiber and thus would lead to high optical insertion loss, problems of stability of the components, and larger size, possibly resulting in more cost. These problems can be overcome by using in-line fiber-optic components in which the processing is performed without taking the light out of the fiber and which are completely compatible with the transmission medium – namely, the optical fiber.

Over the past three decades, the advancements in optical fibers has undoubtedly improved and reshaped fiber-optic technology. Despite the improvements in optical fiber manufacturing and advancements in the field in general, basic optical components such as mirrors, wavelength, and particle reflectors have been a challenge to integrate with fiber-optics. Recently, however, this has changed with the ability to alter the core index of refraction in a single-mode optical fiber by optical absorption of UV light. This photosensitivity of optical fibers allows the fabrication of phase structures in their cores. These phase structure, or phase gratings are obtained by permanently changing the index of refraction in a periodic pattern along the core of a fiber. A periodic modulation of the index of refraction in the fiber core acts like a selective mirror for the wavelength that satisfies the Bragg condition, in other words, it forms a fiber Bragg grating. The grating period and length, together with the strength of the modulation of the refractive index, determine the level of reflectivity and the width of the range of wavelengths to which this reflection applies [4].

In recent years, fiber Bragg gratings have emerged as important components in a variety of lightwave applications. The use of optical fiber Bragg gratings in commercial products has grown exponentially since their market introduction in 1995. In the area of optical communications, fiber gratings will affect almost every aspect

of optical communication from optical transmitter, optical amplification, and dispersion compensation to optical receiver. Fiber grating technology has played an important role in the design of fiber lasers and semiconductor lasers by enabling the fabrication of highly spectrum-selective feedback elements directly in the fiber core which leads to single longitudinal mode output with line width 100kHz. Fiber gratings can also be used in EDFAs. They can help achieve gain flattening through the whole bandwidth of EDFAs, effectively suppressing the ASE noise, improving the efficiency of pumps, and achieving ideal low-noise amplification. In addition, fiber gratings can be used to create WDM demultiplexers and add/drop multiplexers. Furthermore, the good linear characteristics between Bragg wavelength, temperature and stress give fiber gratings a good opportunity to be used as sensors. Fiber grating sensors today are buried in bridges and tunnels to monitor their structural integrity making sure those bridges and tunnels work normally [5].

An enthusiastic scenario based on these applications is depicted in Fig. 1-1 where FBG's are liberally applied to enhance the lightwave network all the way from the central office to the subscriber's premise [2]. Despite competitive technologies, many grating applications have matured, and others are nearing commercialization. As lightwave systems evolve to optical networks and fiber moves towards the home, the number of uses for FBGs will increase. Telecom industry experts predict that FBGs will be a \$1.3-billion market within three years.

Fiber Bragg gratings have, indeed, started a new era in the field of fiber-optic based devices, and are recognized as one of the most significant enabling technologies for fiber-optic communications. Within a few years from their initial development, fiber Bragg gratings moved from laboratory interest to the brink of implementation in optical communication and sensor systems. In a few years, it may be as difficult to think of fiber-optic systems without fiber Bragg gratings as it is to think of bulk optics without the familiar laboratory mirror [4].

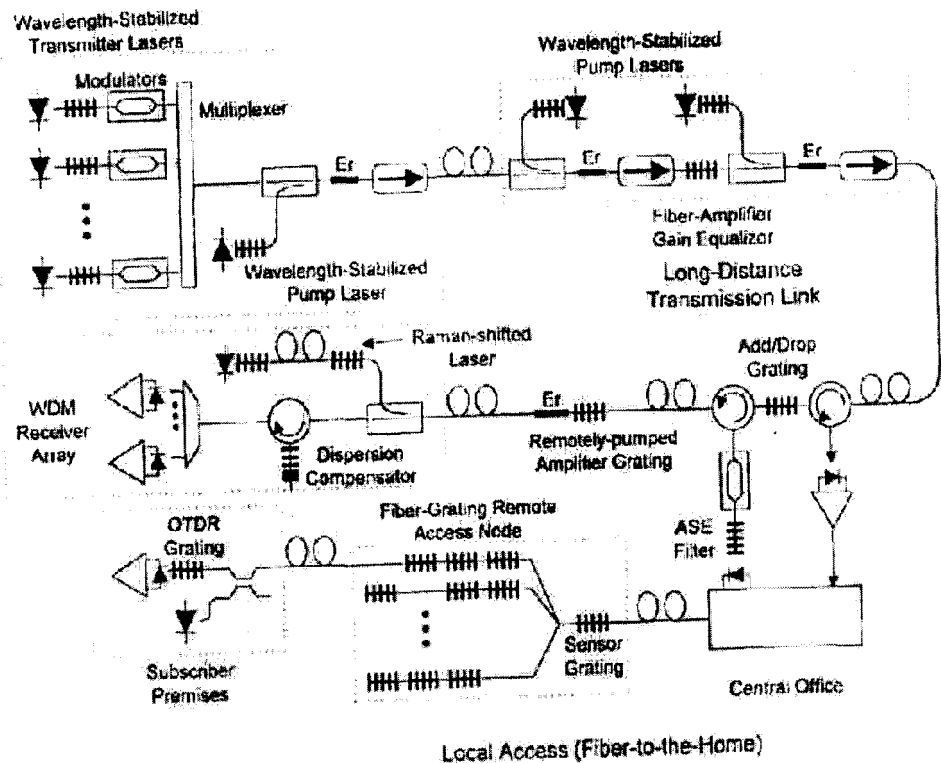


Fig. 1-1 Hypothetical optical network illustrating the use of FBG's to enhance functionality and performance (C. R. Giles, 1997).

1.2 Thesis Motivation and Objectives

Because of its many present and future applications in diverse modern opto-electronics, optical fiber sensor and optical fiber communication systems, the fiber Bragg grating (FBG) has received intense research attention in recent years. Since the first demonstration by *Meltz et al.* [6], FBG's have been formed only in single-mode optical fibers. During the past decade, single-mode fiber Bragg grating (SMFBG) structures have been studied extensively and the spectral characteristics have been well determined [4]. SMFBGs have also been used in numerous applications ranging from wavelength-selective filtering in

wavelength-division-multiple-access (WDMA) systems to temperature and strain sensing [7]. However, single-mode fiber (SMF) has a small core diameter and therefore is not easy to couple with optical devices except other SMF's or laser diodes. This limited SMFBGs is used in some important applications. On the other hand, multimode fiber (MMF) has a merit of easy coupling with other inexpensive light sources such as light-emitting diodes (LED's). In particular, graded-index MMF has relatively low dispersion and is therefore suitable for optical communications. If Bragg gratings in MMF's are possible and they have useful characteristics, they would easily contribute to new optical communication and optoelectronics applications [8].

For example, during the past decade single-mode optical fiber Bragg grating (SM-FBGs) have been popularly used for strain and temperature sensing in many applications such as structural monitoring, in hazardous environments. Recent research has been reported on a differential-pressure (DP) flow sensor using SM-FBGs for hydraulic valve monitoring applications [9]. However, using SM-FBGs in the application of an optically-powered hydraulic valve monitoring system is inappropriate [10]. This is because the system must utilize only one optical fiber for both optical power transmission and for sensing, as shown in Fig.1-2. Therefore, a multimode optical fiber Bragg Grating (MM-FBGs) is more suitable due to the large core diameter [11].

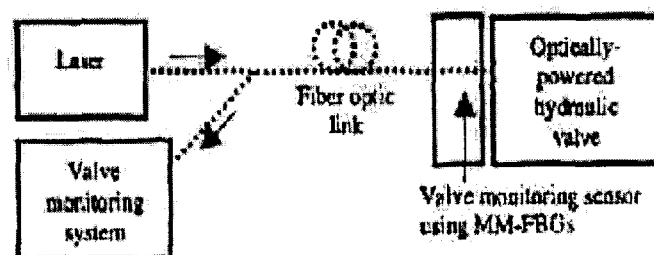


Fig. 1-2 Optical-powered hydraulic valve system (J. Lim and Q. P. Yang, *et al.*, 2001)

Early use of MMFBGs was reported by *Wanser et al* [12]. Micro-bending was used to disturb the population in an optical fiber via mode coupling before passing the light to the MMFBG, they presented all-mode, wave optics calculations of the reflectivity of independent mode MMFBG. A similar approach using the bending effect on a transmission spectrum of an MMFBG for displacement sensing was introduced by *Mizunami et al* [13], who experimentally investigated the spectral properties of MMFBGs. A grating was fabricated in graded-index MMF and in DSF. The number of reflection wavelengths of a Bragg grating at around $1.55\mu\text{m}$ is 19 for highly multimode excitation and 3-4 for lower order mode excitation. A Bragg grating at $0.8\mu\text{m}$ in DSF had three Bragg wavelengths. While he did not measure the reflection response, *Mizunami* did measure the temperature and polarization dependence. *Okude et al.* [14] fabricated a Bragg grating in a short piece of MMF with a core diameter of $17.5\mu\text{m}$ and spliced both ends with SMF's. In this case, only one reflection wavelength was obtained without excess losses due to coupling to cladding modes. Fortunately, *Vasa et al.* [15] demonstrated that FBGs can be used to tune a $\text{Cr}^{3+}:\text{LiSrAlF}_6$ laser. The promise of applying the high coupling efficiency of MMFs to solid-state lasers is very attractive. A novel multimode fiber structure with modal propagation characteristics specifically tailored to facilitate the creation of narrow-band MMFBGs has been proposed by *T. Szkopek et al* [7]. The possibility of a narrow-band fiber Bragg grating in MMF would enable the use of WDM in LANs and the field of *in vivo* Raman spectroscopy.

In the above studies, however, detailed characteristics or analysis of a Bragg grating in MMF, in particular, a thorough and systematic theoretical study on MMFBG has not been undertaken and reported.

Motivated by the lack of such a study, the main theme underlying the work of this thesis is to theoretically and experimentally investigate Bragg gratings in optical fibers in multimode propagation. Specifically, we aim to establish and develop a reasonable theoretical model and a sound numerical treatment for MMFBGs; provide

a valuable tool for the optimized design of fiber grating devices and the physical explanations for the experimentally observed phenomena.

1.3 Organization Outline

Two main studies were conducted as parts of this thesis work. The first study that is included is the development and implementation of a dynamic MMFBG numerical simulator. In this study fiber optical mode solver was constructed based on multimode structure modeling, fiber optical grating solver basically built on FBG model was also established, and these two solver were integrated together as a whole. The second study is the study of the applications of our powerful integrated MMFBG solver. In this case the MMFBG simulator is the applied for both experimental analysis and theoretical investigation.

The contents of this thesis are organized as follows.

Chapter 2 introduces the basic concepts and history of fiber Bragg gratings along with a concise explanation of different types of grating structures, including tapered gratings, chirped gratings, and tilted Bragg gratings. The basic theory to model the FBGs: the coupled mode theory (CMT) is briefly outlined, with focus given to the connection between the mathematical model and the relevant physical quantities. The chapter concludes with a brief application-oriented description of the various devices using Bragg gratings in the fields of the telecommunications and fiber sensors.

Chapter 3 begins with Maxwell's equations, which give the relation between electric and magnetic fields, and show that the transverse electric field of a mode in a weakly guiding waveguide satisfies the scalar wave equation, and thus we can derive the modal properties of light by studying properties of the solutions to this scalar wave equation. On the basis of weakly guiding approximation, a simplified eigenvalue equation for calculating the propagation constants in step-index fiber is formulated. We then solve the eigenvalue equation by numerical techniques because of its transcendental nature. Next discussed is how the simulation results provide all

the characteristics of the mode. Closing the chapter is a discussion of graded-index fibers, which focus on the propagation characteristics of an infinitely extended parabolic index fiber.

In Chapter 4 we describe in detail the derivation of the coupled mode theory formulations for Bragg gratings in MMF, including two categories of multimode fiber Bragg gratings (MMFBGs): independent mode and mode coupling. Analytical expressions for the transmission and reflection coefficients of a Bragg grating under specific conditions are derived as well and evidence for the validity of the MMFBGs modeling is presented. In addition to a derivation of the theoretical formalism, a detailed description of the numerical treatment used to achieve the solution to the coupled mode equations for MMFBGs is given. We then present the results of our simulations for multimode fiber Bragg gratings with various parameters and give further discussion on it in terms of the important resonance Q picture that is a quality factor of gratings proportional to the strength of the grating and simultaneously determined by phase matching condition.

Chapter 5 presents the experiments measuring Bragg gratings in standard graded-index MMF. In these experiments, the reflection characteristics of MMFBGs were studied as the refractive index of sections of the gratings were shifted and different conditions of excitation of modes were performed. Numerical predictions of the effects of refractive index change and mode excitation condition on the spectral characteristics of utilized gratings are then calculated. All the while, these numerical calculations are closely compared with experimental measurements. The agreement between theory and experiment has been not only qualitatively good but in many cases quantitatively good as well. Following this, the main sources of discrepancy in this work are analyzed. Since partial source of disagreement between theory and experiment appears to be experimental difficulties, a brief discussion on the present experiment limitations and future experiment improvements can be found at the end of this chapter.

Chapter 6 is devoted to a relatively thorough and detailed theoretical investigation of grating characteristics in multimode fiber. We examine the relation between the

optical properties of fiber Bragg gratings and their physical structure parameters of fiber and gratings. We then cover issues such as grating length dependence, index of refraction dependence, grating period dependence, excitation condition of modes dependence and fiber-optic structure dependence. Specific attention is paid to the effect of mode excitation condition and optical fiber structure on grating characteristics. Single-mode/multimode fiber launch, equal mode population distribution and Gaussian mode population distribution are studied respectively. The spectral characteristics of single mode fiber Bragg grating (SMFBGs), step index multimode fiber Bragg gratings, and graded index multimode fiber Bragg gratings (MMFBGs) are compared and discussed. The coupling coefficients and phase matching maps have been plotted in which the physical significance between the various conditions is exposed. These theoretical predications are of highly importance in MMFBG design, and of great potential in novel applications.

In chapter 7 we summarize the results of these work and discuss some future work that can be done to complement the studies presented here.

CHAPTER TWO: INTRODUCTION TO FIBER BRAGG GRATINGS

The discovery of photosensitivity in optical fibers led to a new class of in-fiber components: *Fiber Bragg Gratings*. The ability to inscribe intracore Bragg gratings in these photosensitive fibers has revolutionized the field of telecommunications and optical fiber based sensor technology. This chapter will briefly review the general background of fiber Bragg gratings, and is designed to be an overview of common grating types, responses and applications.

2.1 Basic Concepts

A fiber Bragg grating (FBG) is a periodic perturbation of the refractive index along the length of a fiber. Functionally, a Bragg grating can reflect a predetermined narrow or broad wavelength range of light incident on the grating, and allow all other wavelengths of the light to pass.

Photo-imprinting gratings in optical fibers requires the glass to be photosensitive, an effect discovered in 1978 by CRC's Dr. Kenneth Hill [16]. This phenomenon, termed *photosensitivity*, involves irradiating an optical waveguide with an ultraviolet laser beam to change the refractive index of the waveguides core. By irradiating the fiber with an intensive pattern that has a periodic distribution, a corresponding index grating is permanently photo-imprinted in the core of the fiber.

Photo-imprinting results makes a Bragg Grating a very selective spatial reflector in the core of the fiber. At each periodic refraction change a small amount of light is reflected. All the reflected light signals combine coherently to form one large reflection at a particular wavelength when the grating period is approximately half the input light's wavelength. This is referred to as the *Bragg condition*, and the

wavelength at which this reflection occurs is called the *Bragg wavelength*:

$$\Lambda = \frac{\lambda_B}{2n_{eff}}$$

where Λ is the modulation period of refractive index in core. λ_B is resonant wavelength, i.e. Bragg wavelength. n_{eff} is the effective index of the core.

Light signals at wavelengths other than the Bragg wavelength, which are not phase matched, are essentially transparent (see Fig. 2-1) [17]. Therefore, light propagates through the grating with negligible attenuation or signal variation. Only those wavelengths that satisfy the Bragg condition are affected and strongly back-reflected.

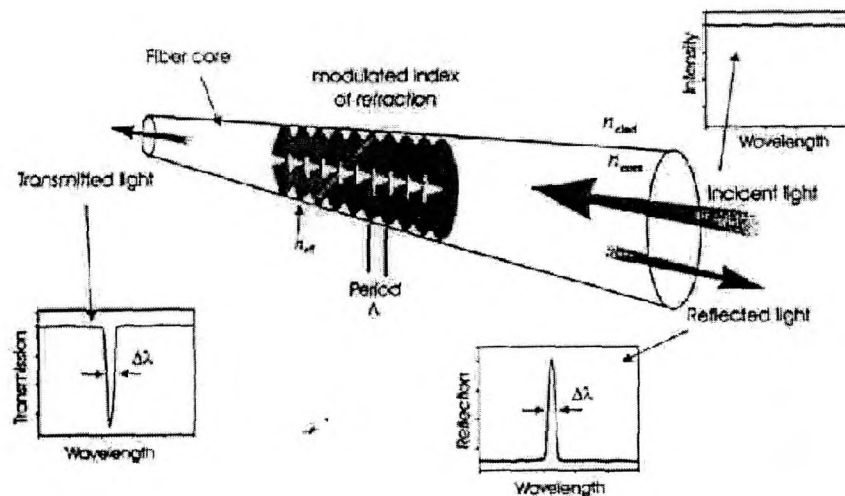


Fig. 2-1 A schematic representation of an intra-core Bragg grating, with the planes of the modulated index of refraction shown along with reflected and transmitted light beams (Andreas Othonos and Kyriacos Kalli, 1999).

The ability to accurately preset and maintain the grating wavelength is a fundamental feature and advantage of fiber Bragg gratings. Other features include:

- Low insertion losses and compatibility with existing optical fibers used in telecommunication networks.
- Low-cost manufacturing of very high quality wavelength-selective devices.

- Phase masks used to photo-imprint the Gratings allow manufacturing that is relatively simple, flexible, low-cost and large-volume.

Fiber gratings can be designed to operate over a wide range of wavelengths extending from the ultraviolet to the infrared region. The wavelength region near 1.5 μ m is of particular interest because of its relevance to fiber-optic communication system. Gratings can be designed to couple other phase-matched wavelengths out of the fiber core, into radiation and cladding modes for tailoring of the grating spectrum. But, these effects are not considered in this work.

2.2 Brief Historical Perspective

Fiber photosensitivity was first discovered by *Kenneth Hill et al.* in 1978 at the Canadian Communication Research Center, during a study of the nonlinear effects in a specially designed high silica optical fiber was in progress. The experimental arrangement used is shown in Figure 2-2 [18]. During an experiment, the attenuation of the fiber was observed to increase under prolonged exposure to core-launched visible light from an argon ion laser. An investigation into the origin of the apparent increase in attenuation determined that the intensity of the light backreflected from the fiber increased significantly as a function of time during the exposure. Subsequent experiments proved that this increase in reflectivity was the result of a permanent refractive index grating being photoinduced in the fiber. This new nonlinear effect in optical fibers was called *fiber photosensitivity*. Gratings of this type have since come to be known as "*Hill grating*" [19].

Within ten years of the discovery of Hill gratings (1978 to 1988), two significant results were produced. First, the experiments by *Lam & Garside* [20] showed that the magnitude of the photoinduced refractive index depends on the square of the writing intensity at argon-ion wavelengths (514.5 and 488nm), which suggests a two-photon process as the pathway of the index changes. Second, *Parent* [21] reported that the photoinduced index change is anisotropic.

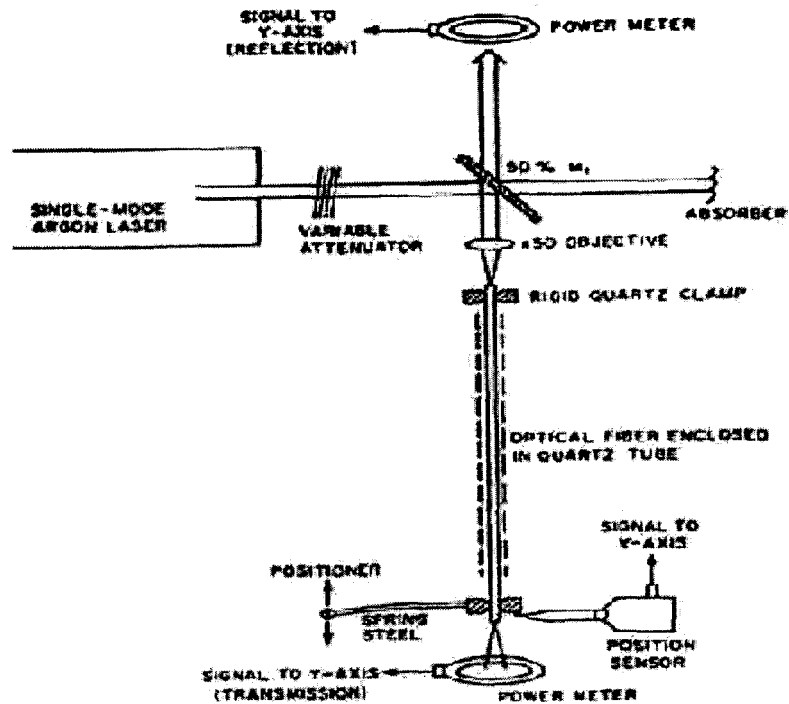


Fig. 2-2 Schematic of apparatus for producing and measuring fiber filters (K. O. Hill and B. Malo, *et al.*, 1993).

In 1989, an important advance in fiber photosensitivity research was reported by *Meltz et al.* [22, 6], who demonstrated the fabrication of Bragg gratings in the core of an optical fiber by exposing the fiber externally from the side to an interference pattern in the UV spectral region. This technique called the *transverse holographic technique* attracted a lot of concerns. This work overcame two disadvantages of the original Hill gratings: it dramatically improved the writing efficiency and it demonstrated the possibility of producing gratings with an arbitrarily selected Bragg wavelength simply by adjusting the angle between the exposing beams. Shortly thereafter, a demonstration of the first fiber Bragg grating that has a peak at the very important telecommunication wavelength of around 1530nm was made with an all-fiber erbium laser. Since then, interest and activity in the field has increased rapidly.

After the holographic method, the phase mask method was developed [23, 24].

Writing of a grating requires a high degree of spatial coherence. But many UV sources, including the fourth harmonic generated Nd:YAG and the excimer laser, have poor spatial coherence. Thus an extremely careful setup and vibration-free environment were necessary to write gratings holographically. The phase mask eliminates this problem. One can easily make a phase grating on a silica mask and send a UV beam through it. In doing so, one causes the interference between the two first order beams (or between the zeroth and one of the first order beams) from the grating is transferred to the fiber located directly behind the mask. This method lacks the flexibility of changing the peak wavelength once the phase mask is made, but makes mass production of identical FBGs possible through its simplicity of experimental handling.

In 1995, *Wong et al.* [25] demonstrated that poling a fiber while writing a grating with UV light resulted in an enhanced electro-optic coefficient. The strength of the UV-written grating could be subsequently modulated by applying an electric field. More recently, *Fujiwara et al.* [26] reported a similar photoassisted poling of bulk germanium-doped silica glass. The silica-germanium system will no doubt produce further surprises.

Nowadays, fiber Bragg gratings are seeing great progress. They represent a key element in the established and emerging fields of optical communications and optical fiber sensing.

2.3 Types of Fiber Gratings

Fiber gratings can be broadly classified into two major categories [27]: Bragg gratings (also called *reflection and short-period gratings*), in which coupling occurs between modes traveling in opposite directions; and transmission gratings (also called *long-period gratings*), in which the coupling is between modes traveling in the same direction. Fig. 2-3 illustrates the core-mode Bragg reflection by a fiber Bragg grating and cladding-mode coupling by a fiber transmission grating.

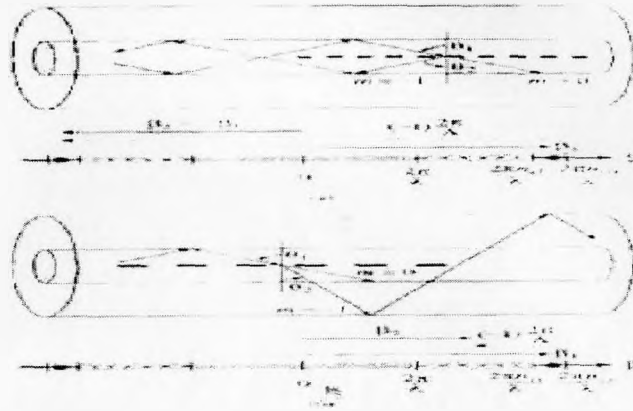





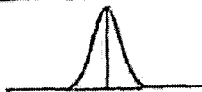

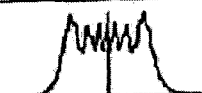




Fig. 2-3 Ray-optic illustration of (a) core-mode Bragg reflection by a FBG and (b) cladding-mode coupling by a fiber transmission grating (Turan Erdogan, 1997).

One can create various types of fiber gratings according to the grating structure in either the FBG or the LPG. Here, only FBGs are further discussed in this thesis. Table 2-1 [5] lists the main fiber Bragg grating types and basic spectrum. These Bragg gratings are distinguished either by their grating pitch (spacing between grating planes) or tilt (angle between grating planes and fiber axis). The distinct spectrum characteristics strongly depend on fiber grating structure types.

Uniform grating has strictly uniform periodic refractive index modulation, its reflection spectrum is composed of the resonant peak at the Bragg wavelength and some small side lobes. These side lobes come from Fabry-Perot effect caused by the mutation of refractive index at the end of the grating. Uniform grating can function as a narrow-band transmission or reflection filter or a broadband mirror, and as strain or temperature sensing devices capable of eliminating the problems of amplitude or intensity fluctuations that exist in many other types of fiber sensors [28-30].

Since in most cases side lobes are usually undesirable, people develop tapered gratings [5]. The refractive index of this kind of grating gradually decreases until it equals to the index of fiber core, this structure can eliminate the side lobes caused by mutation of index at the ends of the grating. Tapered fiber gratings can be realized

Table 2-1 Types and characteristics of several fiber gratings [5]

Fiber grating type	Refractive index modulation format	Reflective spectrum
Uniform fiber gratings		
Tapered fiber gratings		
Chirped fiber gratings		
Moiré fiber gratings		
Tilted fiber gratings		

using apodization, which is tapering the amplitude of the refractive index modulation along the length of the grating. If done smoothly, and on a scale much larger than the wavelength of the light, apodization eliminates out-of-band reflections from impedance mismatch at the ends of the grating.

A chirped Bragg grating is a grating that has a monotonically varying grating period [4, 5]. This can be realized by axially varying either the period of the grating or the index of refraction of the core or both. The reflection spectrum of chirped fiber grating has wide bandwidth and the chirp parameter determines the bandwidth of reflection spectrum and dispersion property. In a chirped grating, the resonant frequency is a linear function of the axial position along the grating so that different frequencies, which are present in the pulse, are reflected at different points and, thus, acquire different delay times. Therefore, chirped gratings, therefore, can be used as dispersion compensators to compress temporally broadened pulses.

A Moiré grating is a superposition of two or more Bragg gratings with slightly different periods which make an amplitude modulation in the index change [5]. Its

optical spectrum indicates that it can be used as a bandpass filter. Actually moiré grating is a tilted phase grating. Tilt in a grating is a shift of the grating plane from normal incidence to incidence with some angle. This angle is chosen so that the Bragg reflection is minimal, hence it can provide fixed power attenuation in some wavelength range. People usually use moiré gratings to realize gain flattening in EDFAs.

Tilting (or blazing) the Bragg grating planes at angles to the fiber axis results in light being coupled out of the fiber core into loosely bound guided cladding modes or into radiation modes outside the fiber. The tilt of the grating planes and strength of the index modulation determines the coupling efficiency and bandwidth of the light that is tapped out. For blazed gratings, not only do different wavelengths emerge at different angles, but also different modes of the same wavelength also emerge at slightly different angles due to their different propagation constants [4, 31].

2.4 Basic Theory of FBGs — Coupled Mode Theory

A lot of theory results about the optical properties of fiber gratings are based on coupled mode theory. Coupled mode theory is a good tool for obtaining quantitative information about the diffraction efficiency and spectral dependence of fiber gratings. People commonly use it not only because it can accurately model the optical property of fiber gratings, but also because it is straight forward and intuitive.

Coupled mode theory is described in a number of texts; the notation in the references might be quite different. In this section we will follow the notations used by Snyder and Love [32], Poladian [33] and Johannes [34]. Here, we assume that the fiber is lossless and single mode in the wavelength range of interest. In other words, we consider only one forward and one backward propagating mode. More general and complex situation will be treated later in Chapter 4. Moreover, we assume that the fiber is weakly guiding, i.e., the difference between the refractive indices in the core and the cladding is very small. Then the electric and magnetic fields are approximately transverse to the fiber axis, and we can ignore all polarization effects

due to the fiber structure and consider solely the scalar wave equation [32]. The fiber axis is oriented in the $+z$ direction and we assume that the electric field is x -polarized, The implicit time dependence is $\exp(-i\omega t)$; a forward propagating wave with propagation constant $\beta > 0$ and frequency $\omega > 0$ has thus the form $\exp[i(\beta z - \omega t)]$.

The grating is treated as a perturbation on the fiber. The unperturbed fiber has refractive index profile $\bar{n}(x, y)$ and the perturbed fiber has the z -dependent index $n(x, y, z)$.

Both fibers are weakly guiding so we assume $\bar{n} \cong n \cong n_{eff} \cong n_{cl}$, where n_{cl} is the index in the cladding and n_{eff} is the effective index of the supported mode in the absence of the grating. We write the total electric field as a superposition of the forward and backward propagating modes,

$$E_x(x, y, z) = b_1(z)\psi(x, y) + b_{-1}(z)\psi(x, y) \quad (2.1)$$

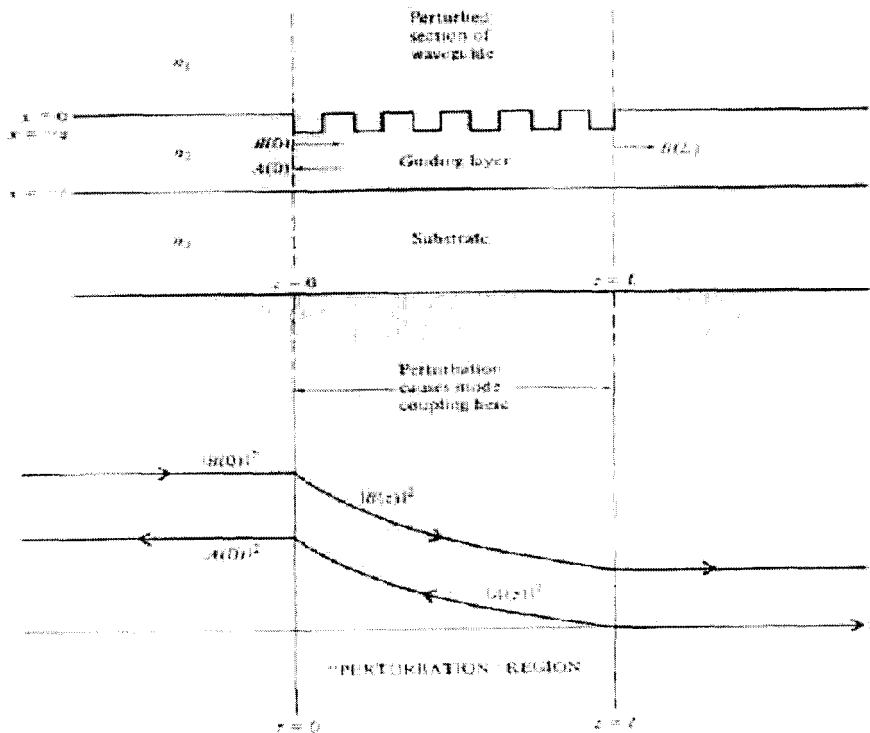


Fig. 2-4 A corrugated section of a waveguide (upper). The incident and reflected intensities inside the corrugated section (lower) (Yariv A., 1991).

Where the coefficients $b_{\pm l}$ contain all the z -dependence of the modes. It is clear that $b_{\pm l}$ are dependent on frequency since they include the harmonic propagation factor $\exp(\pm i\beta z)$ with $\beta = \beta(\omega) = n_{\text{eff}} \omega / c = n_{\text{eff}} k$ as the scalar propagation constant. The transverse dependence is described by the function Ψ , which satisfies the scalar wave equation for the unperturbed fiber,

$$\{\nabla_t^2 + k^2 \bar{n}^2(x, y) - \beta^2\} \Psi = 0 \quad (2.2)$$

where $\nabla_t^2 = \partial^2 / \partial x^2 + \partial^2 / \partial y^2$ and $k = \omega / c$ is the vacuum wavenumber. The total electric field E_x must satisfy the scalar wave equation for the perturbed fiber, i. e.

$$\{\nabla_t^2 + k^2 n^2(x, y, z) + \partial^2 / \partial z^2\} E_x = 0 \quad (2.3)$$

By substituting (2.1) into (2.3), and using (2.2), we obtain

$$\frac{d^2}{dz^2} (b_1 + b_{-1}) \Psi + [\beta^2 + k^2 (n^2 - \bar{n}^2)] (b_1 + b_{-1}) \Psi = 0 \quad (2.4)$$

Multiplication by Ψ and integration over the xy -plane leads to

$$\frac{d^2 b_1}{dz^2} + \frac{d^2 b_{-1}}{dz^2} + (\beta^2 + 2kn_{co} D_{11}(z)) (b_1 + b_{-1}) = 0 \quad (2.5)$$

where we have defined the coefficient D_{11} as

$$D_{11}(z) = \frac{\frac{k}{2n_{co}} \int (n^2 - \bar{n}^2) \Psi^2 dA}{\int \Psi^2 dA} \quad (2.6)$$

The refractive index $n_{co} \approx n_{\text{eff}}$ is an approximate value for the index in the fiber core, and the integrations extend over the entire xy -plane. Eq. (2.5) can be decomposed into the following set of first order differential equations [32]

$$\begin{aligned} \frac{db_1}{dz} - i(\beta + D_{11}) b_1 &= iD_{11} b_{-1} \\ \frac{db_{-1}}{dz} + i(\beta + D_{11}) b_{-1} &= -iD_{11} b_1 \end{aligned} \quad (2.7)$$

as is readily realized by differentiation and summation of the two equations in (2.7). This decomposition corresponds to separating the total field in (2.1) into its forward and backward propagating components. Indeed, when $n = \bar{n}$, we observe that the

solution of (2.7) reduces to $b_{\pm 1}(z) = B_{\pm 1} \exp(\pm i\beta z)$ with constant $B_{\pm 1}$, i.e. $b_{\pm 1}$ correspond to the forward and backward propagating modes. In the absence of the grating, $n = \bar{n}$, the modes propagate without affecting each other; otherwise the modes will couple to each other through the quantity $D_{11}(z)$.

For a fiber grating, the z -dependence of the index perturbation is approximately quasi-sinusoidal in the sense that it can be written

$$n^2 - \bar{n}^2 = \Delta\epsilon_{r,ac} \cos\left(\frac{2\pi}{\Lambda} z + \theta(z)\right) + \Delta\epsilon_{r,dc}(z) \quad (2.8)$$

where Λ is a chosen design period so that $\theta(z)$ becomes a slowly varying function of z compared to a period Λ . The functions $\Delta\epsilon_{r,ac}(z)$ and $\Delta\epsilon_{r,dc}(z)$ are real and slowly varying, and satisfy

$$[\Delta\epsilon_{r,ac}(z)] \ll n_{co}^2, [\Delta\epsilon_{r,dc}(z)] \ll n_{co}^2 \quad (2.9)$$

It is therefore convenient to express D_{11} as a quasi-sinusoidal function

$$D_{11}(z) = \kappa(z) \exp\left(i\frac{2\pi}{\Lambda} z\right) + \kappa^*(z) \exp\left(-i\frac{2\pi}{\Lambda} z\right) + \sigma(z) \quad (2.10)$$

where $\kappa(z)$ is a complex, slowly varying function of z and $\sigma(z)$ is a real, slowly varying function that accounts for the dc index variation from $\epsilon_{r,dc}(z)$. In order to simplify (2.7), we define new field amplitudes u and v by setting

$$\begin{aligned} b_1(z) &= u(z) \exp\left(+i\frac{\pi}{\Lambda} z\right) \exp\left(+i\int_0^z \sigma(z') dz'\right) \\ b_{-1}(z) &= v(z) \exp\left(-i\frac{\pi}{\Lambda} z\right) \exp\left(-i\int_0^z \sigma(z') dz'\right) \end{aligned} \quad (2.11)$$

By substituting (2.10) and (2.11) into the equations (2.7), ignoring the terms that are rapidly oscillating since they contribute little to the growth and decay of the amplitudes, we arrive at the coupled-mode equations

$$\begin{aligned} \frac{du}{dz} &= +i\delta u + q(z)v \\ \frac{dv}{dz} &= -i\delta v + q^*(z)u \end{aligned} \quad (2.12)$$

In (2.12) we have defined the wavenumber detuning $\delta = \beta - \pi/\Lambda$ and the coupling coefficient q of the grating

$$q(z) = i\kappa(z) \exp\left(-2i \int_0^z \sigma(z') dz'\right) \quad (2.13)$$

Note that all phase factors in (2.11) are independent of the propagation constant β and therefore the frequency. Hence, we can simply treat the new variables u and v as the fields themselves once the reference planes have been fixed, since they differ only from $b_{\pm 1}$ by constant phase factors. For example, the reflection coefficient $b_{-1}(z_0)/b_{+1}(z_0)$ can as well be computed by the expression $v(z_0)/u(z_0)$ once the position z_0 has been fixed because the two expressions only differ by a constant phase factor. Also note that all the functions u , v and q are slowly varying with z compared to the period Λ because $\beta \approx \pi/\Lambda$ when the wavelength is close to the Bragg wavelength $\lambda_B = 2n_{eff}\Lambda$.

We summarize the grating model as follows. The Bragg grating is characterized by the following quantities: The design Bragg wavelength λ_B , the effective refractive index n_{eff} , and the slowly varying complex coupling coefficient $q(z)$. The modulus of the coupling coefficient determines the grating strength or the index modulation amplitude and the phase corresponds to the grating phase envelope. The forward and backward propagating field envelopes are mutually coupled by the coupled mode equations

$$\begin{aligned} \frac{du(z; \delta)}{dz} &= +i\delta u + q(z)v \\ \frac{dv(z; \delta)}{dz} &= -i\delta v + q^*(z)u \end{aligned} \quad (2.14)$$

where δ is proportional to the frequency detuning with respect to the design Bragg frequency,

$$\delta = \beta - \pi/\Lambda = (\omega - \omega_B)n_{eff}/c, \quad \omega_B = 2\pi c/\lambda_B \quad (2.15)$$

This model forms the basic theory of FBG.

2.5 Applications of Fiber Bragg Gratings

Fiber gratings have very appealing applications to optic communications and fiber optic sensor system. In addition, there are potential applications in lidars, optical switching, optical signal processing, and optical storage. In the following, Table 2-2 and Table 2-3 [36] list the applications that have employed fiber Bragg gratings. Only a few of the applications are described in more detail.

Table 2-2 Telecommunication Applications [36]

Applications
Dispersion compensation
Wavelength selective devices
Band-rejection filters, long-period gratings
Fiber taps
Fiber erbium amplifiers
Network monitoring and optical fiber identification
Cascaded Raman amplification at 1.3 μ m
Fiber lasers
Semiconductor lasers with external Bragg grating reflector

Table 2-3 Other Applications [36]

Application
Optical fiber mode converters; spatial mode converters, polarization mode converters
Grating-based sensors
Optical signal processing; delay line for phased array antennas, fiber grating compressor
Nonlinear effects in fiber Bragg gratings; optical switch, electro-optic devices, wavelength conversion devices
Optical storage; holographic storage, direct writing

Fiber Lasers

All-fiber lasers can be constructed using FBG's as wavelength-selective resonator mirrors and erbium-doped fiber as the gain medium [2]. These fiber lasers are optically pumped directly. Narrow linewidth fiber lasers suitable as externally-modulated cw sources have been demonstrated in gigabit/s transmission experiments [37] and short distributed-feedback fiber lasers having Er-Yb-doped

gain sections have also exhibited robust single-frequency operation [38]. Low-cost configurations have been proposed using 650nm lasers to pump the Er-doped gain region as shown in Fig. 2-5 [39].

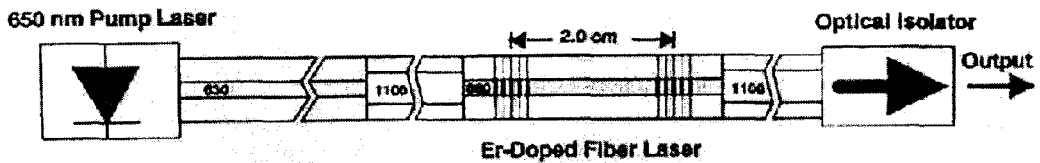


Fig. 2-5 Er-doped fiber laser pumped with a 650-nm wavelength laser (C.R. Giles and V. Mizrahi).

Reflectors in Fiber Amplifiers

Numerous fiber amplifier configurations have been proposed to utilize reflectors or filters to enhance performance [2]. For example, placing a single broadband reflector at the output of an erbium-doped fiber amplifier double-passes the input signal, increasing the small-signal gain and recycling remnant pump light. Reflecting only the pump light may increase the amplifier saturated output power in those cases of amplifiers having marginal pump power. Fig. 2-6 shows a variety of reflector

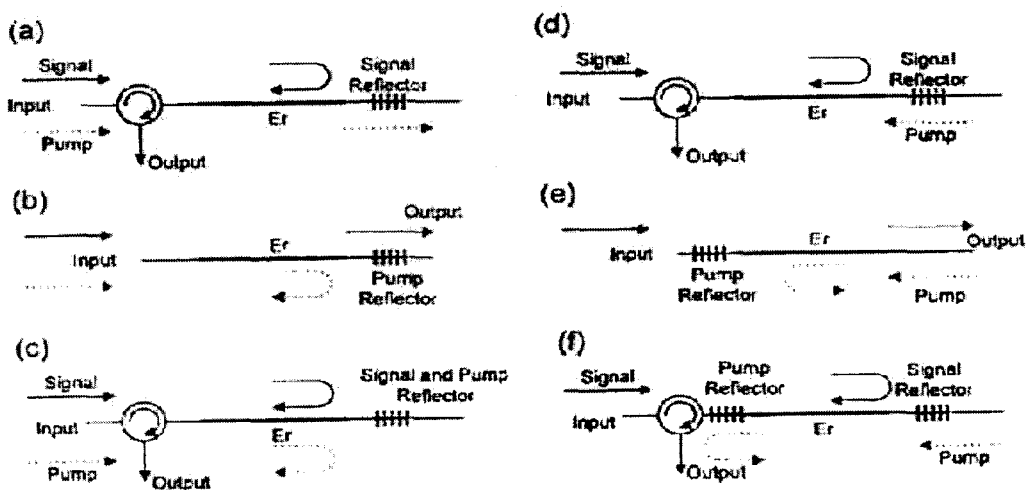


Fig. 2-6 A variety of reflector configurations used to enhance amplifier performance (C. R. Giles and J. Stone, *et al.*, 1991).

configurations used to enhance amplifier performance [40]. FBG's can be used as efficient wavelength-selective reflectors that discriminate between pump and signal light.

Dispersion Compensators

Table 2-2 lists a number potential applications for fiber Bragg gratings in fiber optic communications. Among them, a particularly exciting application is the Bragg grating dispersion compensator. Chromatic dispersion in transmission fiber chromatic dispersion can cause significant distortion of optical pulses, leading to system penalties. Upgrading existing lightwave systems to 10Gb/s channels usually requires dispersion compensators often using long lengths of dispersion-compensating fiber [41]. The chirped grating as shown in Fig. 2-7 can be designed so that all wavelengths in the light pulse exit the reflector at the same time and the dispersion in the optical pulse is equalized [2].

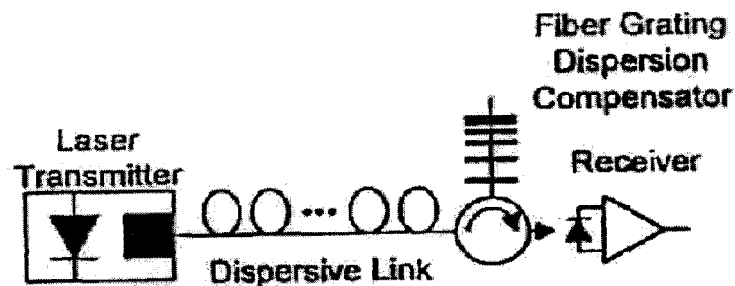


Fig. 2-7 Fiber chromatic dispersion compensation using a linearly chirped FBG reflector (C. R. Giles, 1997).

Filters and Demultiplexers

Another application that takes advantage of the wavelength accuracy of fiber Bragg gratings is their use as filters, especially in WDM systems [42].

The channels of a WDM network are combined in a multiplexer, traverse the fiber link and then are separated with a demultiplexer to direct each channel to its receiver [2]. The multiplexers may either be wavelength selective as in arrayed waveguide

grating multiplexers or bulk grating multiplexers, or wavelength independent as in optical couplers. In contrast, the demultiplexer must separate the channels with low crosstalk. Arrayed-waveguide grating, interference filter or bulk-grating demultiplexers may be used. Fig. 2-8 shows an experiment of a composite passive optical network [43]. In this demonstration, the WDM demultiplexer separating the downstream traffic was a 1x8 fused-fiber coupler having seven reflection gratings written on each output port to reject all except the customer's channel.

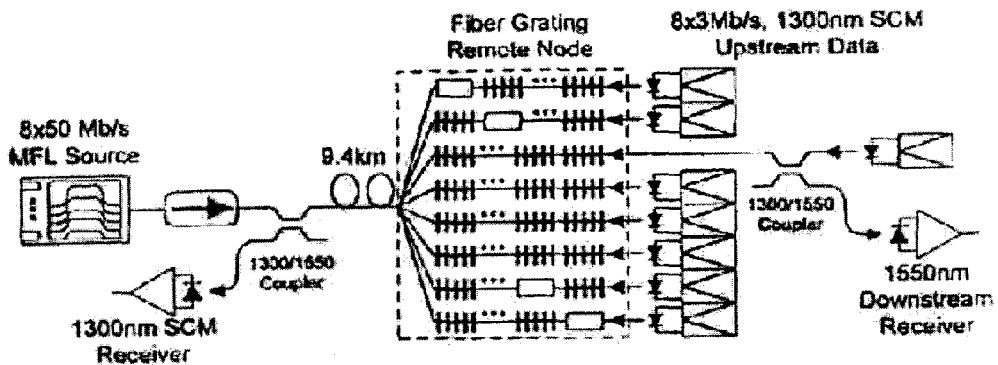


Fig. 2-8 Composite passive optical network with an eight-channel FBG demultiplexer (C. R. Giles and R. D. Feldman, *et al.*, 1996).

Mode and Polarization Converters

The most promising application FBG is in the field of optical fiber sensors. We also discuss mode converters because of their potential use in FBG sensors.

A resonant interaction that produces efficient bound-mode conversion within a fiber is enabled by a periodic index perturbation with a pitch that satisfies the Bragg condition for backward or forward synchronous interaction and the correct azimuthal variation to couple symmetric and asymmetric modes [36]. A simple example is the reflection of the LP_{11} mode by a grating which is slightly tilted (Fig. 2-9) [44, 45]. A fiber grating written with a UV beam that is polarized along a fiber diameter will be slightly birefringent. This effect can be used to form a polarization mode converter by arranging the UV-induced, periodic birefringence to form a resonant rocking filter as

shown in Fig. 2-10 [46, 47]. Orthogonal polarizations will be coupled in a narrow band that is controlled by the pitch and total length of the exposed segments.

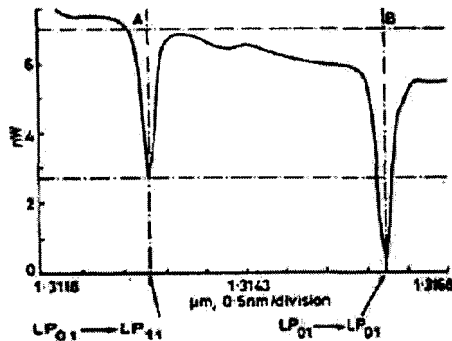


Fig. 2-9 Transmission spectrum of a fiber Grating with a tilted fringe pattern (Kenneth O. Hill and Gerald Meltz, 1997).

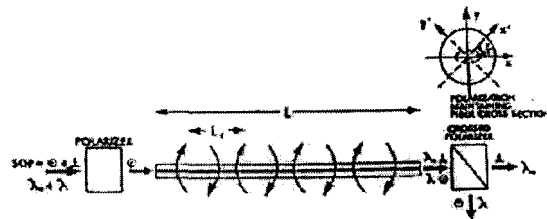


Fig. 2-10 Polarization rocking filter schematic showing the operating principle (Kenneth O. Hill and Gerald Meltz, 1997).

Optical Fiber Sensors

Optical fiber sensor technology based on intra-core Bragg gratings has uses in a number of important application areas ranging from structural monitoring to chemical sensing [48-50]. Practical and cost effective systems are not far in the future judging from recent advances in grating manufacture and sensor readout instrumentation.

Any change in fiber properties, such as strain, temperature, or polarization which varies the modal index or grating pitch, will change the Bragg wavelength. The grating is an intrinsic sensor which changes the spectrum of an incident signal by coupling energy to other fiber modes.

A very important advantage of an FBG sensor is that it is wavelength-encoded [36]. Shifts in the spectrum, seen as a narrowband reflection or dip in transmission, are independent of the optical intensity and uniquely associated with each grating, provided no overlap occurs in each sensor stop-band. With care in selection of the Bragg wavelengths, each tandem array of FBG sensors only registers a measured change along its length and not from adjacent or distant transducers. The sensitivity is governed by the fiber elastic, elasto-optic and thermo-optic properties and the nature of

the load or strain which is applied to the structure that the fiber is attached to or embedded within.

Applications to Planar Optical Waveguides

So far, this project has been restricted to discussing photosensitivity in optical fibers, but glass planar waveguides are also photosensitive. Consequently, there is an interest in applying photosensitivity technology to planar glass optical waveguides. For example, the photosensitivity of thin film germanosilicate layers can be used to obtain lateral confinement by forming a buried channel waveguide with a focused UV beam. The technology can also be used to modify the modal propagation constants to trim interferometric filters and couplers and to reduce bend losses [36].

2.6 Summary

This chapter is a brief introduction to the field of fiber gratings. The historical beginnings of photosensitivity and fiber Bragg grating (FBG) technology are recounted. The basic concepts, fundamental physical mechanism, prominent types and their characteristics of fiber gratings are described. The many applications of fiber grating technology are tabulated, and some key applications are briefly described. It is particularly noteworthy that no other device has had a significant impact on both sensing and optical communications applications and markets simultaneously.

Thus far, many facts prove that fiber gratings have broad application prospective and huge marketing potential. The moving of the fiber near to subscribers home, increases the needs and the diversity of applications of the gratings, opening new perspectives in this field. However, although the perspectives are still attractive, in the research area there is a long walk to be done before one starts to innovate in this area. From now on, the following chapters will be devoted to the main thesis work on MMFBGs which is an apparently novel and highly significant issue in FBG's research area.

CHAPTER THREE: MODELING AND SIMULATION OF GUIDED MODES IN OPTICAL FIBERS

Optical fibers are thin, long cylindrical structures which support light propagation through total internal reflection. An optical fiber is composed of an inner core and an outer cladding typically made of silica glass, although, materials like plastics are sometimes used. Single mode (SM) fiber is designed such that all the higher order waveguide modes are cut-off by a proper choice of the waveguide parameters. The multimode (MM) fiber is made of a core region whose diameter is a large multiple of the optical wavelength. The index profile of the core is either uniform (step-index) or graded (eg., parabolic). Optical fibers are therefore classified as step-index or graded-index, and multimode or single-mode as illustrated in Fig.3-1 [51].

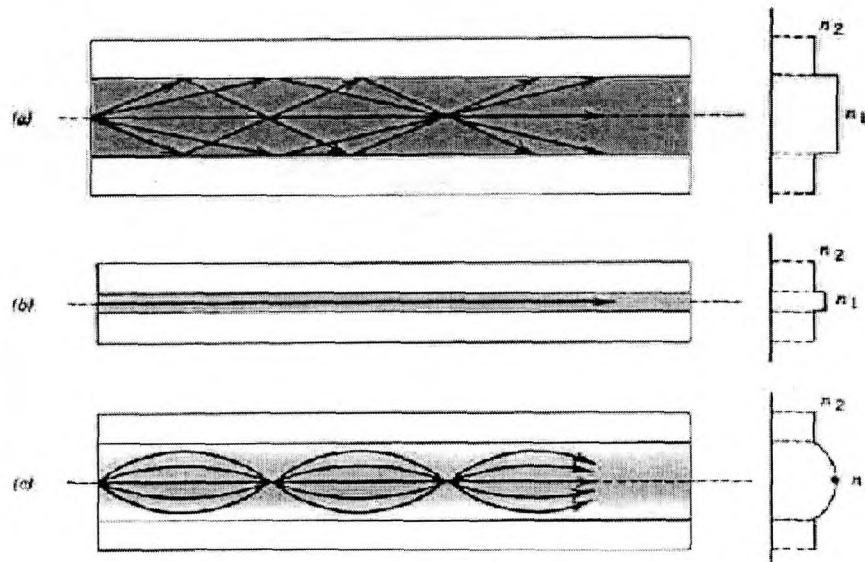


Fig. 3-1 Geometry, refractive-index profile, and typical rays in: (a) a multimode step-index fiber, (b) a single-mode step-index fiber, and (c) a multimode graded-index fiber (Bahaa E. A. Saleh and Malvin Carl Teich).

This chapter will study the subject of optical guided modes in fibers. It consists of two parts: modeling and simulation of step index fibers, and modeling and simulation of graded index fibers.

3.1 Mode Modeling and Simulation for Step Index Fibers

In this section we examine the propagation of guided waves in step-index fibers using electromagnetic theory. We aim to determine the electric and magnetic fields of guided waves that satisfy Maxwell's equations and the boundary conditions imposed by the cylindrical dielectric core and cladding. In succession, we use the numerical method to find the guided modes in a step-index fiber, each of which has a distinct propagation constant, a characteristic field distribution in the transverse plane, and two independent polarization states.

3.1.1 Maxwell's Equations

To analyze the optical waveguide we need to consider Maxwell's equations, which give the relationships between electric and magnetic field. Assuming a linear, isotropic dielectric material having no current and free charges, these equations take the form

$$\nabla \times \vec{E} = -\frac{\partial \vec{B}}{\partial t} \quad (3.1a)$$

$$\nabla \times \vec{H} = \frac{\partial \vec{D}}{\partial t} \quad (3.1b)$$

$$\nabla \cdot \vec{D} = 0 \quad (3.1c)$$

$$\nabla \cdot \vec{B} = 0 \quad (3.1d)$$

where $\vec{D} = \epsilon \vec{E}$, $\vec{B} = \mu \vec{H}$. The parameter ϵ is the permittivity (or dielectric constant) and μ is permeability of the medium.

A relationship defining the wave phenomena of the electromagnetic fields can be derived from Maxwell's equations. Taking the curl of Eq. (3-1a) and making use of

Eq. (3-1b) yields

$$\nabla \times (\nabla \times \vec{E}) = -\mu \frac{\partial}{\partial t} (\nabla \times \vec{H}) = -\epsilon\mu \frac{\partial^2 \vec{E}}{\partial t^2} \quad (3.2a)$$

Using the vector identity,

$$\nabla \times (\nabla \times \vec{E}) = \nabla(\nabla \cdot \vec{E}) - \nabla^2 \vec{E}$$

and using Eq. (3.1c) (i.e. $\nabla \cdot \vec{E} = 0$), Eq. (3.2a) becomes

$$\nabla^2 \vec{E} = \epsilon\mu \frac{\partial^2 \vec{E}}{\partial t^2} \quad (3.2b)$$

Similarly, by taking the curl of Eq.(3.1b), it can be shown that

$$\nabla^2 \vec{H} = \epsilon\mu \frac{\partial^2 \vec{H}}{\partial t^2} \quad (3.2c)$$

Equations (3.2b) and (3.2c) are the standard *wave equations* [52].

3.1.2 The Scalar Wave Equation for the Modal Fields

The step index fiber is characterized by the following refractive index distribution

$$\begin{aligned} n(r) &= n_1 & 0 < r < a & & \text{core} \\ &= n_2 & r > a & & \text{cladding} \end{aligned} \quad (3.3)$$

Most fibers are weakly guiding (i.e., $n_1 \approx n_2$ or $\Delta \ll 1$) so that the guided rays are paraxial (i.e. approximately parallel to the fiber axis). The longitudinal components of the electric and magnetic fields are then much weaker than the transverse components and the guided waves are approximately transverse electromagnetic (TEM). The linear polarization in the x and y directions then form orthogonal states of polarization. The linearly polarized (l, m) mode is usually denoted as the LP_{lm} mode. The two polarization of mode (l, m) travel with the same propagation constant and have the same spatial distribution.

In the weakly guiding approximation the transverse component of the electric field (E_x or E_y) satisfies the scalar wave equation [53]

$$\nabla^2 \Psi = \epsilon_0 \mu_0 n^2 \frac{\partial^2 \Psi}{\partial r^2} \quad (3.4)$$

For n^2 depending only on the transverse coordinates (r, ϕ) , we may write

$$\Psi(r, \phi, z, t) = \psi(r, \phi)e^{i(\omega t - \beta z)} \quad (3.5)$$

where ω is the angular frequency and β is known as the propagation constant. The above equation represents the modes of the system. Substituting in equation (3.4), we readily obtain

$$\left(\nabla^2 - \frac{\partial^2}{\partial z^2} \right) \psi + \left[\frac{\omega^2}{c^2} (n^2(r, \phi) - \beta^2) \right] \psi = 0 \quad (3.6)$$

In most practical fibers n^2 depends only on the cylindrical coordinate r and therefore it is convenient to use the cylindrical system of coordinates to obtain

$$\frac{\partial^2 \psi}{\partial r^2} + \frac{1}{r} \frac{\partial \psi}{\partial r} + \frac{1}{r^2} \frac{\partial^2 \psi}{\partial \phi^2} + [k_0^2 n^2(r) - \beta^2] \psi = 0 \quad (3.7)$$

where

$$k_0 = \omega / c = 2\pi / \lambda_0 \quad (3.8)$$

is the free space wave number. Because the medium has cylindrical symmetry, we can solve equation (3.7) by the method of separation of variables:

$$\psi(r, \phi) = R(r)\Phi(\phi) \quad (3.9)$$

On substituting and dividing by $\psi(r, \phi)/r^2$, we obtain

$$\frac{r^2}{R} \left(\frac{d^2 R}{dr^2} + \frac{dR}{r dr} \right) + r^2 [n^2(r)k_0^2 - \beta^2] = -\frac{1}{\Phi} \frac{d^2 \Phi}{d\phi^2} = +l^2 \quad (3.10)$$

where l is a constant. The ϕ dependence will be of the form $\cos l\phi$ or $\sin l\phi$ and for the function to be single valued (i.e., $\Phi(\phi+2\pi) = \Phi(\phi)$) we must have

$$l = 0, 1, 2, \dots \text{etc.} \quad (3.11)$$

(Negative values of l correspond to the same field distribution.) Since for each value of l there can be two independent states of polarization, modes with $l \geq 1$ are four-fold degenerate corresponding to two orthogonal polarization states and to the ϕ dependence being $\cos l\phi$ or $\sin l\phi$, modes with $l = 0$ are ϕ independent and have two-fold degeneracy. The radial part of the equation gives us

$$r^2 \frac{d^2 R}{dr^2} + r \frac{dR}{dr} + \left\{ [k_0^2 n^2(r) - \beta^2]^2 - l^2 \right\} R = 0 \quad (3.12)$$

The solution of the above equation for a step index profile is given in the next section.

3.1.3 The Eigenvalue equation for Propagation Constants

In this section, we obtain the modal fields and the corresponding propagation constants for a step index fiber for which the refractive index variation is given by equation (3.3). For such a fiber it is possible to obtain rigorous solutions of the vector equations [see, e.g., Snyder and Love (1988), Sodha and Ghatak (1977), Chapter 4] However, most practical fibers used in communication are weakly guiding as stated in above section [53], in such a case the radial part of the transverse component of the electric field satisfies equation (3.12) and the complete transverse field is given by

$$\psi(r, \phi, z, t) = R(r) e^{i(\alpha x - \beta z)} \begin{cases} \cos l\phi \\ \sin l\phi \end{cases} \quad (3.13)$$

If we use equation (3.3) for $n^2(r)$ in equation (3.12), we obtain

$$r^2 \frac{d^2 R}{dr^2} + r \frac{dR}{dr} + \left(U^2 \frac{r^2}{a^2} - l^2 \right) R = 0: \quad 0 < r < a \quad (3.14)$$

and

$$r^2 \frac{d^2 R}{dr^2} + r \frac{dR}{dr} + \left(W^2 \frac{r^2}{a^2} + l^2 \right) R = 0: \quad r > a \quad (3.15)$$

where

$$U = a(k_0^2 n_1^2 - \beta^2)^{1/2} \quad (3.16)$$

$$W = a(\beta^2 - k_0^2 n_2^2)^{1/2} \quad (3.17)$$

and the normalized waveguide parameter V is defined by

$$V = (U^2 + W^2)^{1/2} = k_0 a (n_1^2 - n_2^2)^{1/2} \quad (3.18)$$

Guided modes correspond to $n_2^2 k_0^2 < \beta^2 < n_1^2 k_0^2$ and therefore for guided modes both U and W are real.

Equations (3.14) and (3.15) are of the standard form of Bessel's equation [see

Appendix A]. The solutions of equation (3.14) are $J_l(x)$ and $Y_l(x)$ where $x = Ur/a$. The solution has to be rejected since it diverges as $x \rightarrow 0$. The solutions of equation (3.15) are the modified Bessel functions $K_l(\bar{x})$ and $I_l(\bar{x})$ with the asymptotic forms

$$K_l(\bar{x}) \xrightarrow{\bar{x} \rightarrow \infty} \left(\frac{\pi}{2\bar{x}} \right)^{\frac{1}{2}} e^{-\bar{x}} \quad (3.19)$$

$$I_l(\bar{x}) \xrightarrow{\bar{x} \rightarrow \infty} \left(\frac{1}{2\pi\bar{x}} \right)^{\frac{1}{2}} e^{\bar{x}} \quad (3.20)$$

where $\bar{x} = Wr/a$. Obviously, the solution $I_l(\bar{x})$, which diverges as $\bar{x} \rightarrow \infty$, has to be rejected. Thus, the transverse dependence of the modal field is given by

$$\psi(r, \phi) = \begin{cases} \frac{A}{J_l(U)} J_l\left(\frac{Ur}{a}\right) \begin{bmatrix} \cos l\phi \\ \sin l\phi \end{bmatrix}; r < a \\ \frac{A}{K_l(W)} K_l\left(\frac{Wr}{a}\right) \begin{bmatrix} \cos l\phi \\ \sin l\phi \end{bmatrix}; r > a \end{cases} \quad (3.21)$$

where we have assumed the continuity of ψ at the core-cladding interface. Continuity of $\partial\psi/\partial r$ at $r = a$ leads to the following eigenvalue equation for β :

$$\frac{UJ_l'(U)}{J_l(U)} = \frac{WK_l'(W)}{K_l(W)} \quad (3.22)$$

Using the identities

$$\pm UJ_l'(U) = lJ_l(U) - UJ_{l\pm 1}(U) \quad (3.23)$$

$$\pm WK_l'(W) = lK_l(W) \mp WK_{l\pm 1}(W) \quad (3.24)$$

$$J_{l\pm 1}(U) = (2l/U)J_l(U) - J_{l-1}(U) \quad (3.25)$$

and

$$K_{l\pm 1}(W) = (2l/W)K_l(W) + K_{l-1}(W) \quad (3.26)$$

equation (3.22) can be written in either of the following two forms

$$U \frac{J_{l\pm 1}(U)}{J_l(U)} = W \frac{K_{l\pm 1}(W)}{K_l(W)} \quad (3.27)$$

or

$$U \frac{J_{l-1}(U)}{J_l(U)} = -W \frac{K_{l-1}(W)}{K_l(W)} \quad (3.28)$$

The mode condition (3.27) is mathematically equivalent to (3.28) if we use the recurrence relation of the Bessel functions. In the following section, we will use equation (3.28) for studying the modes.

3.1.4 Numerical Implementation and Simulation Results

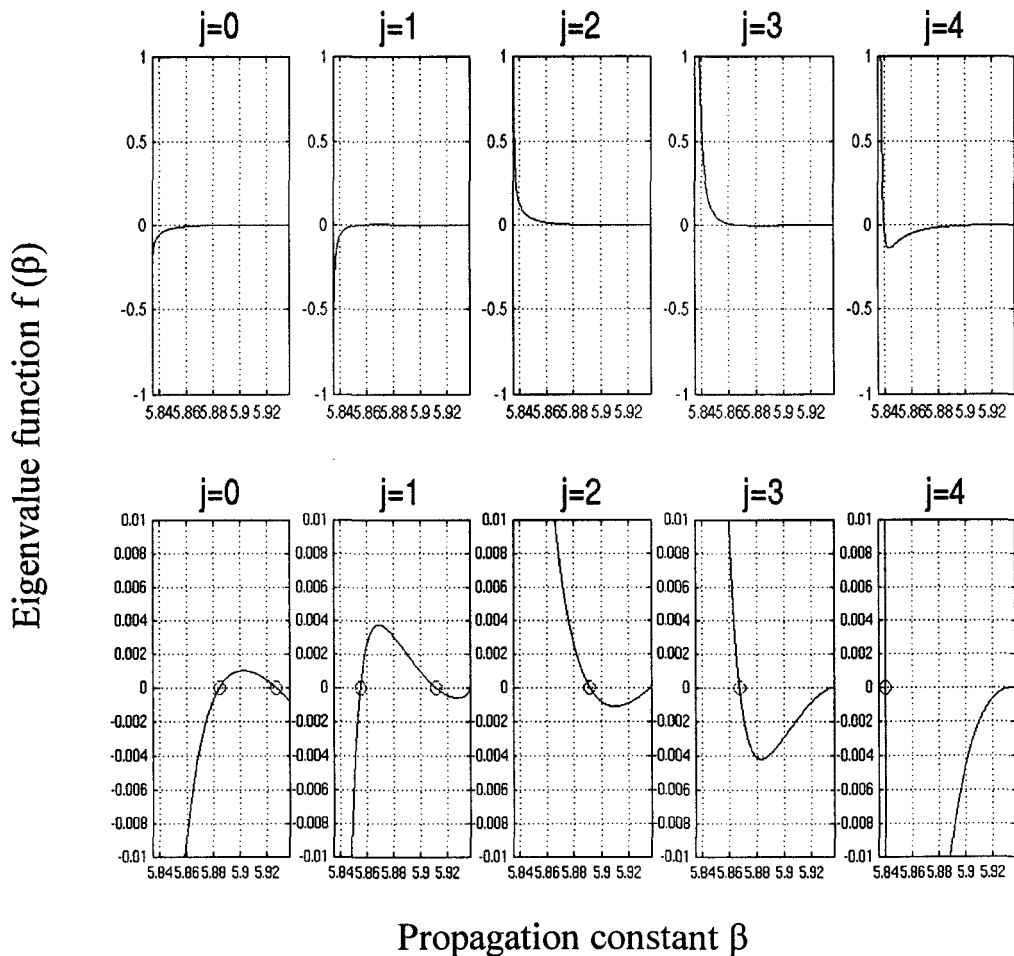


Fig. 3-2 Root finding of solving the eigenvalue equation (3.28) for $V = 6.58998$. There are 10 subfigure in two rows, five columns each column corresponds to one order $j=0,1,2,3,4$ from left to right. In first row (up row), give the global view the curve (y axis -1,1), in second row (bottom row), give a zoom in view around zeros (y axis -0.01, 0.01) with circle demark the root position, there are clearly 7 roots for $A = 6$.

The calculation of the modal field distributions and the corresponding propagation constants are of extreme importance in the study of waveguides. However, Eq. (3-28) is a transcendental equation which is not able to obtain analytical solution. This characteristic equation may be solved graphically by plotting its right- and left- hand sides (RHS and LHS) versus U and finding the intersections. Here, the equation is solved numerically, by applying bracketing and bisection methods on the basis of intermediate value theorem (the detailed root-finding algorithm and numerical procedure are included in Appendix B). The resulted graph, as an instance for root finding, is plotted in Fig. 3-2 showing there are seven roots searched with the selected condition.

Simulations of the radial distributions of optical fields are shown from Figs. 3-3 to Fig. 3-5. The fiber parameters are illustrated in the every figure caption respectively.

Obviously, each mode has a distinct radial distribution. The semi-logarithm E fields make known the varying rate of the field distribution tendency. The intensity, which is illustrated in (c) of Figures 3-3 to 3-5, is proportional to the amplitude square. It is noted that the higher order modes have a greater fraction of power in the cladding.

The calculated propagation constants are shown in Figures 3-6 and 3-7 as a function of wavelength λ . This is a straight-line parallel function with jumps at the wavelength of around $1.54946\mu\text{m}$. Above this wavelength, root corresponding to LP₁₂ mode will not be supported in the fiber any more.

The number of modes that can exist in a fiber as a function of normalized frequency V may be conveniently represented in terms of a normalized propagation constant b defined by

$$b = \frac{\frac{\beta^2}{k_0^2} - n_2^2}{n_1^2 - n_2^2} = \frac{w^2}{V^2} \quad (3.29)$$

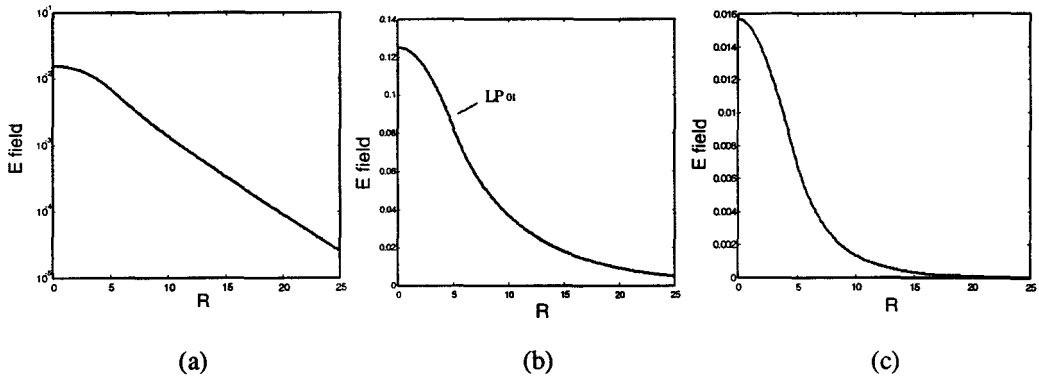


Fig. 3-3 Radial distributions of the fundamental LP_{01} mode in the transverse plane (a) Semi-logarithm E field (b) The electrical field amplitude (c) The modal field intensity. The parameters have been selected as: $n_1 = 1.46$, $n_2 = 1.45854$, $a = 5\mu\text{m}$.

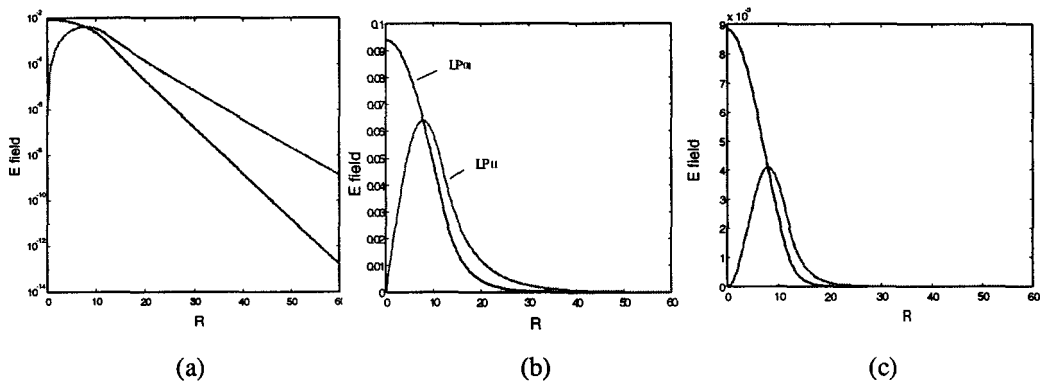


Fig. 3-4 Radial distributions of the LP_{01} and LP_{11} modes (a) Semi-logarithm E field (b) The electrical field amplitude (c) The modal field intensity. The parameters are: $n_1 = 1.46$, $n_2 = 1.45854$, $a = 12\mu\text{m}$.

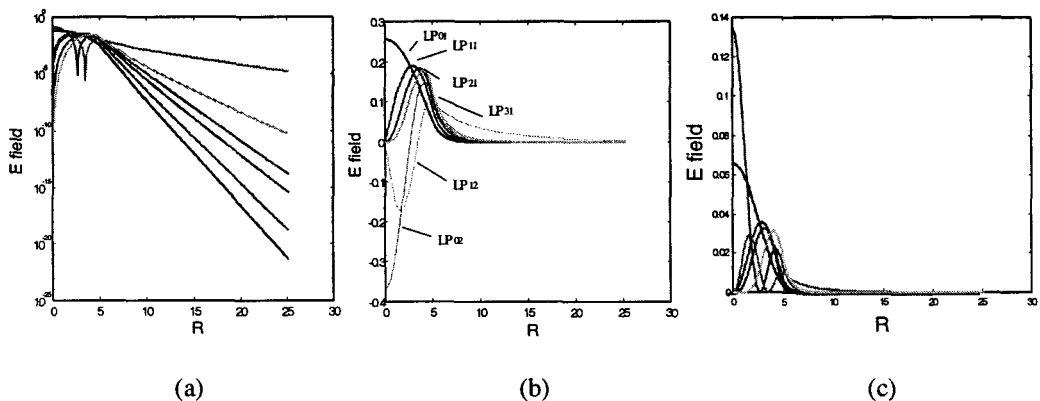


Fig. 3-5 Radial distributions of some lower-order modes in a step index fiber (a) Semi-logarithm E field (b) The electrical field amplitude (c) The modal field intensity. The parameters are set to be: $n_1 = 1.46$, $n_2 = 1.4348$, $a = 5.04\mu\text{m}$.

$$\text{Thus } w = V\sqrt{b} \quad (3.30)$$

$$\text{and } U = \sqrt{V^2 - w^2} = V\sqrt{1-b} \quad (3.31)$$

Since for guided (or bound) modes

$$n_2^2 < \frac{\beta^2}{k_0^2} < n_1^2 \quad (3.32)$$

We will have

$$0 < b < 1 \quad (3.33)$$

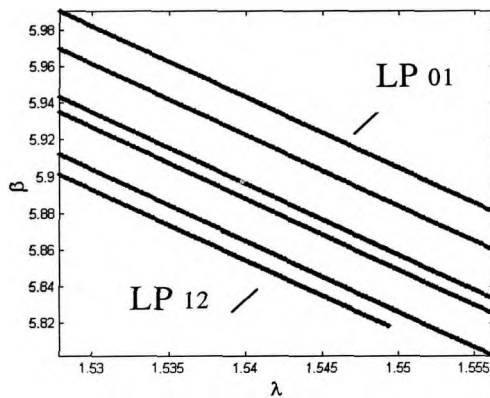


Fig. 3-6 The propagation constants as a function of wavelength in few mode fiber

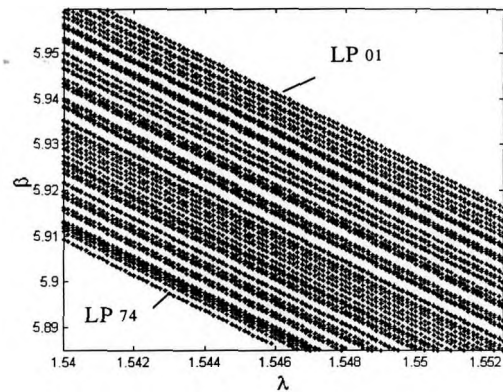


Fig. 3-7 The propagation constants as a function of wavelength in multimode fiber

In table 3-1 we have tabulated the values of b , U , and W for $1.5 < V < 2.5$ for the fundamental mode of a step index fiber for reference and verification.

A plot of b as a function of V is shown in Fig. 3-8 for the first 20 guided modes of the weakly guiding fiber. This figure shows that at a particular V value there are only a finite number of guided modes.

Each mode can exist only for values of V that exceed a certain limiting value. The condition $b = 0$ (i.e., $\beta^2 = k_0^2 n_2^2$) corresponds to what is known as the mode cut-off.

For $b < 0$, $\beta^2 < k_0^2 n_2^2$ and the fields are oscillatory even in the cladding and we have

Table 3-1 Variations of b , U , and W for the fundamental mode of the step index fiber

V	b	U	W
1.500000025587	0.229247764535	1.316887462527	0.7181973877705121
1.525000026014	0.239553491688	1.329854680493	0.7463990943944843
1.550000026440	0.249798255093	1.342519926715	0.7746872454974203
1.575000026867	0.259971371692	1.354892460207	0.8030513718966095
1.600000027293	0.270063361281	1.366981294265	0.8314819471681059
1.625000027720	0.280065853335	1.378795188161	0.8599703013431984
1.650000028146	0.289971498089	1.390342642085	0.8885085427169480
1.675000028572	0.299773882301	1.401631894790	0.9170894870324725
1.700000028999	0.309467449899	1.412670923420	0.9457065933570539
1.725000029425	0.319047427612	1.423467445129	0.9743539060196367
1.750000029852	0.328509755568	1.434028920116	1.0030260020314865
1.775000030278	0.337851022749	1.444362555810	1.0317179434625257
1.800000030705	0.347068407149	1.454475311929	1.0604252342938703
1.825000031131	0.356159620461	1.464373906234	1.0891437813114302
1.850000031558	0.365122857046	1.474064820790	1.1178698586469402
1.875000031984	0.373956746962	1.483554308594	1.1466000756113006
1.900000032411	0.382660312822	1.492848400457	1.1753313474992093
1.925000032837	0.391232930202	1.501952912039	1.2040608690762005
1.950000033263	0.399674291401	1.510873450964	1.2327860904880332
1.975000033690	0.407984372278	1.519615423936	1.2615046953577518
2.000000034116	0.416163401968	1.528184043825	1.2902145808599403
2.025000034543	0.424211835244	1.536584336656	1.3189138395823621
2.050000034969	0.432130327326	1.544821148492	1.3476007430041650
2.075000035396	0.439919710950	1.552899152170	1.3762737264372642
2.100000035822	0.447580975497	1.560822853873	1.4049313752925359
2.125000036249	0.455115248033	1.568596599525	1.4335724125464377
2.150000036675	0.462523776096	1.576224581002	1.4621956872958721
2.175000037101	0.469807912074	1.583710842140	1.4908001643006101
2.200000037528	0.476969099053	1.591059284549	1.5193849144221081
2.225000037954	0.484008858000	1.598273673221	1.5479491058768327
2.250000038381	0.490928776175	1.605357641940	1.5764919962302983
2.275000038807	0.497730496653	1.612314698484	1.6050129250651162
2.300000039234	0.504415708870	1.619148229632	1.6335113072630387
2.325000039660	0.510986140101	1.625861505972	1.6619866268469436
2.350000040087	0.517443547785	1.632457686520	1.6904384313337673
2.375000040513	0.523789712623	1.638939823140	1.7188663265546940
2.400000040940	0.530026432389	1.645310864790	1.7472699719029194
2.425000041366	0.536155516367	1.651573661579	1.7756490759733334
2.450000041792	0.542178780399	1.657730968646	1.8040033925623580
2.475000042219	0.548098042443	1.663785449870	1.8323327169992973
2.500000042645	0.553915118634	1.669739681403	1.8606368827837703

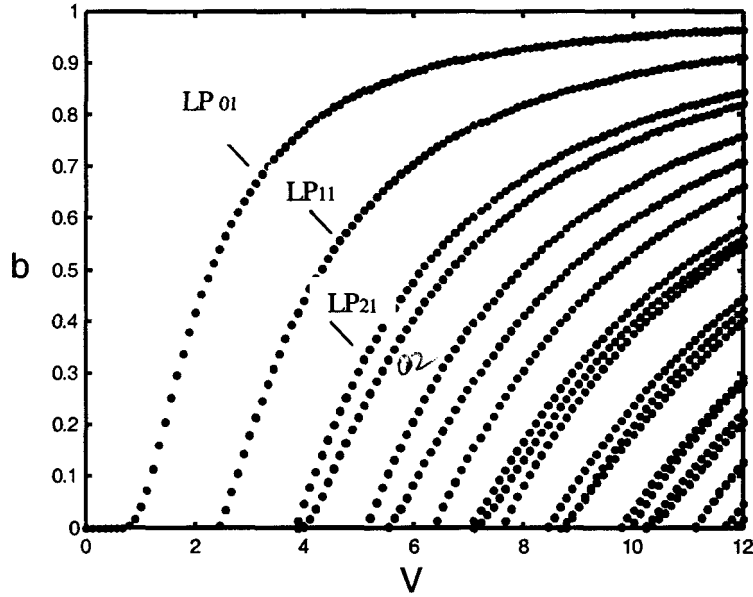


Fig. 3-8 Normalized propagation constant b as function of normalized frequency V for the guided modes of the optical fiber.

what are known as radiation modes. Obviously, at cut-off $\beta = k_0 n_2$ implying

$$b = 0, w = 0, U = V = V_c \quad (3.34)$$

The cutoffs of various modes are determined from the following equations

$$l = 0 \text{ modes: } J_l(V_c) = 0$$

$$l = 1 \text{ modes: } J_0(V_c) = 0$$

$$l \geq 2 \text{ modes: } J_{l-1}(V_c) = 0; V_c \neq 0 \quad (3.35)$$

As is obvious from the above analysis and also from Fig. 3-8, it follows that the lowest-order mode, characterized by $l = 0$, has a cut off $V = 0$. In other words, the lowest-order mode has no cutoff and ceases to exist only when the core diameter is zero. This is the principle on which the single-mode fiber is based. This guided mode is referred to as the HE_{11} mode and is now labeled LP_{01} . The next mode of the type $l = 0$, cuts off when $J_1(V_c)$ next equals zero, that is, when $V \cong 3.8317$. The mode is labeled LP_{02} . The curves in Figure 3-8 are universal. The cutoff values of V for various LP_{lm} modes are given in Table 3-2 (because of its length, we put Table 3-2 in Appendix C).

Comparison of the linearly polarized mode results we got above with the exact modes in [35] shows that the linearly polarized modes are a superposition of $HE_{l+1,m}$ and $EH_{l-1,m}$ modes. Therefore, linearly polarized (LP) modes are actually such degenerate modes regardless of their TM, TE, EH, or HE field configuration. As we have seen, LP modes can be used as simpler but quite accurate approximation of the exact modes, based on the principle of weakly guided mode approximation. In this approximation, the electromagnetic field patterns and the propagation constants of the mode pairs or the mode groupings are very similar. In general, we have the following:

1. Each LP_{0m} mode is derived from an HE_{1m} mode.
2. Each LP_{1m} mode comes from TE_{0m} , TM_{0m} , and HE_{2m} modes.
3. Each LP_{lm} mode ($l \geq 2$) is from an $HE_{l+1,m}$ and $EH_{l-1,m}$ mode.
4. The $l = 0$ modes are two-fold degenerate corresponding to two independent states of polarization.
5. The $l \geq 1$ modes are four-fold degenerate because, for each polarization, the ϕ dependence could be either $\cos(l\phi)$ or $\sin(l\phi)$.

One of the most important advantages of using the linearly polarized mode is that the modes are almost transversely polarized and are dominated by one transverse electric field component (E_x or E_y) and one transverse magnetic field component (H_y or H_x).

3.1.5 Fractional Modal Power in the Core

A final quality of interest discussed here for step index fibers is the fractional power flow in the core and cladding for a given mode. The relative amounts of power flowing in the core and the cladding can be obtained by integrating the Poynting vector in the axial direction [53]

$$S_z = \frac{1}{2} \text{Re}(\vec{E} \times \vec{H}^*) \cdot \vec{e}_z \quad (3.36)$$

over the fiber cross section. Now, the power in the core of the fiber is given by

$$\begin{aligned}
 P_{core} &= const. \int_0^a \int_0^{2\pi} |\psi|^2 r dr d\phi \\
 &= \frac{2C}{J_l^2(U)} \int_0^a J_l^2\left(\frac{Ur}{a}\right) r dr \int_0^{2\pi} \cos^2 l\phi d\phi
 \end{aligned}$$

or

$$\begin{aligned}
 P_{core} &= C \frac{\pi a^2}{U^2} \frac{2}{J_l^2(U)} \int_0^U J_l^2(x) x dx \\
 &= C \pi a^2 \left[1 - \frac{J_{l-1}(U) J_{l+1}(U)}{J_l^2(U)} \right]
 \end{aligned} \tag{3.37}$$

where C is a constant and use has been made of standard integrals associated with Bessel functions. Similarly, the power in the cladding is given by

$$\begin{aligned}
 P_{clad} &= const. \int_0^\infty \int_0^{2\pi} |\psi|^2 r dr d\phi \\
 &= C \pi a^2 \left[\frac{K_{l-1}(W) K_{l+1}(W)}{K_l^2(W)} - 1 \right]
 \end{aligned} \tag{3.38}$$

The total power is

$$\begin{aligned}
 P_{tot} &= P_{core} + P_{clad} \\
 &= C \pi a^2 \frac{V^2}{U^2} \frac{K_{l+1}(W) K_{l-1}(W)}{K_l^2(W)}
 \end{aligned} \tag{3.39}$$

where use has been made of the equation

$$U^2 \frac{J_{l+1}(U) J_{l-1}(U)}{J_l^2(U)} = -W^2 \frac{K_{l+1}(W) K_{l-1}(W)}{K_l^2(W)} \tag{3.40}$$

which follows from the eigenvalue equations. The fractional power propagating in the core is thus given by

$$\eta_1 = \frac{P_{core}}{P_{tot}} = \left[\frac{W^2}{V^2} + \frac{U^2}{V^2} \frac{K_l^2(W)}{K_{l+1}(W) K_{l-1}(W)} \right] \tag{3.41}$$

Thus, the ratio of cladding power to the total power, $\eta_2 = P_{clad} / P_{tot}$, which measures the fraction of mode power flowing in the cladding layer can be obtained accordingly.

In Figures 3-9 and 3-10 we have plotted the fractional power contained in the core and in the cladding as a function of V for several modes respectively. From these figures it can be seen that the electromagnetic energy of a guided mode is carried

partly in the core and partly in the cladding. The further away a mode is from its cutoff frequency, the more concentrated its energy is in the core. Generally speaking, the power flow in the cladding decrease as V increases. In terms of label of LP_{lm} modes, P_{clad}/P associated with a particular mode increases when the mode subscript lm increases. Note that the fundamental mode LP_{01} is best confined.

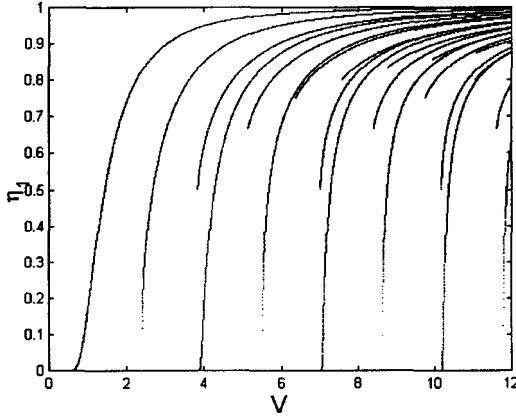


Fig.3-9 Fractional power contained in the core as a function of the frequency parameter V .

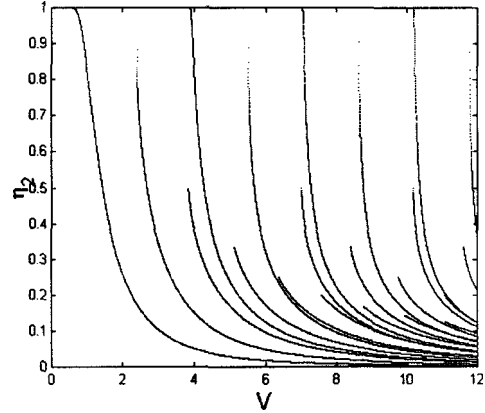


Fig.3-10 Fractional power contained in the cladding as a function of the frequency parameter V .

Throughout Section 3.1, we study and discuss the propagation characteristics of step index fibers. The simulation results given in this section are in exact consistent with typical results in literatures [35, 53, 54], etc., such as Figs. 3-5, 3-8, 3-9 and 3-10, Tables 3-1 and 3-2, and so forth.

3.2 Mode Modeling and Simulation for Graded Index Fibers

Index grading is an ingenious method for reducing the pulse spreading caused by the differences in the group velocities of the modes of multimode fiber.

A versatile refractive index profiles is generally characterized by the power-law function

$$n^2(r) = \begin{cases} n_1^2[1 - 2\Delta(r/a)^q] & 0 \leq r \leq a \\ n_1^2(1 - 2\Delta) = n_2^2(r \geq a) & r \geq a \end{cases} \quad (3.42)$$

where a represents the radius of the core, Δ is the relative index difference, n_1 and n_2 represent the axial and cladding refractive indices, respectively, and q , called the grade profile parameter, determines the steepness of the profile. For $q = 1$, $n^2(r)$ is linear, and for $q = 2$ it is quadratic. As $q \rightarrow \infty$, $n^2(r)$ approaches a step function, as illustrated in Fig. 3-11 [51].

In this section, we examine the propagation of light in an infinitely extended parabolic index fiber characterized by the following refractive index variation because of its popularity and importance in realistic applications.

$$n^2 = n_1^2 \left[1 - 2\Delta \left(\frac{r}{a} \right)^2 \right] \quad (3.43)$$

or, in Cartesian coordinates,

$$n^2 = n_1^2 \left[1 - 2\Delta \frac{x^2 + y^2}{a^2} \right] \quad (3.44)$$

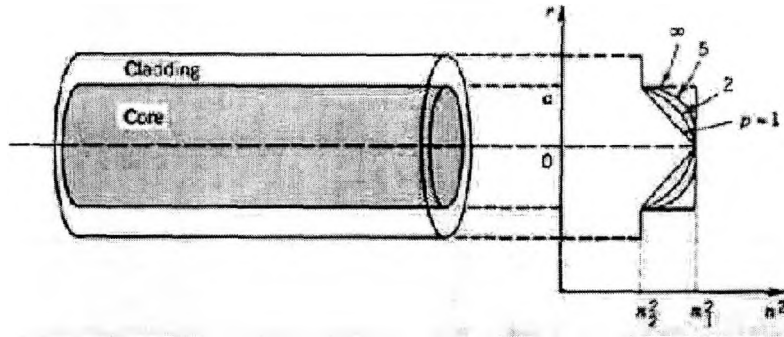


Fig. 3-11 Power-law refractive index profile $n^2(r)$ for different values of p (Bahaa E. A. Saleh and Malvin Carl Teich).

3.2.1 Model Analysis of Parabolic Index Fibers

We now present a detailed modal analysis for a parabolic index fiber. If we substitute equation (3.43) in the scalar wave equation we obtain [53]

$$\nabla^2 \Psi = \frac{n_1^2}{c^2} \left[1 - 2\Delta \left(\frac{x^2}{a^2} + \frac{y^2}{a^2} \right) \right] \frac{\partial^2 \Psi}{\partial t^2} \quad (3.45)$$

We assume a modal solution of the form

$$\Psi(x, y, z, t) = \psi(x, y)e^{i(\alpha x - \beta z)} \quad (3.46)$$

Then equation (3.45) becomes

$$\frac{\partial^2 \psi}{\partial x^2} + \frac{\partial^2 \psi}{\partial y^2} + \left\{ k_0^2 n_1^2 \left[1 - 2\Delta \left(\frac{x^2}{a^2} + \frac{y^2}{a^2} \right) \right] - \beta^2 \right\} \psi = 0 \quad (3.47)$$

We use the method of separation of variables and write

$$\psi(x, y) = X(x)Y(y) \quad (3.48)$$

If we substitute the above solution in equation (3.47) and divide by XY we obtain

$$\left(\frac{1}{X} \frac{d^2 X}{dx^2} - k_0^2 n_1^2 \frac{2\Delta}{a^2} x^2 \right) + \left(\frac{1}{Y} \frac{d^2 Y}{dy^2} - k_0^2 n_1^2 \frac{2\Delta}{a^2} y^2 \right) + (k_0^2 n_1^2 - \beta^2) = 0 \quad (3.49)$$

The variables have indeed separated out and we may write

$$\left(\frac{1}{X} \frac{d^2 X}{dx^2} - k_0^2 n_1^2 \frac{2\Delta}{a^2} x^2 \right) = -K_1 \quad (3.50)$$

and

$$\left(\frac{1}{Y} \frac{d^2 Y}{dy^2} - k_0^2 n_1^2 \frac{2\Delta}{a^2} y^2 \right) = -K_2 \quad (3.51)$$

where K_1 and K_2 are constants and

$$\beta^2 = k_0^2 n_1^2 - K_1 - K_2 \quad (3.52)$$

We now use the variables

$$\xi = \gamma x, \quad \eta = \gamma y \quad (3.53)$$

with

$$\gamma = \left[n_1 k_0 \frac{\sqrt{2\Delta}}{a} \right]^{1/2} = \frac{\sqrt{V}}{a} \quad (3.54)$$

where

$$V = n_1 k_0 a (2\Delta)^{1/2} \quad (3.55)$$

represents the waveguide parameters. Thus

$$\begin{aligned} d^2 X / d\xi^2 + (\Lambda_1 - \xi^2) X(\xi) &= 0 \\ d^2 Y / d\eta^2 + (\Lambda_2 - \eta^2) Y(\eta) &= 0 \end{aligned} \quad (3.56)$$

where

$$\Lambda_1 = \frac{K_1}{\gamma^2} \quad (3.57)$$

and

$$\Lambda_2 = \frac{K_2}{\gamma^2} \quad (3.58)$$

For bounded solutions—that is, for $X(\xi)$ and $Y(\eta)$ to tend to zero as $\xi, \eta \rightarrow \pm\infty$ (i.e., $x, y \rightarrow \pm\infty$)—we must have

$$\Lambda_1 = 2m + 1; \quad m = 0, 1, 2, \dots \quad (3.59)$$

and

$$\Lambda_2 = 2n + 1; \quad n = 0, 1, 2, \dots \quad (3.60)$$

The corresponding modal distributions $X(x)$ and $Y(y)$ are the Hermite-Gauss functions. Thus, we obtain the following expressions for mode profiles and corresponding propagation constants,

$$\psi_{mn}(x, y) = \left[N_m H_m(\xi) e^{-\frac{1}{2}\xi^2} \right] \left[N_n H_n(\eta) e^{-\frac{1}{2}\eta^2} \right] \quad (3.61)$$

$$\beta_{mn} = k_0 n_1 \left[1 - \frac{2(m+n+1)}{k_0 n_1} \sqrt{\frac{2\Delta}{a^2}} \right]^{1/2} \quad (3.62)$$

where $m, n = 0, 1, 2, \dots$ and

$$N_m = \left[\frac{\gamma}{2^m m! \sqrt{\pi}} \right]^{1/2} = \left[\frac{\sqrt{V}/a}{2^m m! \sqrt{\pi}} \right]^{1/2} \quad (3.63)$$

represents the normalization constant. Different values of m and n correspond to different modes of the fiber.

We should mention here that in an actual parabolic index core fiber the refractive index is given by equation (3.43) only for $r < a$ beyond which it has a constant values equal to

$$n = n_1(1 - 2\Delta)^{1/2} (= n_2) \quad \text{for } x^2 + y^2 > a^2$$

and the solutions given by equations (3.61) and (3.62) are then not exact solutions for

such a profile. The guided modes will correspond to only those values of m and n for which

$$k_0 n_2 < \beta_{mn} < k_0 n_1 \quad (3.64)$$

The lowest order mode that corresponds to $m = 0, n = 0$ is given by

$$\psi_{00} = \frac{\gamma}{\sqrt{\pi}} e^{-\frac{1}{2}\gamma^2 r^2} = \frac{1}{a} \sqrt{\frac{V}{\pi}} e^{-\frac{1}{2}V(r/a)^2} \quad (3.65)$$

which has a Gaussian distribution.

3.2.2 Linearly Polarized Modes

In Section 3.1.2 we showed that the scalar modes of an optical fiber characterized by cylindrically symmetric refractive index distribution [$n = n(r)$] are described by the transverse field profile (see equation (3.13)) [53]

$$\Psi(r, \theta, z, t) = e^{i(\omega t - \beta z)} R(r) \begin{cases} \cos(l\phi) \\ \sin(l\phi) \end{cases} \quad (3.66)$$

and the propagation constant β along the fiber axis are obtained from the scalar wave equation

$$\frac{d^2 R}{dr^2} + \frac{1}{r} \frac{dR}{dr} + \left[k_0^2 n^2(r) - \beta^2 - \frac{l^2}{r^2} \right] R(r) = 0 \quad (3.67)$$

where $R(r)$ is the solution of the radial part of the wave equation, l is zero or positive integer, and denotes an azimuthal mode number. When positive integer m is assumed to be a radial mode number, the field of (l, m) mode R_{lm} is given by

$$R_{lm}(r) = N_{lm} L_{m-1}^l(\gamma^2 r^2) \cdot r^l \cdot \exp\left[-\frac{1}{2}\gamma^2 r^2\right] \quad (3.68)$$

where

$$N_{lm} = \gamma^{l+1} \left[\frac{2(m-1)!}{\Gamma(l+m)} \right]^{1/2} \quad (3.69)$$

represents the normalization constant so that

$$\int_0^\infty |R_{lm}(r)|^2 r dr = 1 \quad (3.70)$$

The functions $L_n^k(x)$ are the associated Laguerre polynomials given by

$$L_n^k(x) = \sum_{p=0}^n (-1)^p \frac{\Gamma(n+k+1)}{(n-p)! \Gamma(p+k+1) p!} x^p \quad (3.71)$$

Thus

$$\left. \begin{aligned} L_0^k(x) &= 1, L_1^k(x) = k+1-x \\ L_2^k(x) &= \frac{1}{2}(k+2)(k+1) - (k+2)x + \frac{1}{2}x^2 \end{aligned} \right\} \quad (3.72)$$

and so forth. The corresponding propagation constants are given by

$$\beta_{lm} = k_0 n_1 \left[1 - \frac{2(2m+l-1)}{k_0 n_1} \sqrt{\frac{2\Delta}{a^2}} \right]^{1/2} \quad (3.73)$$

The LP₀₁ mode is given by equation (3.65). Note that for LP_{lm} modes $l = 0, 1, 2, \dots$ and $m = 1, 2, 3, \dots$. Further,

$$\psi_{11}(r, \phi) = \sqrt{\frac{2}{\pi}} \gamma^2 r e^{-\frac{1}{2}\gamma^2 r^2} \begin{cases} \cos \phi \\ \sin \phi \end{cases} \quad (3.74)$$

where the subscripts now refer to the values of l and m . In writing the total field we assume normalization in both r and ϕ coordinates. The next higher mode is given by

$$\psi_{21}(r, \phi) = \frac{\gamma}{\sqrt{\pi}} (\gamma^2 r^2) e^{-\frac{1}{2}\gamma^2 r^2} \begin{cases} \cos 2\phi \\ \sin 2\phi \end{cases} \quad (3.75)$$

$$\psi_{02}(r, \phi) = \sqrt{\frac{2}{\pi}} (\gamma^2 r^2 - 1) e^{-\frac{1}{2}\gamma^2 r^2} \quad (3.76)$$

Similarly, we can consider other higher order modes.

3.2.3 Computer Simulation and Results Discussion

Using the above results of the MMF analysis, the computer simulations to a parabolic-index fiber are carried out. The fiber parameters are extracted from [8], which are: $n_1 = 1.462$, $n_2 = 1.4483$, $a = 25\mu\text{m}$.

The simulated modal field distributions are displayed in Fig. 3-12, likewise we also give three representative field patterns as dealt with step index conditions to depict the field variation.

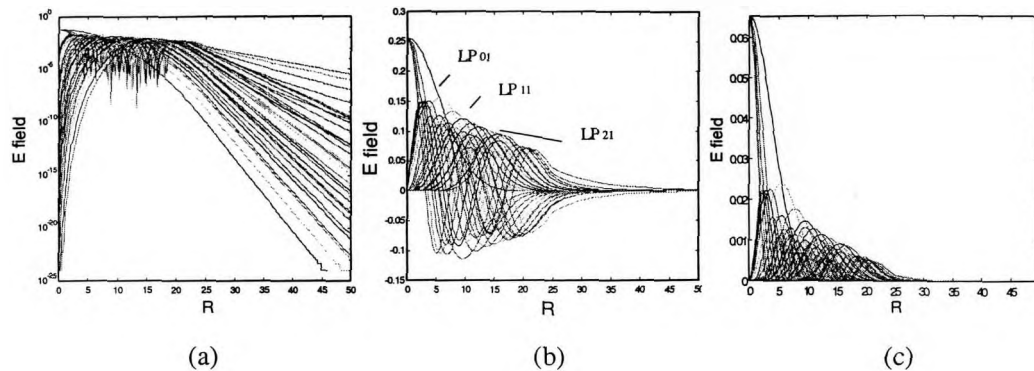


Fig. 3-12 Radial distributions of lower-order and higher-order modes in multimode fiber (a) Semi-logarithm E field (b) The electrical field amplitude (c) The modal field intensity.

The Dependence of the propagation constants β on the wavelength λ is calculated based on above discussed MMF model as shown in Fig. 3-13 and further compared with the same dependence in step index fiber keeping all the physical conditions identical, see Fig. 3-14. The corresponding β values for parabolic profile fiber are marked schematically in Table 3-3.

By observing Table 3-3 and comparing the above two Figures, we may note the following points:

1. On the one hand, both function curves in Figures 3-13 and 3-14 are parallel straight lines; however, on the other hand, the separations between the neighboring parallels in Fig. 3-13 are almost exactly alike whereas in Fig. 3-14 the every separation between two adjoining lines are very different from each other.
2. Within the same investigated β and λ , only 10 different propagation constants can be observed in Fig. 3-13 at a given wavelength; in contrast, there exhibit totally 56 diverse values of propagation constants in Fig. 3-7 which is the source of Fig. 3-14. In other words, it is indicated that the total number of modes in our step index MMF far exceeds the mode number in the corresponding graded index MMF.

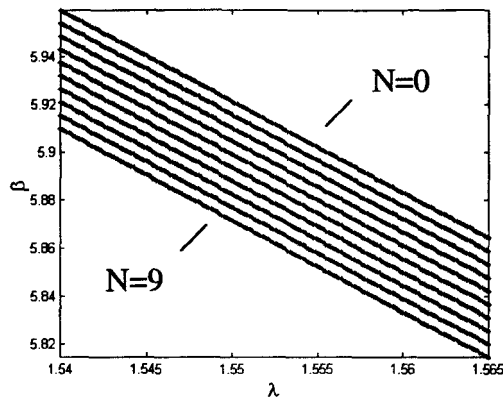


Fig.3-13 The propagation constants as a function of wavelength in a multimode parabolic graded-index fiber.

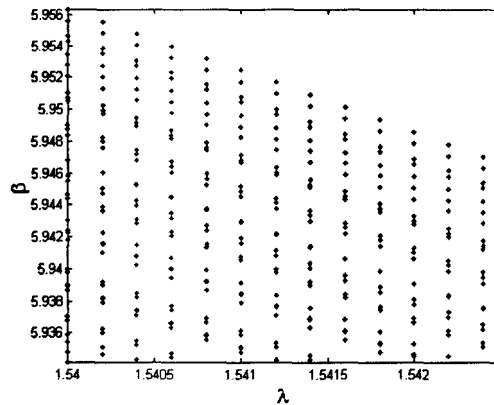


Fig.3-14 An broadened window of the propagation constants dependence on wavelength in a multimode step-index fibers whose full screen image shown previously in Fig. 3-7.

3. Table 3-3 shows that despite 30 LP_{lm} modes existed in our graded index fiber, some of them possess the same propagation constant. That means a further degeneracy occurs among these bound modes in MMF based on the LP mode.

Next, the reason which these features are resulted from is discussed from the point of WKB view. The WKB method is an approximation approach applicable to multimode fibers that have profiles so that the wave equation is separable to one-dimensional equations and when the variation of the refractive index is small in distances $\sim \lambda$. From the WKB analysis, the propagation constant along the fiber axis is specified only by a bound mode number ν as

$$\beta_{\nu} \approx n_1 k_0 \left[1 - 2 \left(\frac{\nu}{M} \right)^{q/(q+2)} \Delta \right]^{1/2}, \quad \nu = 1, 2, \dots, M \quad (3.77)$$

Since in a weakly guiding fiber whose Δ is enough smaller than unity, i.e., $\Delta \ll 1$, the approximation $(1+\delta)^{1/2} \approx 1+1/2 \delta$ (when $|\delta| \ll 1$) can be applied to (3.77), yielding

Table 3-3 Propagation constant values corresponding to Fig. 3-13

1.550000000000	20.268339700577	205.402797108985	30
1	0	1	5.920975125586 1.460646311700
6	1	1	5.915482632424 1.459291367673
2	0	2	5.909985034770 1.457935164418
11	2	1	5.909985034770 1.457935164418
7	1	2	5.904482318366 1.456577698418
15	3	1	5.904482318366 1.456577698418
3	0	3	5.898974468888 1.455218966139
12	2	2	5.898974468888 1.455218966139
19	4	1	5.898974468888 1.455218966139
8	1	3	5.893461471944 1.453858964031
16	3	2	5.893461471944 1.453858964031
22	5	1	5.893461471944 1.453858964031
4	0	4	5.887943313075 1.452497688527
13	2	3	5.887943313075 1.452497688527
20	4	2	5.887943313075 1.452497688527
25	6	1	5.887943313075 1.452497688527
9	1	4	5.882419977754 1.451135136043
17	3	3	5.882419977754 1.451135136043
23	5	2	5.882419977754 1.451135136043
27	7	1	5.882419977754 1.451135136043
5	0	5	5.876891451386 1.449771302979
14	2	4	5.876891451386 1.449771302979
21	4	3	5.876891451386 1.449771302979
26	6	2	5.876891451386 1.449771302979
29	8	1	5.876891451386 1.449771302979
10	1	5	5.871357719307 1.448406185717
18	3	4	5.871357719307 1.448406185717
24	5	3	5.871357719307 1.448406185717
28	7	2	5.871357719307 1.448406185717
30	9	1	5.871357719307 1.448406185717

$$\beta_v \approx n_1 k_0 \left[1 - \left(\frac{v}{M} \right)^{q/(q+2)} \Delta \right], \quad v = 1, 2, \dots, M \quad (3.78)$$

where M represents the number of propagating modes and is usually calculated by the equation

$$M \approx \frac{q}{q+2} n_1^2 k_0^2 a^2 \Delta = \frac{q}{q+2} \frac{V^2}{2} \quad (3.79)$$

In the step-index fiber ($q = \infty$),

$$\beta_\nu \approx n_1 k_0 \left[1 - \frac{\nu}{M} \Delta \right], \quad \nu = 1, 2, \dots, M \quad (3.80)$$

$$\text{and } M \approx \frac{V^2}{2} \quad (3.81)$$

In our designed example for step-index fiber, the number of modes is indeed 206 within the wavelength range.

For graded-index MMF, $q = 2$

$$\beta_\nu \approx n_1 k_0 \left[1 - \left(\frac{\nu}{M} \right)^{1/2} \Delta \right], \quad \nu = 1, 2, \dots, M \quad (3.82)$$

the number of modes M given by (3.79) becomes

$$M \approx \frac{V^2}{4} \quad (3.83)$$

It is evident that for a given value of the waveguide parameter V , the total number of guided modes in step-index ($q = \infty$) fiber is twice as many as in a parabolic index ($q = 2$) fiber. In the case of our MMF, the total number of modes M is 103 which is just half of the same V step-index fiber to our wavelength extent. However, some of these modes have almost the same propagation constant as we have seen in Table 3-3. Therefore, we introduce the concept of principal mode: the modes having the same propagation constant is classified into the same principal mode. The propagation constant for the N th principal mode is approximated by the equation

$$\beta_N \approx n_1 k_0 \left\{ -2\Delta [N/F(\alpha)]^{2q/(q+2)} \right\}^{1/2}, \quad N = 1, 2, \dots, F \quad (3.84)$$

where the maximum principal mode number $F(\alpha)$ is given by

$$F(\alpha) \approx \sqrt{\frac{q}{q+2}} a k_0 n_1 \sqrt{\Delta} \quad (3.85)$$

As is apparent from the above analysis and also from Fig. 3-14, for our graded-index

MMF, there 10 principal modes are bound at around $1.55\mu\text{m}$. A general approximation for our modal analysis and simulation is that of using the LP mode description with the assumption of ideal step- and parabolic- graded index profile. Although we have not made a detailed study of limitations that are due to the LP mode approximation, for the small core-cladding difference in the fiber we feel that this is hardly a serious limitation even considering the fact that the approximation should give rise to the results to some extent.

To sum up, we give a more general sketch map to compare the propagation characteristics between step-index and graded-index fibers, as illustrated in Fig. 3-15 [51]. It is shown in Fig. 3-15 that the dispersion effect of graded index fibers is much lower than that of step-index fibers owing to its higher degeneracy in comparison with step-index fiber.

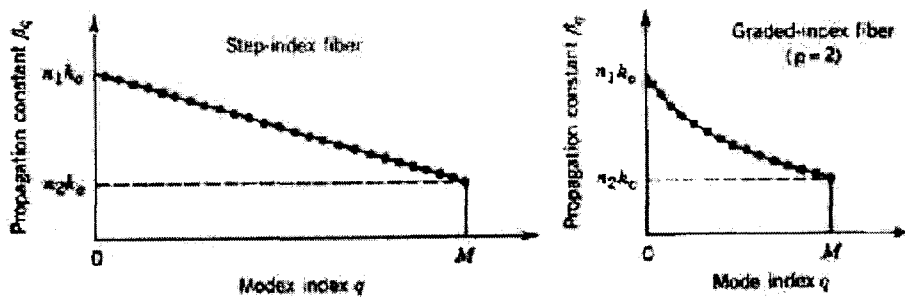


Fig. 3-15 Comparison of the propagation constant β_v between step-index fiber and graded-index fiber on the mode index $\nu = 1, 2, \dots, M$ (Bahaa E. A. Saleh and Malvin Carl Teich).

In this section, the propagation characteristics of graded index fibers are studied. The computed results whose wavelguide parameters were selected from [8] are identical to the reported results in reference [8]. In the following, we will come up to the further consideration on excitation condition of guided modes, which provides an accurate determination of mode power distribution in an either step-index fiber or a graded-index fiber based on numerical processing.

3.2.4 Excitation of Guided Modes

We start with the wave equation, which takes the form [53]

$$d^2\psi_m / dx^2 + [k_0^2 n^2(x) - \beta_m^2] \psi_m(x) = 0 \quad ; \quad m = 0, 1, 2, \dots \quad (3.86)$$

where $\psi_m(x)$ represents the field pattern corresponding to the propagation constant β_m , we have used the symbol $\psi_m(x)$ instead of the more complicated symbol $E_y^{(m)}(x)$. Using the condition that for guided modes $\psi_m(x)$ will go to zero as $x \rightarrow \pm\infty$, we can readily show that

$$\int_{-\infty}^{+\infty} \psi_m^*(x) \psi_k(x) dx = 0 \quad \text{for } m \neq k \quad (3.87)$$

which is known as the *orthogonality condition*. Since equation (3.86) is a linear equation, a constant multiple of $\psi_m(x)$ is also a solution and we can always choose the constant so that

$$\int_{-\infty}^{+\infty} |\psi_m(x)|^2 dx = 1 \quad (3.88)$$

which is known as the *normalization condition*. Combining equations (3.87) and (3.88) we get the *orthonormality condition*

$$\int_{-\infty}^{+\infty} \psi_m^*(x) \psi_k(x) dx = \delta_{mk} \quad (3.89)$$

where δ_{mk} is the Kronecker delta function defined by the following equation

$$\delta_{mk} = \begin{cases} 0 & \text{for } m \neq k \\ 1 & \text{for } m = k \end{cases} \quad (3.90)$$

Equation (3.89) represents the orthonormality condition satisfied by the discrete (guided) modes. The radiation modes (which form a continuum) also form an orthogonal set in the sense that

$$\int_{-\infty}^{+\infty} \psi_{\beta'}^*(x) \psi_{\beta}(x) dx = 0, \quad \text{for } \beta \neq \beta' \quad (3.91)$$

However the integral for $\beta = \beta'$ is not defined and the orthonormality condition is in terms of the Dirac delta function.

The important point is that the finite number of guided modes along with the continuum of radiation modes form a complete set of functions in the sense that any

“well-behaved” function of x can be expanded in terms of these functions — that is

$$\phi(x) = \sum_m c_m \psi_m(x) + \int c(\beta) \psi_\beta(x) d\beta \quad (3.92)$$

where the first term on the RHS represents a sum over discrete (guided) modes and the second term represents an integral over the continuum (radiation) modes. If we multiply equation (3.92) by $\psi_k^*(x)$ and integrate we will readily obtain

$$c_k = \int_{-\infty}^{+\infty} \psi_k^*(x) \phi(x) dx \quad (3.93)$$

where we have used equation (3.89). Now, let $E_y(x, z = 0)$ represent the actual incident field (polarized in the y -direction) at the entrance aperture of the waveguide ($z = 0$), The power launched in the m th mode will be

$$\begin{aligned} P_m &= (1/2\omega\mu_0) \beta_m |c_m|^2 \int_{-\infty}^{+\infty} |\psi_m(x)|^2 dx \\ &= (1/2\omega\mu_0) \beta_m \left| \int \psi_m^*(x) E_y(x, z = 0) dx \right|^2 \end{aligned} \quad (3.94)$$

As the beam propagates through the waveguide, the field in the region ($z > 0$) will be given by

$$E_y(x, z) = \sum_m c_m \psi_m(x) e^{-i\beta_m z} + \int c(\beta) \psi_\beta(x) e^{-i\beta z} d\beta \quad (3.95)$$

One can easily see that at an arbitrary value of z , the power in the m^{th} mode will be proportional to

$$|c_m e^{-i\beta_m z}|^2 = |c_m|^2 \quad (3.96)$$

which remains constant with z .

The above analysis predicting the excitation efficiencies of various modes will be utilized in the later chapters.

3.3 Summary

In this chapter we carried out a detailed modal analysis of both the step index fiber and the graded index fiber using electromagnetic theory. Based on this analysis, we developed efficient optical mode solver software. With our mode solver, we studied the propagation characteristics of various multimode optical fibers. The simulation results are in well consistent with literatures, which prove the validity of

our developed mode solver. The simulation results also reveal that modal dispersion can be reduced by grading the refractive index of the fiber core from a maximum value at its center to a minimum value at the core-cladding boundary. This is an optimum property of graded index fiber.

In practice, the developed mode solver is an effective part of the to-be-built integrated MMFBG simulator package. It will play an important role in building and performing the MMFBG modeling and simulation. Our mode solver can perform a wide range of functions including:

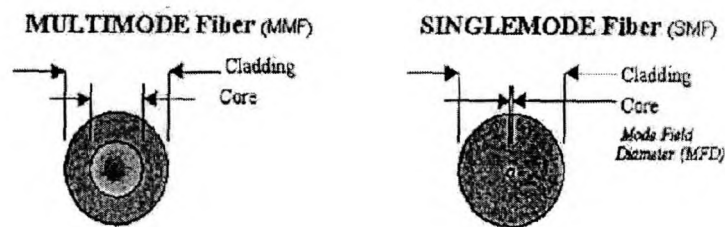
- (1) Searching roots for propagation constants β and calculates the corresponding effective index of refractive n_{eff} .
- (2) Describing the optical field distributions for all propagating fiber modes under any specific wavelength.
- (3) Simulating common fiber characteristics such as b - V relationship, i.e., normalized propagation constant b and normalized frequency V relationship.
- (4) Providing cut-off wavelengths of any chosen guided modes and simultaneously exhibits all critical points corresponding to root change.
- (5) Showing fractional power flow in the core and the cladding of various low-order and high-order modes.
- (6) Determining the mode power distribution among fiber supported modes by excitation condition simulation.
- (7) Calculating overlap integral between optical fields in a variety of concerned simulations.

Based on the above performance, our mode solver also provides the capability to calculate the coupling coefficients and evaluate the phase-matching condition for Bragg gratings, which will be further elaborated in the next chapter.

CHAPTER FOUR: MODELING AND SIMULATION OF FBGS IN MULTIMODE FIBER STRUCTURES

Fiber Bragg gratings represent a key element in the established and emerging fields of optical communications and optical fiber sensing. While fiber grating structures in single-mode fiber (SMF) are useful, Bragg gratings in multimode fibers (MMF) could have a dramatic impact on optical communication systems. In order to design fiber gratings for various applications, it is crucial to have tools for modeling and simulation, analysis and characterization of FBGs not only in single-mode fiber but also in multimode fiber structures.

For explicitness, the main features of both SMF and MMF are stated in comparison as follows [56].



Multimode (MMF), characterized by

- core/cladding diameters,
- step vs. graded index, → BW·D bandwidth-distance product
- Numerical Aperture (N.A.),
- nominal index of refraction,
- loss in dB/km,
- dispersion parameters

Advantages: low-precision terminations at lower cost, suitable for LED launch.

Disadvantages: high dispersion (low data rate), high loss.

Singlemode (SMF) (e.g. Corning SMF-28) characterized by

- Mode Field Diameter,
- Material dispersion and dispersion slope,
- NA → Numerical Aperture (N.A.)
- nominal index of refraction,
- loss in dB/km,

Advantages: low loss, dispersion.

Disadvantages: requires ELED or laser to hit small entry mode

We see in contrast to SMF that MM fiber has the advantage that it can couple large amount of light and is easy to handle, both the advantages arising from its large core size.

The most common mathematical model that governs wave propagation in gratings is the coupled-mode theory. The analysis of gratings based on single mode structure is well understood; a review is given in Chapter 2. As applications of coupled-mode theory now move on to the consideration of multimode structures, it is especially important to obtain a sound theoretical description before we implement the designing and deployment of numerical techniques.

4.1 Establishment of Coupled-Mode Theory Formulations for MMFBGs

In a normal step- or graded-index fiber with a finite glass cladding, coupling can occur between the bound core mode and the bound cladding mode of the fiber. But these effects are not considered in this work. This thesis presents an investigation primarily on the core modes of Bragg gratings in a multimode optical fiber. Fig. 4-1 illustrates a schematic diagram of distribution of core refractive index for FBG. The following investigation will establish on the cylindrical coordinates as shown in Fig. 4-2 [57].

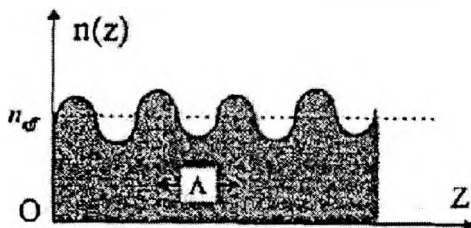


Fig. 4-1 Core refractive index distribution of fiber Bragg gratings [57].

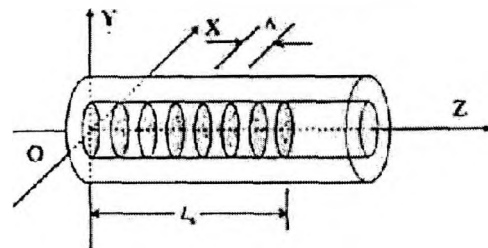


Fig. 4-2 Coordinates system for fiber gratings.

4.1.1 Generalized Coupled Mode Equations

Many phenomena occurring in physics or engineering can be viewed as coupled-mode processes. The coupled-mode formalism has also proved a very powerful tool in integrated optics, where it has helped in the understanding and analysis of a large variety of important phenomena and devices. *Snyder and Marcuse* [32, 54] have developed a coupled-mode formalism applicable to a large class of dielectric waveguides including channel guides and fibers, and they have used it in their analyses of optical fiber deformations. *Yariv* [58] has given a summary of coupled-wave phenomena that occur in integrated optics and presented a perturbation analysis of these for the TE modes in planar waveguides. *Kogelnik* [59] has also presented the coupled-mode formalism and its derivation in sufficient generality. He worked on the Vector equation and made no approximations in its derivation. But for optical fiber, because of the cylindrical symmetry (see Fig. 4-2) scalar equation analysis is suitable for this situation.

In the following, we will present and derive a generalized coupled mode equations based on scalar analysis and an important approximation — slowing varying envelope approximation (SVEA) is applied [54, 60, 61].

The waveguide modes satisfy the unperturbed wave equation

$$\nabla^2 \bar{E} = \mu_0 \epsilon_0 \epsilon_{ij} \frac{\partial^2 \bar{E}}{\partial t^2} \quad (4.1)$$

In order to derive the coupled mode equations, effects of perturbation have to be included, assuming that the modes of the unperturbed waveguide remain unchanged.

We begin with the wave equation

$$\nabla^2 \bar{E} = \mu_0 \epsilon_0 \frac{\partial^2 \bar{E}}{\partial t^2} + \mu_0 \frac{\partial^2 \bar{P}}{\partial t^2} \quad (4.2)$$

Assuming that wave propagation takes place in a perturbed system with a dielectric grating, the total polarization response of the dielectric medium described in Eq. (4.2) can be separated into two terms, unperturbed and the perturbed polarization, as

$$\bar{P} = \bar{P}_{\text{unpert}} + \bar{P}_{\text{pert}} \quad (4.3)$$

where

$$\bar{P}_{\text{unpert}} = \epsilon_0 \chi^{(1)} \bar{E}_\mu \quad (4.4)$$

Equation (4.2) thus becomes,

$$\nabla^2 E_\mu = \mu_0 \epsilon_0 \epsilon_r \frac{\partial^2 E_\mu}{\partial t^2} + \mu_0 \frac{\partial^2 P_{\text{pert},\mu}}{\partial t^2} \quad (4.5)$$

We take the eigenmodes of (4.1) as an orthonormal set in which to expand E and write

$$E_i = \frac{1}{2} \sum_{\mu=1}^{\mu=i} [A_\mu(z) e_{\mu} \exp(i(\omega t - \beta_{\mu z})) + c.c.] + \sum_{\rho=0}^{\rho=\infty} A_\rho(z) e_{\rho} \exp(i(\omega t - \beta_{\rho z})) d\rho \quad (4.6)$$

where μ extends over the discrete set of confined modes and includes both positive and negative traveling waves.

Substituting the modes in Eq. (4.6) into (4.5) provides the following relationship:

$$\begin{aligned} & \nabla^2 \left[\frac{1}{2} \sum_{\mu=1}^{\mu=i} [A_\mu(z) e_{\mu} \exp(i(\omega t - \beta_{\mu z})) + c.c.] + \sum_{\rho=0}^{\rho=\infty} A_\rho(z) e_{\rho} \exp(i(\omega t - \beta_{\rho z})) d\rho \right] \\ & - \mu_0 \epsilon_0 \epsilon_r \left[\frac{1}{2} \sum_{\mu=1}^{\mu=i} [A_\mu(z) e_{\mu} \exp(i(\omega t - \beta_{\mu z})) + c.c.] + \sum_{\rho=0}^{\rho=\infty} A_\rho(z) e_{\rho} \exp(i(\omega t - \beta_{\rho z})) d\rho \right] \\ & = \mu_0 \frac{\partial^2 P_{\text{pert},\mu}}{\partial t^2} \end{aligned} \quad (4.7)$$

The integration over ρ takes in the continuum of radiation modes, and *c.c.* denotes complex conjugation. Our chief interest lies in perturbations which couple only discrete modes so that, in what follows, we will neglect the two terms on the left side of (4.7). In weak coupling, further simplification is possible by applying the slowing varying envelope approximation (SVEA). This requires that the amplitude of the mode change slowly over a distance of the wavelength of the light as

$$\frac{\partial^2 A_\mu}{\partial z^2} \ll \beta_\mu \frac{\partial A_\mu}{\partial z} \quad (4.8)$$

so that

$$\nabla^2 E_t = \frac{1}{2} \sum_{\mu=1}^{\mu=l} \left[-2i\beta_{\mu} \frac{\partial A_{\mu}}{\partial z} e_{\mu} \exp(i(\omega t - \beta_{\mu} z)) - \beta_{\mu}^2 A_{\mu} e_{\mu} \exp(i(\omega t - \beta_{\mu} z)) + cc \right] \quad (4.9)$$

Expanding the second term in Eq. (4.7), noting that $\omega^2 \mu_0 \epsilon_0 \epsilon_r = \beta_{\mu}^2$, and combining with Eq. (4.9), the wave equation simplifies to

$$\sum_{\mu=1}^{\mu=l} \left[-i\beta_{\mu} \frac{\partial A_{\mu}}{\partial z} e_{\mu} \exp(i(\omega t - \beta_{\mu} z)) + cc \right] = \mu_0 \frac{\partial^2 P_{pert,t}}{\partial t^2} \quad (4.10)$$

Multiplying both sides of Eq. (4.10) by e_{μ}^* and integrating over the wave-guide cross-section leads to

$$\begin{aligned} & \sum_{\mu=1}^{\mu=l} \int_{-\infty}^{+\infty} \int_{-\infty}^{+\infty} \left[-i\beta_{\mu} \frac{\partial A_{\mu}}{\partial z} e_{\mu} e_{\mu}^* \exp(i(\omega t - \beta_{\mu} z)) + cc \right] dx dy \\ &= \int_{-\infty}^{+\infty} \int_{-\infty}^{+\infty} \mu_0 \frac{\partial^2 P_{pert,t}}{\partial t^2} e_{\mu}^* dx dy \end{aligned} \quad (4.11)$$

According to the orthogonality relationship

$$1/2 \int_{-\infty}^{+\infty} \int_{-\infty}^{+\infty} e_{\mu} e_{\nu}^* dx dy = \frac{2\omega\mu_0}{\beta_{\mu}} \delta_{\mu\nu} \quad (4.12)$$

Applying Eq. (4.12) directly results in

$$\begin{aligned} & \sum_{\mu=1}^{\mu=l} \left[-2i\omega\mu_0 \frac{\partial A_{\mu}}{\partial z} \exp(i(\omega t - \beta_{\mu} z)) + cc \right] \\ &= \int_{-\infty}^{+\infty} \int_{-\infty}^{+\infty} \mu_0 \frac{\partial^2 P_{pert,t}}{\partial t^2} e_{\mu}^* dx dy \end{aligned} \quad (4.13)$$

Equation (4.13) is fundamentally the wave propagation equation, which can be used to describe a variety of phenomena in the coupling of modes. Equation (4.13) applies to a set of forward- and back ward-propagating modes, it is now easy to see how mode coupling occurs by introducing forward- back ward-propagating modes. The

total transverse field may be described as a sum of both fields, not necessarily composed of the same mode order:

$$E_t = \frac{1}{2} [A_\nu e_\nu \exp(i(\omega t - \beta_\nu z)) + cc + B_\mu e_\mu \exp(i(\omega t + \beta_\mu z)) + cc] \quad (4.14)$$

$$H_t = \frac{1}{2} [A_\nu H_\nu \exp(i(\omega t - \beta_\nu z)) + cc - B_\mu H_\mu \exp(i(\omega t + \beta_\mu z)) - cc] \quad (4.15)$$

Here the negative sign in the exponent signifies the forward- and the positive sign the back ward-propagating mode, respectively. The modes of a waveguide form an orthogonal set, which in an ideal fiber will not couple unless there is a perturbation. Using Eqs. (4.14) and (4.15) in Eq. (4.13) leads to

$$\begin{aligned} & \left[\frac{\partial A_\nu}{\partial z} \exp(i(\omega t - \beta_\nu z)) + cc \right] - \left[\frac{\partial B_\mu}{\partial z} \exp(i(\omega t + \beta_\mu z)) + cc \right] \\ & = + \frac{i}{2\omega} \int_{-\infty}^{+\infty} \int_{-\infty}^{+\infty} \frac{\partial^2 P_{pert,t}}{\partial t^2} e_{\mu,\nu}^* dx dy \end{aligned} \quad (4.16)$$

Equation (4.16) is the main starting point for the following discussions.

4.1.2 Bragg Gratings in Multimode Fibers — Part I. Electromagnetic Derivations of the CMT formulation for Independent Mode MMFBG

In a multimode fiber, coupling can occur between identical or nonidentical modes depending on the transfer matrix

$$\begin{bmatrix} S_{11} & S_{12} & S_{13} \cdots & S_{1n} \\ S_{21} & S_{22} & S_{23} \cdots & S_{2n} \\ \cdots & & \cdots & \\ S_{n1} & S_{n2} & S_{n3} \cdots & S_{nn} \end{bmatrix}$$

According to the T-matrix characteristics, i.e., the coupling characteristics of modes interaction, we classify multimode fiber Bragg gratings (MMFBG) into two categories: independent mode and mode coupling, each leads to novel types of fiber devices and sensors.

The simplest type of multimode fiber grating is one whose refractive index perturbation is transversely uniform. For this case the mode coupling coefficient is diagonal and does not produce mode coupling, even to radiation modes, due to mode orthogonality. In the case of more general transverse spatial variation of the grating perturbation, we define independent mode gratings as those where the mode coupling coefficient is strongly diagonal. In this case, coupling only occurs between the same modes. Mode coupling gratings refer to all the coupling coefficients in T-matrix not equal to zero. That is to say, in addition to self-coupling happened in independent mode gratings, there also exist cross-coupling between different modes. This complicates the case and makes it hard to get the analytical solution.

In the following, we will give in detail the electromagnetic derivations of the coupled mode formulations for both categories of MMFBGs [12, 27, 31, 62-64].

We deal with independent mode gratings first. In FBGs, the dielectric constant varies periodically along the wave-propagation direction, the total polarization can be defined with the perturbed permittivity, $\Delta\epsilon(z)$ and the applied field as

$$P = \epsilon_0[\epsilon_r - 1 + \Delta\epsilon(z)]E_\mu \quad (4.17)$$

The term within the parentheses are equivalent to $\chi^{(1)}$, and ϵ_r is the relative permittivity of the unperturbed core. The constitutive relations between the permittivity of a material and the refractive index n result in the perturbation modulation index being derived from $n^2 = \epsilon_r$ so that

$$[n + \delta n(z)]^2 = \epsilon_r + \Delta\epsilon(z) \quad (4.18)$$

Assuming the perturbation to be a small fraction of the refractive index, it follows that

$$\Delta\epsilon(z) \approx 2n\delta n(z) \quad (4.19)$$

Defining the refractive index modulation of the grating as

$$\delta n(z) = \overline{\Delta n} \left\{ 1 + \sum_{N=1}^{\infty} \frac{V}{2} [\exp i[(2\pi N / \Lambda)z + \phi(z)] + cc] \right\} \quad (4.20)$$

where $\overline{\Delta n}$ is the refractive index change averaged over a single period of the grating, v is the visibility of the fringes, and the exponent term along with the complex conjugate cc describe the real periodic modulation in complex notation. An arbitrary spatially varying phase of $\phi(z)$ has been induced. Λ is the period of the perturbation, where N is an integer ($-\infty < N < +\infty$) that signifies its harmonic order. The period-averaged change in the refractive index has to be taken into account since it alters the effective index n_{eff} of a mode.

Combining Eqs. (4.18) and (4.20), the total material polarization is

$$P = \epsilon_0 \left\{ n^2 - 1 + 2n\overline{\Delta n} \left[1 + \sum_{N=1}^{\infty} \frac{v}{2} [\exp i[(2\pi N / \Lambda)z + \phi(z)] + cc] \right] \right\} E_{\mu} \quad (4.21)$$

where the first term on the RHS is the permittivity, the second term is the dc refractive index change, and the third term is the ac refractive index modulation. Finally, defining a new modulation amplitude by incorporating the visibility,

$$\delta n(z) = 2n \left[\overline{\Delta n} + \sum_{N=1}^{\infty} \frac{\Delta n}{2} [\exp i[(2\pi N / \Lambda)z + \phi(z)] + cc] \right] \quad (4.22)$$

The perturbed polarization can now be related to refractive index change shown in Eq. (4.22) to give

$$P_{pert} = 2n\epsilon_0 \left[\overline{\Delta n} + \sum_{N=1}^{\infty} \frac{\Delta n}{2} [\exp i[(2\pi N / \Lambda)z + \phi(z)] + cc] \right] E_{\mu} \quad (4.23)$$

Including Eq. (4.23) in Eq. (4.16) results in

$$\begin{aligned} & \left[\frac{\partial A_v}{\partial z} \exp(i(\omega t - \beta_v z)) + cc \right] - \left[\frac{\partial B_{\mu}}{\partial z} \exp(i(\omega t + \beta_{\mu} z)) + cc \right] \\ & = + \frac{i\epsilon_0}{2\omega} \int_{-\infty}^{+\infty} \int_{-\infty}^{+\infty} \frac{\partial^2}{\partial t^2} \delta n(z) [A_v \exp(i(\omega t - \beta_v z)) e_{\nu} + B_{\mu} \exp(i(\omega t + \beta_{\mu} z)) e_{\mu}] e_{\mu, \nu}^* dx dy + cc \\ & = -in\omega\epsilon_0 A_v \int_{-\infty}^{+\infty} \int_{-\infty}^{+\infty} \left[\overline{\Delta n} + \sum_{N=1}^{\infty} \frac{\Delta n}{2} [\exp i[(2\pi N / \Lambda)z + \phi(z)] + cc] \right] e_{\nu} \exp(i(\omega t - \beta_v z)) e_{\mu, \nu}^* dx dy \\ & \quad - in\omega\epsilon_0 B_{\mu} \int_{-\infty}^{+\infty} \int_{-\infty}^{+\infty} \left[\overline{\Delta n} + \sum_{N=1}^{\infty} \frac{\Delta n}{2} [\exp i[(2\pi N / \Lambda)z + \phi(z)] + cc] \right] e_{\mu} \exp(i(\omega t + \beta_{\mu} z)) e_{\mu, \nu}^* dx dy + cc \end{aligned} \quad (4.24)$$

Which can lead to the following simple coupled-mode equations by choosing the appropriate synchronous terms,

$$\frac{\partial A_\nu}{\partial z} = -i \sum \left\{ \sigma_{dc} A_\nu + \kappa_{ac}^* B_\mu \exp\{i[\Delta\beta z - \phi(z)]\} \right\} \quad (4.25)$$

$$\frac{\partial B_\mu}{\partial z} = i \sum \left\{ \sigma_{dc} B_\mu + \kappa_{ac} A_\nu \exp\{-i[\Delta\beta z - \phi(z)]\} \right\} \quad (4.26)$$

with

$$\Delta\beta = \beta_\mu + \beta_\nu - \frac{2\pi N}{\Lambda} \quad (4.27)$$

and the dc coupling constant,

$$\sigma_{dc} = n\omega\epsilon_0 \int_{-\infty}^{+\infty} \int_{-\infty}^{+\infty} \overline{\Delta n e_{\mu\nu}} e_{\mu\nu}^* dx dy \quad (4.28)$$

while the ac coupling constant includes the overlap integral,

$$\kappa_{ac} = n\omega\epsilon_0 \int_{-\infty}^{+\infty} \int_{-\infty}^{+\infty} \frac{\Delta n}{2} \xi_\nu \xi_\mu^* dx dy \quad (4.29)$$

Eqs. (4.25) and (4.26) are the coupled-mode equations from which the transfer characteristics of the Bragg grating can be calculated.

To find a solution, the following substitutions are made for the forward and backward propagating modes:

$$\begin{aligned} R &= A_\nu \exp\left(i\Delta\beta z - \frac{\phi}{2}\right) \\ S &= B_\mu \exp\left(-i\Delta\beta z + \frac{\phi}{2}\right) \end{aligned} \quad (4.30)$$

Differentiating Eq. (4.30) and substituting into Eqs. (4.25) and (4.26) results in the following coupled-mode equations:

$$\frac{dR}{dz} - i \left[\sigma_{dc} + \left(\Delta\beta - \frac{1}{2} \frac{d\phi(z)}{dz} \right) \right] R = +i\kappa_{ac} S \quad (4.31)$$

$$\frac{dS}{dz} + i \left[\sigma_{dc} + \left(\Delta\beta - \frac{1}{2} \frac{d\phi(z)}{dz} \right) \right] S = -i\kappa_{ac}^* R \quad (4.32)$$

We define $\hat{\sigma}$ is a general “dc” self-coupling coefficient as

$$\hat{\sigma} \equiv \Delta\beta + \sigma - \frac{1}{2} \frac{d\phi}{dt} \quad (4.33)$$

Then,

$$\frac{dR}{dz} = i\hat{\sigma}R(z) + i\kappa S(z) \quad (4.34)$$

$$\frac{dS}{dz} = -i\hat{\sigma}S(z) - i\kappa^* R(z) \quad (4.35)$$

For a single-mode Bragg reflection grating, we find the following simple relations:

$$\sigma \equiv \frac{2\pi}{\lambda} \overline{\delta n_{eff}} \quad (4.36)$$

$$\kappa = \kappa^* = \frac{\pi}{\lambda} \nu \overline{\delta n_{eff}} \quad (4.37)$$

If the grating is uniform along z , then $\overline{\delta n_{eff}}$ is a constant and $\frac{d\phi}{dz} = 0$, at phase matching, $\Delta\beta = 0$, and thus κ , σ , and $\hat{\sigma}$ are constants. Thus, (4.34) and (4.35) are coupled first-order ordinary differential equations with constant coefficients, for which closed-form solutions can be found when appropriate boundary conditions are specified. Assuming a forward-going wave incident from $z = -\infty$ and requiring that no backward-going wave exists for $z \geq L$, with $R(0) = 1$ and $S(L) = 0$ we obtain the solution to Eqs. (4.34) and (4.35) by Gaussian diagonal extinction method

$$R(z) = \exp(i\hat{\sigma}z) \{ \{-\sqrt{\kappa^2 - \hat{\sigma}^2} \cos[\sqrt{\kappa^2 - \hat{\sigma}^2}(L/2 - z)] + i\hat{\sigma} \sin[\sqrt{\kappa^2 - \hat{\sigma}^2}(L/2 - z)]\} / \{(\sqrt{\kappa^2 - \hat{\sigma}^2} \cos[(L/2)\sqrt{\kappa^2 - \hat{\sigma}^2}] + i\hat{\sigma} \sin[(L/2)\sqrt{\kappa^2 - \hat{\sigma}^2}]\} \} \quad (4.38)$$

$$S(z) = \exp(-i\hat{\sigma}z) \{-i\kappa \sin[\sqrt{\kappa^2 - \hat{\sigma}^2}(L/2 - z)] / \{(\sqrt{\kappa^2 - \hat{\sigma}^2} \cos[(L/2)\sqrt{\kappa^2 - \hat{\sigma}^2}] + i\hat{\sigma} \sin[\sqrt{\kappa^2 - \hat{\sigma}^2}(L/2)]\} \} \quad (4.39)$$

These result in the following analytical solution for the amplitude reflection coefficient:

$$\rho = \frac{S(0)}{R(0)} = \frac{-\kappa \sinh(SL)}{\Delta\beta \sinh(SL) - iS \cosh(SL)} \quad (4.40)$$

where

$$\Delta\beta = 2\pi(n_{eff} / \lambda - 1/2\Lambda) \quad (4.41)$$

and

$$S = \sqrt{|\kappa|^2 - \Delta\beta^2} \quad (4.42)$$

Finally, the power reflection coefficient is $|\rho|^2$,

$$r = |\rho|^2 = \frac{|\kappa|^2 \sinh^2(SL)}{\Delta\beta^2 \sinh^2(SL) + S^2 \cosh^2(SL)} \quad (4.43)$$

For independent mode gratings, for the case of a finite length periodic grating perturbation between $z = 0$ and $z = L$, the total grating reflectivity can be shown to be

$$R(L, \lambda) = \frac{\sum_{\sigma} |a_{\sigma\sigma}|^2 r_{\sigma}}{\sum_{\sigma} |a_{\sigma\sigma}|^2} \quad (4.44)$$

where $a_{\sigma\sigma}$ is the incident modal amplitude, r_{σ} is the modal reflectivity.

According to (4.44), The grating reflection response may be written as weighted sum of the individual reflection responses for each mode considered in isolation:

$$R(L, \lambda) = \sum_{\sigma} \eta_{\sigma} \frac{|\kappa_{\sigma,\sigma}|^2 \sinh^2(S_{\sigma}L)}{\Delta\beta_{\sigma}^2 \sinh^2(S_{\sigma}L) + S_{\sigma}^2 \cosh^2(S_{\sigma}L)} \quad (4.45)$$

where $\eta_{\sigma} = P_{\sigma} / \sum_{\mu} P_{\mu}$ is the fraction of total optical power in mode σ , $\kappa_{\sigma,\sigma}$ is self-coupling coefficient, $\Delta\beta_{\sigma}$ is the wavevector detuning and S_{σ} is the detuned coupling strength. They are defined from Eqs. (4.41) and (4.42).

Eqs. (4.44) and (4.45) are the power reflection response of independent mode MMFBGs. It is shown that the operation of a MMFBGs is affected by the mode population distribution (MPD).

4.1.3 Bragg Gratings in Multimode Fibers — Part II. Electromagnetic Derivations of the CMT formulations for Mode Coupling MMFBG

In Section 4.1.2, we derived the coupled-mode formulations for Bragg gratings for MMF in very detail. But it is only for a special coupled-wave phenomena — independent mode MMFBGs. In this Section, we will develop the coupled-mode formulations for MMFBGs in more generality. In this derivation, we do not define the perturbation P_{pert} to any fixed form but follow the similar derivation ideas as we have done in the last Section.

Fiber gratings introduce a longitudinal nonuniformity by the dielectric constant refractive index modulation periodically along the wave-propagation direction. This longitudinal nonuniformity, i.e., perturbation, can be expressed by the refractive index distribution deviating from the ideal waveguide situation slowly and weakly. Now we consider the following weakly-guided ideal waveguide and longitudinal nonuniformity waveguide:

A. ideal waveguide

The refractive index distribution is $n_0(u, v)$. The field distribution of waveguide mode $\psi_n(u, v)$ and the corresponding mode propagation constant β_n are known. They satisfy the wave equation

$$\nabla_t^2 \Psi_n + (k_0^2 n_0^2 - \beta_n^2) \Psi_n = 0 \quad (4.46)$$

at the same time, assuming ψ_n has been normalized as

$$\int_s \Psi_n \Psi_n^* ds = 1 \quad (4.47)$$

B. practical waveguide

The refractive index distribution of the practical waveguide is $n(u, v, z)$ and the mode field distribution is $\psi(u, v, z)$. They also satisfy

$$\nabla^2 \Psi + k_0^2 n^2 \Psi = 0 \quad (4.48)$$

We note that there is only very small difference between $n(u, v, z)$ and $n_0(u, v)$.

Compared with the variation frequency of electromagnetic field, $n(u, v, z)$ and $\psi(u, v, z)$ are just the slowly varying function depending on z .

According to the completeness property of waveguide modes, ψ can be expressed by ψ_n

$$\Psi(u, v, z) = \sum_{n,p} a_n^p(z) \Psi_n^p(u, v) \exp(-jp\beta_n z), \quad m \neq n, \quad p = +, - \quad (4.49)$$

where, $a_n^p(z)$ is a slowly varying function of variable z . Ignoring coupling to the radiation modes which are not our chief interest, substituting Eq. (4.49) into wave equation (4.48) provides the following relationship:

$$\sum_{n,p} \left[a_n^p \nabla_n^2 + \frac{d^2 a_n^p}{dz^2} - j2p\beta_n \frac{da_n^p}{dz} - \beta_n^2 a_n^p + k_0^2 n^2 a_n^p \right] \Psi_n^p \exp(-jp\beta_n z) = 0 \quad (4.50)$$

Because $a_n^p(z)$ is a slowly varying function of z , i.e., the amplitude of the mode change slowly over a distance of the wavelength of the light, so that

$$\left| \frac{d^2 a_n^p}{dz^2} \right| \ll \left| 2\beta_n \frac{da_n^p}{dz} \right| \quad (4.51)$$

Applying this slowly varying envelope approximation (SVEA), we neglect the second-order derivation of $a_n^p(z)$ in the Eq. (4.50). From Eq. (4.46) we get

$$\sum_{n,p} \left[-j2p\beta_n \frac{da_n^p}{dz} + k_0^2 (n^2 - n_0^2) a_n^p \right] \Psi_n^p \exp(-jp\beta_n z) = 0 \quad (4.52)$$

Multiplying both sides of Eq. (4.52) by $\psi_m^{q*} \exp(jq\beta_m z)$ and integrating over the waveguide cross-section, simultaneously considering the modes orthogonality relationship results in

$$\frac{da_m^q}{dz} = \sum_{n,p} K_{mn}^{pq} a_n^p \exp[j(q\beta_m - p\beta_n)z] \quad (4.53)$$

where

$$K_{mn}^{pq} = \frac{k_0^2}{j2q\beta_m} \int_S (n^2 - n_0^2) \Psi_n^p \Psi_m^{q*} ds \quad (4.54)$$

is the amplitude coupling coefficient between modes (m, q) and (n, p) .

Eq. (4.53) is a set of cross-coupled differential equations. To find a solution to Eq. (4.53) requires some necessary simplifications according to the specific problem.

The difference between longitudinal nonuniformity optical waveguide and longitudinal uniform optical waveguide is immediately apparent according to Eq. (4.53). The longitudinal nonuniformity of an optical waveguide causes complicated coupling interaction between all guided modes. When modes travel in waveguide, there happen significant interchange of energy among the modes. In fact, Eq. (4.53) is the general coupled mode equations for longitudinal nonuniformity optical waveguide. It is the important and theoretical foundation for analyzing and designing various optical waveguide.

In the ideal-mode approximation to coupled-mode theory, we assume that the transverse component of the electric field can be written as a superposition of the ideal modes labeled j (i.e., the modes in an ideal waveguide with no grating perturbation), such that

$$\vec{E}_t(x, y, z, t) = \sum_j [A_j(z) \exp(i\beta_j z) + B_j(z) \exp(-i\beta_j z)] \cdot \vec{e}_{jt}(x, y) \exp(-i\omega t) \quad (4.55)$$

where $A_j(z)$ and $B_j(z)$ are slowly varying amplitudes of the j th modes traveling in the $+z$ and $-z$ direction, respectively. The transverse mode field is $\vec{e}_{jt}(x, y)$. While the modes are orthogonal in an ideal waveguide and hence, do not exchange energy, the presence of a dielectric perturbation causes the modes to be coupled such that the amplitudes A_j and B_j of the j th mode evolve along the z axis. According to Eq. (4.53), evolution of A_j and B_j can be expressed by

$$\begin{aligned} \frac{dA_j}{dz} = & i \sum_k A_k (K_{kj}^t + K_{kj}^z) \exp[i(\beta_k - \beta_j)z] \\ & + i \sum_k B_k (K_{kj}^t - K_{kj}^z) \exp[-i(\beta_k + \beta_j)z] \end{aligned} \quad (4.56)$$

$$\begin{aligned} \frac{dB_j}{dz} = & -i \sum_k A_k (K_{kj}^t - K_{kj}^z) \exp[i(\beta_k + \beta_j)z] \\ & - i \sum_k B_k (K_{kj}^t + K_{kj}^z) \exp[-i(\beta_k - \beta_j)z] \end{aligned} \quad (4.57)$$

In (4.56) and (4.57), $K_{kj}^t(z)$ is the transverse coupling coefficient between modes j and k given by directly from Eq. (4.54) as

$$K_{kj}^t(z) = \frac{\omega}{4} \iint_{\infty} dx dy \Delta \varepsilon(x, y, z) \bar{e}_{kt}(x, y) \cdot e_{jt}^*(x, y) \quad (4.58)$$

where $\Delta \varepsilon$ is the perturbation to the permittivity, approximately $\Delta \varepsilon \cong 2n \delta n$ when $\delta n \ll n$. The longitudinal coefficient $K_{kj}^z(z)$ is analogous to $K_{kj}^t(z)$, but generally $K_{kj}^z(z) \ll K_{kj}^t(z)$ for fiber modes, and thus this coefficient is usually neglected. $K_{kj}^t(z)$ is called cross-coupling coefficient. Let $k = j$, we can directly get the self-coupling coefficient.

The electric fields present in Eq. (4.58) are e_{kt} for LP_k mode and e_{jt} for LP_j mode, respectively. They all should be situated in *field normalizations* such that the power flows are normalized to unity, i.e., it follows that

$$P = \frac{1}{2} \iint_s \text{Re}(\bar{e} \times \bar{h}^*) \cdot d\bar{S} = \frac{n}{2\eta_0} \iint_s |e_t|^2 dS \quad (4.59)$$

$$\text{where } \eta_0 = \left(\frac{\varepsilon_0}{\mu_0} \right)^{-1/2}$$

P is the time-average power carried by the transverse field components along z -axis (i.e., direction of propagation).

In theory, Bragg grating is characterized by complex Fourier expansion of the periodic structure of the perturbation. In the most general case, the index perturbation $\delta n(z)$ is modeled as a phase and amplitude-modulated periodic waveform

$$\delta n(z) = \delta n_0(z) \left\{ 1 + m \cos \left[\frac{2\pi z}{\Lambda} + \phi(z) \right] \right\} \quad (4.60)$$

where m is the fringe visibility of the index change, Λ is the normalized period, and the function $\phi(z)$, assumed to be slowly varying on a length scale set by the normalized period, can describe a position-dependent chirp. The other slowly varying function $\delta n_0(z)$ characterizes the space averaged background refractive index increase due to the envelope of the induced index change (DC background envelope).

It should be mentioned that higher Fourier components (i.e., multiples of $2\pi/\Lambda$) are neglected in Eq. (4.60). They can have two physically distinct effects: First, they will lead to scattering associated with multiples of $2\pi/\Lambda$; this can be described simply by the addition of more terms to Eq. (4.60) but will not be important at the wavelengths of interest in this paper. Second, they will modify the scattering associated with the fundamental wave number $2\pi/\Lambda$; these effects can be included in the coupled-mode equations that we derive here but at grating strengths of current interest they will be small. Thus it is sufficient to restrict ourselves to Eq. (4.60).

If we define two new coefficients

$$\sigma_{kj}(z) = \frac{\omega n_{co}}{2} \overline{\delta n_{co}}(z) \iint dx dy \vec{e}_{kx}(x, y) \cdot \vec{e}_{jx}(k, y) \quad (4.61)$$

$$\kappa_{kj}(z) = \frac{\nu}{2} \sigma_{kj}(z) \quad (4.62)$$

where σ is a “dc”(period-averaged) coupling coefficient and κ is an “AC” coupling coefficient, then the general coupling coefficient can be written

$$K'_{kj}(z) = \sigma_{kj}(z) + 2\kappa_{kj(z)} \cos \left[\frac{2\pi}{\Lambda} z + \Phi(z) \right] \quad (4.63)$$

From the characterization of Eq. (4.60), it is apparent by now that in the above equation σ , κ , ϕ are all slowly varying functions of z .

Equations (4.56) – (4.63) form the basis for the solution of a number of coupled mode problems. They are exactly the coupled-mode equations for MMFBGs in sufficient generality that we use to describe the multimode FBG structures. They show that the change in the amplitude of each mode as a function of the deformation $\Delta\epsilon$, the modal field distribution, and of the amplitudes of all other modes present in

the guide. Depending on the particular problem at hand, one can usually make some simplifying assumptions at this stage.

The coupled-mode Eqs. (4.56) and (4.57) can hardly be found an analytical solution. They need to be evaluated numerically using some standard techniques. About the related numerical method, we will discuss in the following Section 4.2. Assuming the numerical solutions to MMFBGs coupled mode equations have been known at this moment, the total grating reflection may be described as a linear superposition of individual amplitude square for all the modes. This is because all the guided modes supported in the multimode fiber interact with each other (cross-coupling) and/or among themselves (self-coupling) only in the region of Bragg grating. Beyond the grating area, these modes are still orthonormal as they travel in the waveguide without gratings or any other perturbations. Therefore, the grating reflection response can be written as

$$R(L, \lambda) = \frac{S(L, \lambda)}{P_{in}(L, \lambda)} \quad (4.64)$$

where

$$P_{in} = \sum_{\sigma} |A_{\sigma}(0)|^2$$

$$S(L, \lambda) = \sum_{\sigma} |B_{\sigma}(0)|^2$$

Under standard normalization condition

$$P_{in} = \sum_{\sigma} |A_{\sigma}(0)|^2 = 1 \quad (4.65)$$

Finally, the total reflectivity of MMFBG is

$$R(L, \lambda) = \sum_{\sigma} |B_{\sigma}(0)|^2 \quad (4.66)$$

A_{σ}, B_{σ} are incident and reflected modal amplitude respectively. Recall the Eq. (4.45), the fraction of total optical power in mode σ has been taken into account for the independent mode MMFBG reflection response. But here, for such mode coupling gratings, the modal power distribution was not encompassed in MMFBG reflectivity formula directly due to it has been treated as the boundary conditions while calculating the numerical solution to coupled mode equations (4.56) and (4.57).

The physical model for MMFBGs represented by Eqs. (4.56) to (4.63) forms the basis for the rest of this thesis. In the subsequent section, we will describe numerical calculations for simulating fiber Bragg gratings.

4.2 Applied Numerical Computation Methods for MMFBGs

In last section we derived the coupled mode equations for MMFBGs. These equations must be solved numerically through the fiber profile.

First, we transform the governing coupled mode equations in a way that is suitable for numerical analysis and implementation.

Then our goal is to solve the coupling equations which is actually the ordinary differential equations by adopting boundary conditions for our system.

Now let's review the coupled mode equations purely from the mathematical point of view

$$\frac{df_1}{dx} = F_A(f_1, f_2, x) \quad (4.67)$$

$$\frac{df_2}{dx} = F_B(f_1, f_2, x) \quad (4.68)$$

The known boundary condition is $f_1(x_0)$ and $f_2(x_L)$, with the range from x_0 to x_L . The problem of interest here is $f_2(x_0)$ and $f_1(x_L)$. As may be apparent by now, we are facing both *initial value problems* (IVP) and *boundary value problems* (BVP) for ordinary differential equations describing our physical system. In general, boundary value problems always require considerably more effort to solve than do initial value problems.

In this thesis, we will use Runge-Kutta method and shooting method to solve IVPs and BVPs respectively. The reason for applying these methods lies in two aspects: First, Runge-Kutta method very effective and relatively easy to program. Secondly, although shooting method might be less efficient than other methods (relaxation methods), we still prefer to follow the experienced advice: we always

shoot first, and only then relax. The following subsections will introduce these methods principally [65-68, 55].

4.2.1 Runge-Kutta Method for Solving Initial Value Problems

Runge-Kutta methods are single-step methods that replace higher derivatives by finite difference approximations based on values of f at points between t_k and t_{k+1} . It can be derived by applying numerical quadrature rules to evaluate the integral

$$y_{k+1} - y_k = \int_{t_k}^{t_{k+1}} f(t, y(t)) dt \quad (4.69)$$

The second derivative of y is given by

$$y'' = f_t + f_t f \quad (4.70)$$

where each function is evaluated at (t, y) . We can approximate the term on the right by expanding f in a Taylor series in two variables

$$f(t+h, y+hf) = f + hf_t + hf_y f + O(h^2) \quad (4.71)$$

from which we obtain

$$f_t + f_t f = \frac{f(t+h, y+hf) - f(t, y)}{h} + O(h) \quad (4.72)$$

With this approximation to the second derivative, the 2nd-order Taylor series becomes

$$\begin{aligned} y_{k+1} &= y_k + h_k f(t_k, y_k) + \frac{h_k^2}{2} \frac{f(t_k + h_k, y_k + h_k f(t_k, y_k)) - f(t_k, y_k)}{h} \\ &= y_k + \frac{h_k}{2} (f(t_k, y_k) + f(t_k + h_k, y_k + h_k f(t_k, y_k))) \end{aligned} \quad (4.73)$$

which is known as Heun's method and can be implemented in the form

$$y_{k+1} = y_k + \frac{h_k}{2} (k_1 + k_2) \quad (4.74)$$

where $k_1 = f(t_k, y_k)$ and $k_2 = f(t_k + h_k, y_k + h_k k_1)$.

The best-known Runge-Kutta method is the classical fourth-order scheme

$$y_{k+1} = y_k + \frac{h_k}{6} (k_1 + 2k_2 + 2k_3 + k_4) \quad (4.75)$$

where

$$k_1 = f(t_k, y_k) \quad (4.76)$$

$$k_2 = f(t_k + h_k/2, y_k + h_k k_1/2) \quad (4.77)$$

$$k_3 = f(t_k + h_k, y_k + h_k k_2/2) \quad (4.78)$$

$$k_4 = f(t_k + h_k, y_k + h_k k_3) \quad (4.79)$$

Runge-Kutta methods have a number of virtues. To proceed to time t_{k+1} , they require no history of the solution prior to time t_k , which makes them self-starting at the beginning of the integration, and also makes it easy to change the step size during the integration. These features also make Runge-Kutta methods relatively easy to program, which accounts in part for their popularity.

4.2.2 Shooting Method for Solving Boundary Value Problems

By itself, a differential equation does not uniquely determine a solution; additional side conditions must be imposed on the solution to make it unique. In this section, we discuss “pure” shooting, where the integration proceeds from x_1 to x_2 , and we try to match boundary conditions at the end of the integration.

The “standard” two point boundary value problem has the following form: We desire the solution to a set of N coupled first-order ordinary differential equations, satisfying n_1 boundary conditions at the starting point x_1 , and a remaining set of $n_2 = N - n_1$ boundary conditions at the final point x_2 .

The differential equations are

$$\frac{dy_i(x)}{dx} = g_i(x, y_1, y_2, \dots, y_n) \quad i = 1, 2, \dots, N \quad (4.80)$$

At x_1 , the solution is supposed to satisfy

$$B_{1j}(x, y_1, y_2, \dots, y_n) = 0 \quad j = 1, \dots, n_1 \quad (4.81)$$

while at x_2 , it is supposed to satisfy

$$B_{2k}(x, y_1, y_2, \dots, y_n) = 0 \quad k = 1, \dots, n_2 \quad (4.82)$$

Imagine that these freely specifiable values are the components of a vector \mathbf{V} that

lives in a vector space of dimension n_2 . Then, knowing the functional form of the boundary conditions (4.81), we can write a function that generates a complete set of N starting values y , satisfying the boundary conditions at x_1 , from an arbitrary vector value of V in which there are no restrictions on the n_2 component values. In other words (4.81) converts to a prescription

$$y_i(x) = y_i(x_1; V_1, V_2, \dots, V_{n_2}) \quad i = 1, \dots, N \quad (4.83)$$

Given a particular V , a particular $y(x_1)$ is thus generated. It can then be turned into a $y(x_2)$ by integrating the ODEs to x_2 as an initial value problem. Now, at x_2 , let us define a *discrepancy vector* F , also of dimension n_2 , whose components measure how far we are from satisfying the n_2 boundary conditions at x_2 (4.82). Simplest of all is just to use the right-hand sides of (4.82),

$$F_k = B_{2k}(x_2, y) \quad k = 1, \dots, n_2 \quad (4.84)$$

Now, we want to find a vector value of V that zeros the vector value of F .

The basic idea is illustrated in Fig. 4-3. Each curve represents a solution of the same ODE, with different values for the initial slope giving different solutions for the

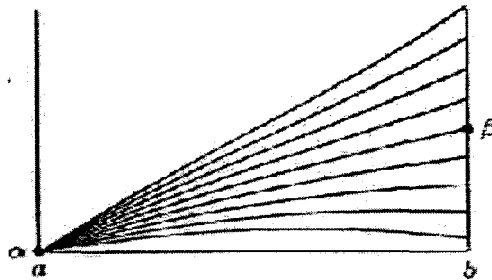


Fig. 4-3 Shooting method for two-point boundary value problem [67].

ODE. All of the solutions start with the given initial value, but for only one value of the initial slope does the resulting solution curve hit the desired boundary condition. We keep adjusting our aim until we hit the target. We do this by invoking the Newton-Raphson's method, which is to be described in the next section.

4.2.3 Newton-Raphson Method for constructing shooting Algorithm

Newton's method (also called the Newton-Raphson method) is by far the most popular method for solving an equation of the form $f(x) = 0$. Our implementation of the shooting method exactly implements Newton-Raphson. This method offers a very efficient means of converging to a root. Let us see how it works:

A typical problem gives N functional relations to be zeroed, involving variables x_i , $i = 1, 2, \dots, N$:

$$F_i(x_1, x_2, \dots, x_N) = 0 \quad i = 1, 2, \dots, N \quad (4.85)$$

We let \mathbf{x} denote the entire vector of values x_i and \mathbf{F} denote the entire vector of functions F_i . In the neighborhood of \mathbf{x} , each of the functions F_i can be expanded in Taylor series

$$F_i(\bar{x} + \delta\bar{x}) = F_i(\bar{x}) + \sum_{j=1}^N \frac{\partial F_i}{\partial x_j} \delta x_j + O(\delta\bar{x}^2) \quad (4.86)$$

The matrix of partial derivatives appearing in Eq. (4.86) is the *Jacobian* matrix \mathbf{J} :

$$J_{ij} \equiv \frac{\partial F_i}{\partial x_j} \quad (4.87)$$

It is not feasible to compute these partial derivative analytically. Rather, each requires a separate integration of the N ODEs, followed by the evaluation of

$$\frac{\partial F_i}{\partial V_j} \approx \frac{F_i(V_1, \dots, V_j + \Delta V_j, \dots) - F_i(V_1, \dots, V_j, \dots)}{\Delta V_j} \quad (4.88)$$

In matrix notation equation (4.86) is

$$\bar{F}(\bar{x} + \delta\bar{x}) = \bar{F}(\bar{x}) + \bar{J} \cdot \delta\bar{x} + O(\delta\bar{x}^2) \quad (4.89)$$

By neglecting terms of order $\delta\bar{x}^2$ and higher and by setting $\bar{F}(\bar{x} + \delta\bar{x}) = 0$, we obtain a set of linear equations for the corrections $\delta\bar{x}$ that move each function closer to zero simultaneously, namely

$$\bar{J} \cdot \delta\bar{x} = -\bar{F}, \quad (4.90)$$

Matrix equation (4.90) can be solved by *LU* decomposition, i.e., lower and upper triangular decomposition. The correction are then added to the solution vector

$$\bar{x}_{new} = \bar{x}_{old} + \delta\bar{x} \quad (4.91)$$

and the process is iterated to convergence. In our program, it is done automatically to check the degree to which both functions and variables have converged. Once either reaches targeted accuracy, that is, the value is less than some tolerance we set, the iteration stops.

Therefore, we see that using Runge-Kutta method, the MMFBGs coupled mode equations (4.56) and (4.57) can be solved numerically and a set of unique solutions can be achieved with shooting-method decided boundary (BCs). To sum up, the algorithm goes as the following:

- (i) Use Runge-kutta method to solve IVPs for our governing ODEs from a physically reasonable initial guess.
- (ii) Determine the optical fiber structure and grating structure, for example, step-index fiber, graded-index fiber, etc., define certain parameters for the fiber and make clear refractive index distribution.
- (iii) Determine the electric field profiles of fiber $\Psi_j(x, y)$ and calculate light propagation.
- (iv) Compute the coupling coefficients, to calculate the K_{kj} , the fiber modes in step (iii) are needed; also, explore the phase matching condition.
- (v) Determine boundary conditions or launch conditions, again fiber modes are needed and we may assume some reasonable value, for instance, assume that the field $S(L) = 0$, which is satisfied by the fact that the reflection field at the output end of the grating can not exist owing to the absence of the perturbation beyond that region.
- (vi) Apply Newton-Raphson to implement a complete cycle of the shooting method that thus will take us right to the solution ultimately.

4.3 Solution of the coupled Mode Equations for MMFBGs

To clarify the above relations, we present the numerical algorithm by means of a block diagram, which is shown in Fig. 4-4.

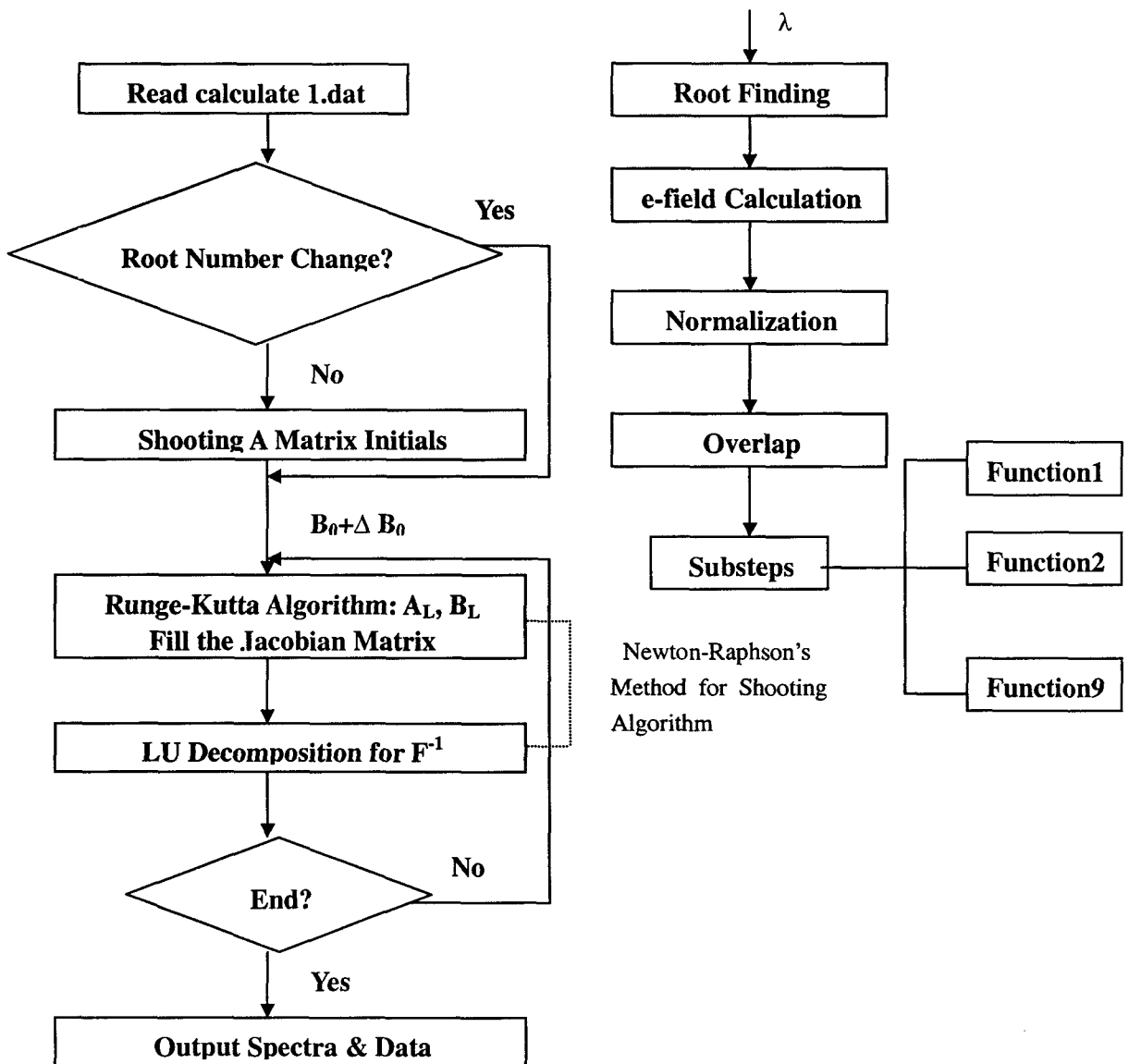


Fig. 4-4 Block diagram of the numerical algorithm for theoretical simulations

We apply this numerical procedure to calculate the reflection and transmission response of fiber gratings subject to equally distributed mode power inputs. We set the fiber and grating characteristics as follows: $n_1 = 1.46$, $n_2 = 1.4348$, $a = 4\mu\text{m}$, $\Lambda = 0.533\mu\text{m}$, $\Delta n = 0.001$, $L = 10000\mu\text{m}$ (ideally designed parameters to test and verify the MMFBG theoretical feasibility).

The solution to the reflection spectrum $R=|r^2|$, and its corresponding transmission spectrum are shown in Fig. 4-5.

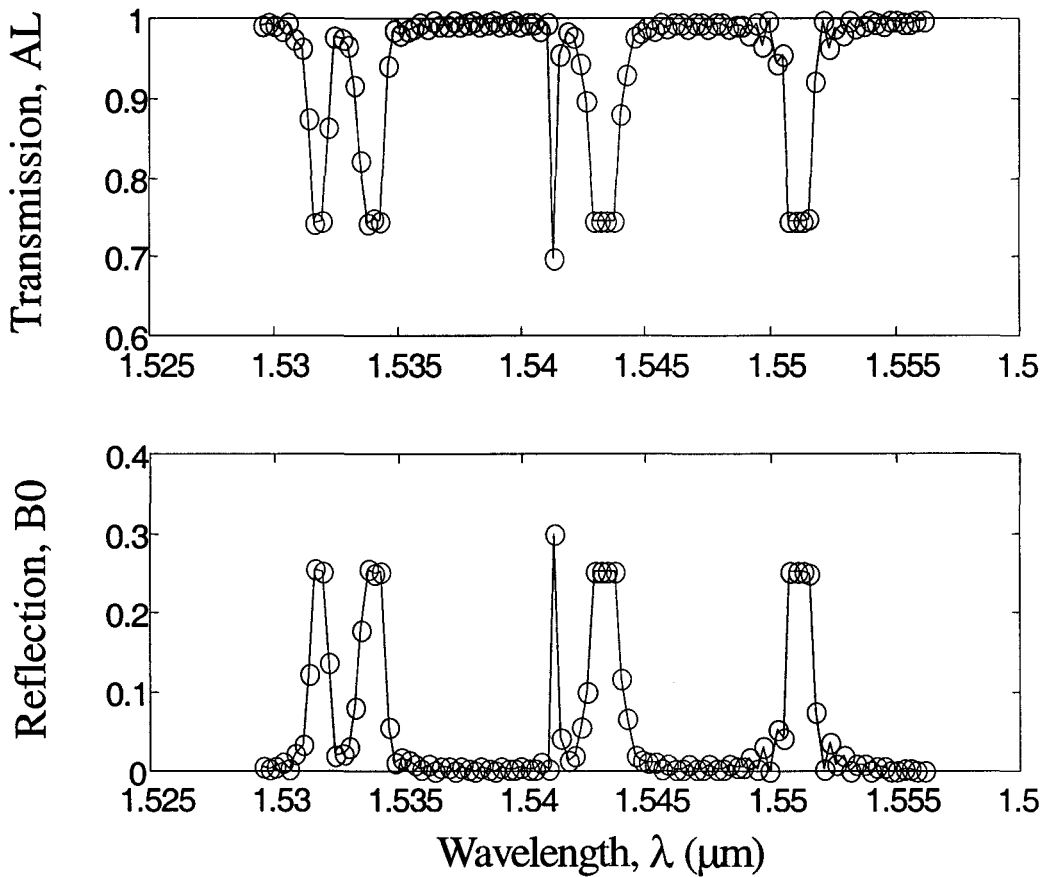


Fig. 4-5 Solutions to four modes FBG CMEs: Reflection and Transmission spectra

There are four modes guiding in the following fiber which we are working with. Five peaks are observed and four of them, the peak regions are flattened and the spectrum broadens. One more interesting phenomenon is a remarkable sharp spectral

resonance standing almost in the middle of the spectrum and even higher than all other reflection peaks. In our simulation, this strongly reflecting grating with a large index change becomes saturated because the incident wave is completely reflected before reaching the end of the gratings, and thus the bandwidth is independent of length and directly proportional to the induced index change. The notable sharp reflected signal is due to the contributions of cross-coupling interaction. Quantitatively, this behavior of the spectral characteristics of here considered Bragg grating can be confidently confirmed and nicely explained by a serial separate mode analysis pictures developed by setting excitation conditions as:

Table 4-1 Excitation conditions for separate mode analysis

Mode	Excited Power Conditions			
	Sequence 1	Sequence 2	Sequence 3	Sequence 4
1	1	0	0	0
2	0	1	0	0
3	0	0	1	0
4	0	0	0	1

These situations are simulated and the results are presented in plots Fig. 4-6 (a)-(d), respectively. In this illustration, we can see very clearly that LP_m mode only can couple with the mode with the same order m , modes of different order m are orthogonal. For here four modes, i.e., LP_{01} , LP_{02} , LP_{11} , LP_{21} , the former two spectra both have two peaks (one is self-coupling and one is cross-coupling) whilst the latter two spectra only possess one peak (only self-coupling). The saturated peaks are resulted from self-coupled modes and the sharpened one consists of two components which appear twice in Figs. (a) and (b) separately.

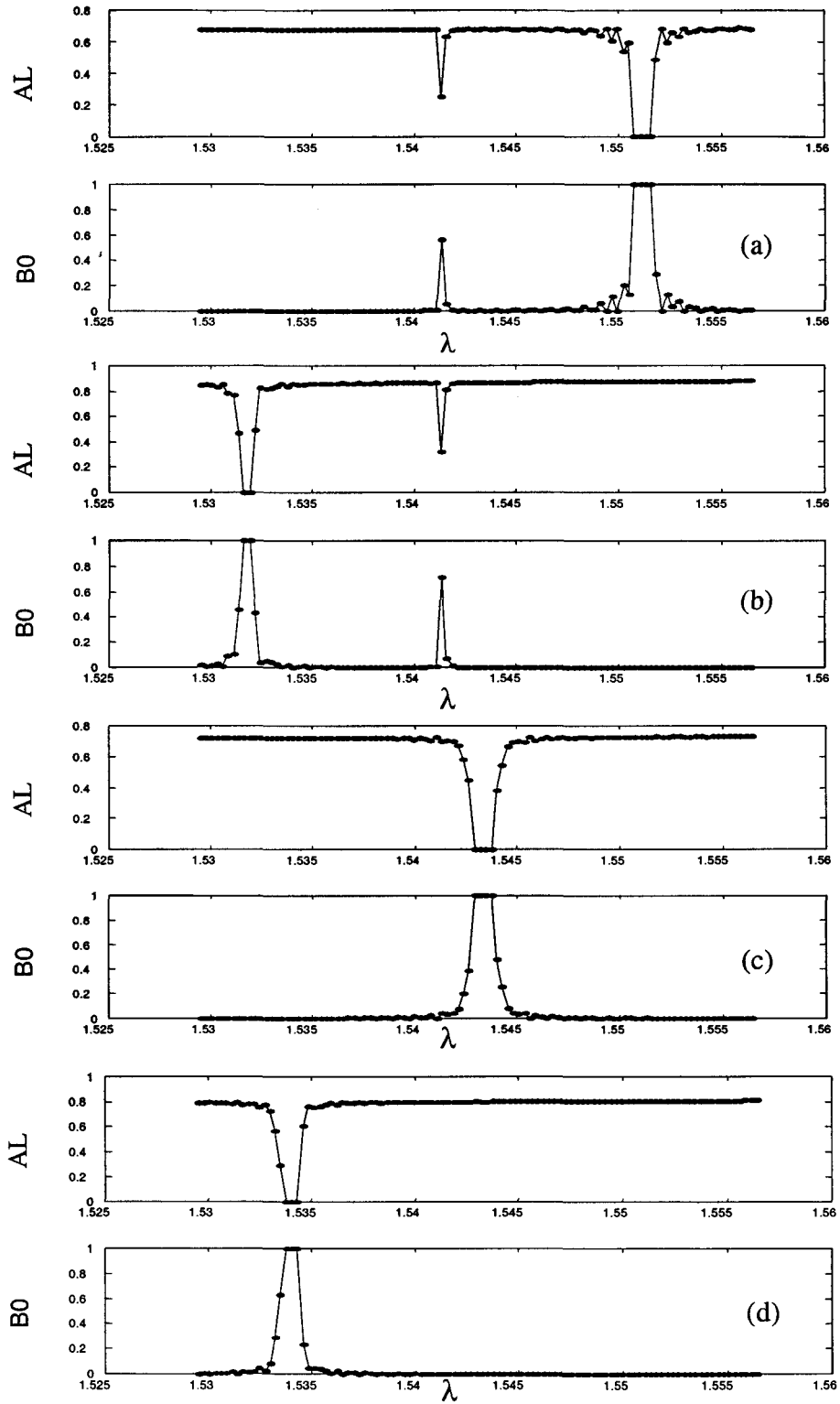


Fig. 4-6 Spectral response of the Bragg grating: (a)-(d) for decomposition analysis full spectra in Fig 4-5, respectively.

Another example is concerned about a more complicated Bragg grating for fifty-seven modes fiber structure. The parameters setting for the fiber and the grating are as in the followings: $n_1 = 1.462$, $n_2 = 1.4483$, $a = 25\mu\text{m}$, $\Lambda = 0.534\mu\text{m}$, $\Delta n = 0.00018517$, $L = 10000\mu\text{m}$. Fig. 4-7 shows the multiple peaks spectral response for a typical transmission and reflection characteristics of a MMFBG. Both these two example simulations evidently illustrate the theoretical feasibility of a multimode fiber Bragg grating.

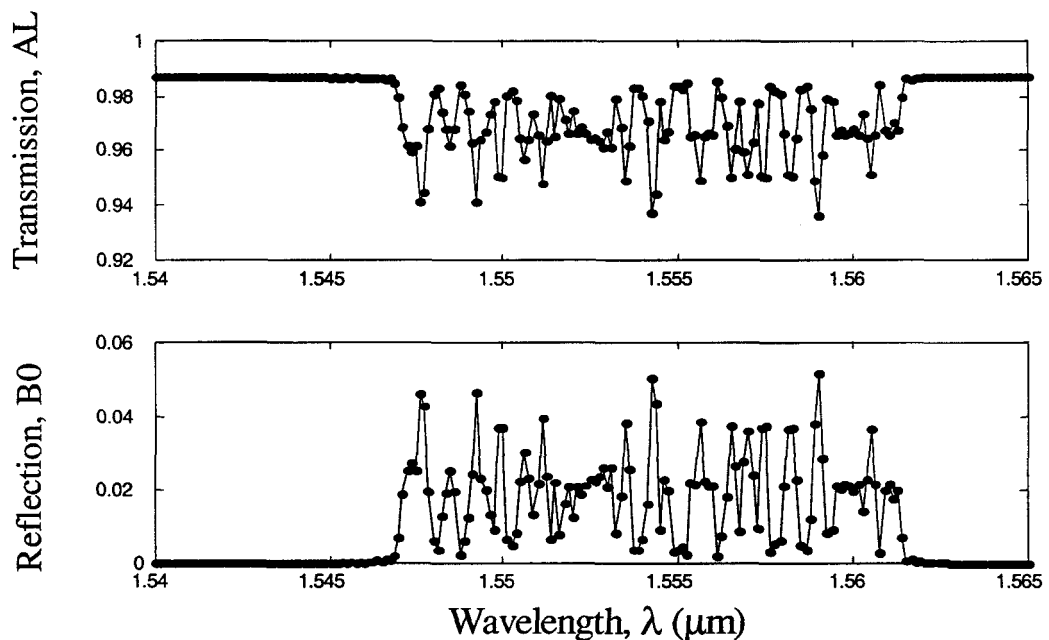


Fig. 4-7 Solutions to fifty-seven modes FBG CMEs: Reflection and Transmission Spectra.

It should be noted that there are step-size $\Delta\lambda$ and Δz used as free parameters. $\Delta\lambda$ describing the wavelength stepsize will strongly affect the spectral properties including peak numbers, peak intensity, peak shape, and so on. $\Delta\lambda$ should be small enough to get true spectra. Otherwise it will conceal some real information of the spectra. Then a question is: how small $\Delta\lambda$ is enough? The answer is: as small as possible, or, the smaller the better; but it takes the price of time consumption. I have a perfect answer which is: choose the exact same $\Delta\lambda$ in our software as the $\Delta\lambda$ in actual experiments (optical spectral analyzer). Under such a selection criteria, the spectra

from our numerical simulator will absolutely as “accurate” as the spectra from experiments.

On the other hand, Δz mostly decides the Newton-Raphson’s shooting convergence property and the calculation speed as well as its precision. Since the algorithm is a combination of the numerically stable and efficient Newton-Raphson method with shooting reconstruction, the calculation is not very sensitive to the precise, small choice for Δz . Finally, depending on a particular problem, it is possible to get a well balance between the simulation accuracy and computation efficiency.

4.4 Model Validation and Physical Interpretation

To validate our model, we are going to apply it to the spectral response of the reflectivity of FBGs that can be compared with analytical proof. We only work with the reflected signal, although the study can be extended to the transmitted one. We start with the simplest signal-mode fiber grating, then proceed to next typical two-mode coupled-mode FBG. The reason for picking these two kinds of FBGs is that distinguishing spectral features have been well known in numerous references. Typical sets of FBG parameters are selected. For example, $n_1 = 1.46$, $n_2 = 1.45854$, $a = 5\mu\text{m}$, $\Lambda = 0.530128\mu\text{m}$, $\Delta n = 0.00018517$, $L = 10000\mu\text{m}$, for single mode FBG simulation; the following is for two-mode FBGs spectral simulation: $n_1 = 1.46$, $n_2 = 1.45854$, $a = 12\mu\text{m}$, $\Lambda = 0.530128\mu\text{m}$, $\Delta n = 0.00018517$, and $L = 10000\mu\text{m}$.

The numerically calculated reflection spectra through such a single-mode and a two-mode fiber Bragg grating are given in Figs. 4-8 (a) and 4-9 (a). The analytical results are compared with them in Figs. 4-8 (b) and 4-9 (b) accordingly. As can be seen, the numerical calculations are identical to their corresponding analytical reflection by all means.

To further verify our method for more than two modes FBG, we performed our simulations using the same set of parameters as the first example in the last section, except for index variation $\Delta n = 0.00018517$. A uniform grating is considered here.

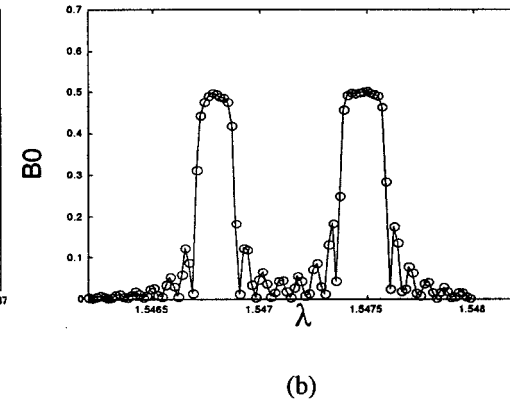
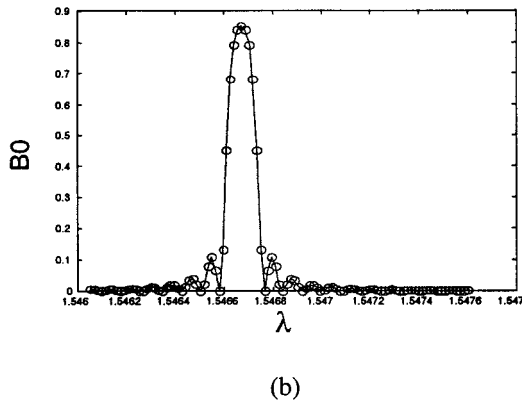
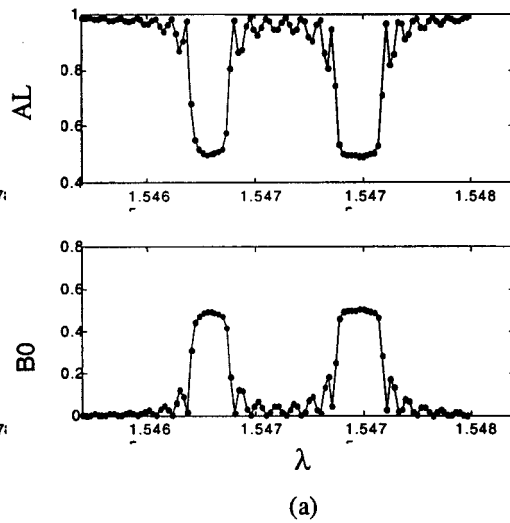
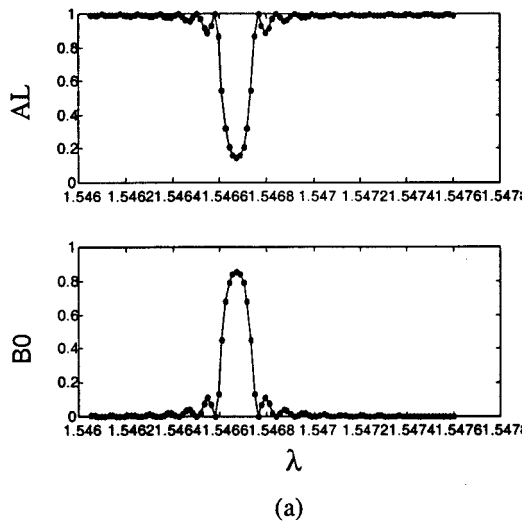


Fig.4-8 Comparison of a typical reflection spectrum of a single mode fiber Bragg grating (SMFBG) (a) numerical spectrum, and (b) analytical spectrum.

Fig.4-9 Comparison of a typical reflection spectrum of a two-mode FBG: (a) numerical simulation of the FBG, and (b) analytical solution of the FBG.

The cross coupling between modes of the same m is weak for this four mode MMF structure with the explicit Δn value. Our simulation result for the FBG spectrum is shown in Fig. 4-10, where no reflected peak accounted for cross coupling is observed. For a uniform grating, negligible cross coupling, an analytical solution for the reflectivity or transmission is available. Fig. 4-11 was yielded in such cases, which amount to approximating the total grating reflection response as the weighted sum of the individual reflection responses for each mode considered in isolation. In other

words, this is a mode coupling system assuming only self-coupling involved. Clearly, the reflection response simulations from our developed numerical approach and from the standard analytical solution are identical to each other for weak cross coupling MMFBG situations.

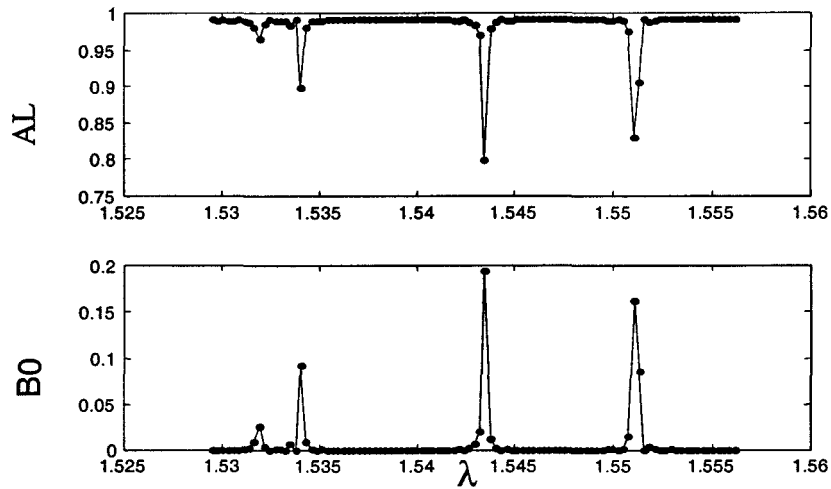


Fig. 4-10 The numerically calculated reflection response of the four-mode MMFBG with weak cross coupling.

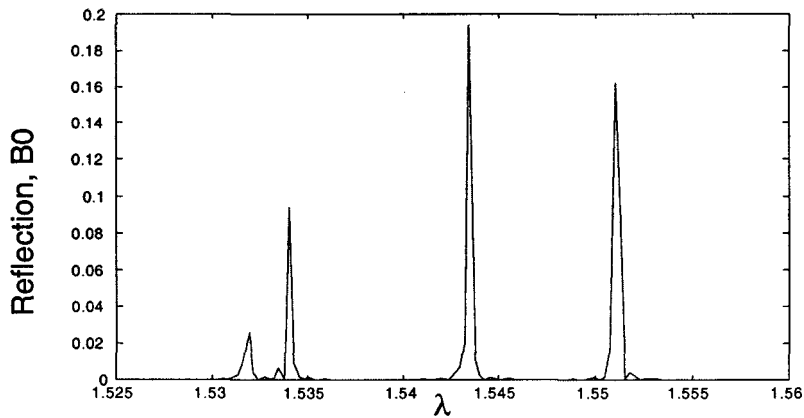


Fig. 4-11 Analytical solution of the four-mode MMFBG with only self coupling MMFBG

In the above manners, we can validate our model and algorithm for MMFBGs, and furthermore, we will be able to check the simulated results with a new defined

parameter, called *quality factor*, which has a very special importance in the rest of our discussions.

When dealing with single mode or two modes FBG problems, we can understand the physical insight perfectly well as is well known. But if more than two modes are involved a much more complicated mode coupling occurs which leads to difficulty in getting a feeling of the physical interpretation of the MMFBGs spectra. We deal with this by proposing a new factor Q to determine the all likely couplings and weigh their respective contribution account to the grating spectra at a given wavelength. The definition of factor Q is based on a fact that a Bragg grating will couple various modes in reflection and transmission provided two conditions are satisfied:

- 1) phase synchronism and
- 2) sufficient mode overlap in the region of the fiber that contains the grating.

The phase-matching condition, which ensures a coherent exchange of energy between the modes, is given by

$$(n_{eff,i} + n_{eff,j}) \cdot \Lambda = \lambda_B \quad (4.92)$$

where $n_{eff,i}$ and $n_{eff,j}$ is the refractive index of the i th and j th propagating mode.

A useful way to understand this requirement and its importance is to combine the mode-coupling with phase-matching condition altogether in a factor Q . This quality factor is proportional to the strength of the coupling and decided also by phase-matching condition. These two phases are connected inseparably and will contribute to the reflected or transmitted peak in company.

For our MMFBG model, Q factor is a very important and clear indicator to show which coupling event is most likely and, in addition, how many coupling events are really taking place. The modes which are involved in the coupling process are the modes that make Q some values. The mode which makes Q a maximum compared with any other pairs is the mode that dedicate to the spectral peak mostly.

We are going to use reflection FBG with four-mode coupling as an example. Return to Fig. 4-5, for each reflected peak we will give the corresponding output Q factor diagram in the following.

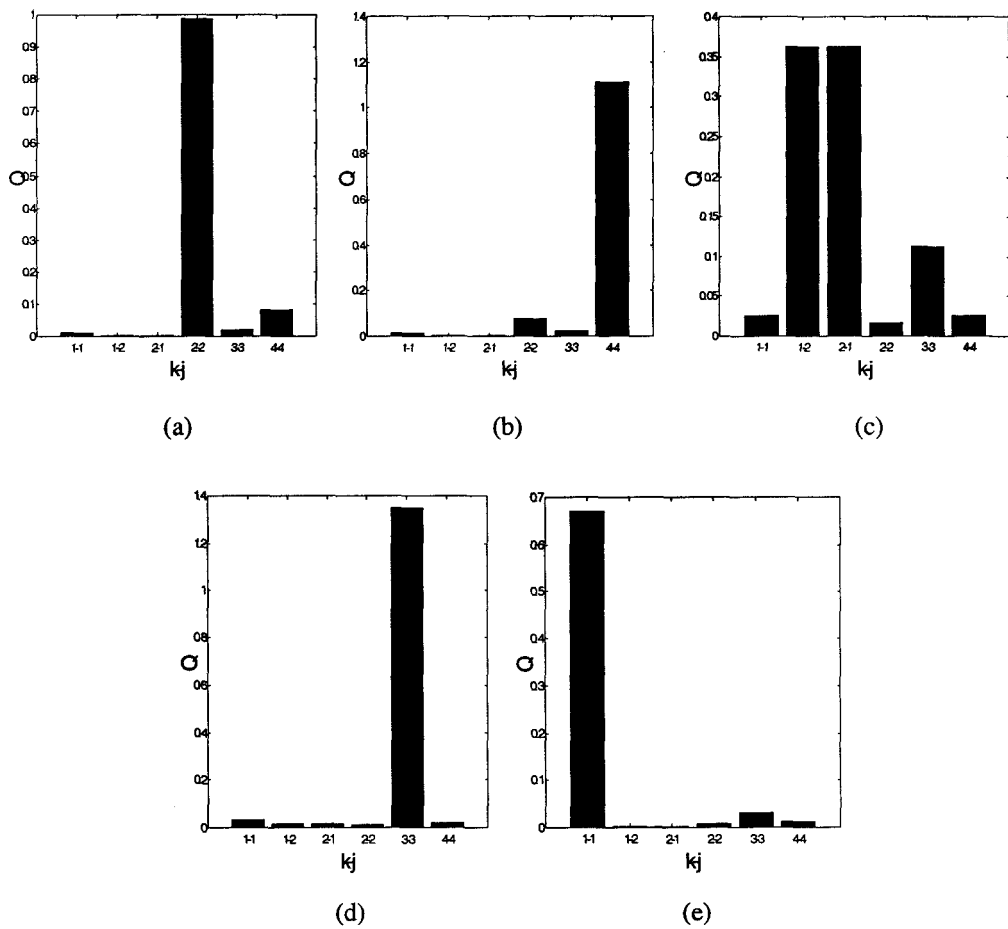


Fig. 4-12 A quality factor Q diagram illustrating the coupling physical insight for a four-mode FBG. (a)-(e) are the Q factor analysis corresponding to the five major reflection peaks, respectively.

Thus, the Q factor diagrams confirm our qualitative explanations for the features of the four-mode grating interaction (see Fig. 4-6). They also provide new physical insight into the dynamics nature of the responses.

4.5 Summary

A generalized physical model is developed and implemented numerically for modeling and simulation of MMFBGs. The achievements as far as concerned in this chapter form the basis and nucleus of theory and application for the rest of this thesis.

Therefore, we here summarize in more detail as follows:

- Coupled Mode Theory is a method to analyze the light propagation in perturbed or weakly coupled waveguides. It has been widely used and proven to be one of the most productive and efficient methods for the analysis of waveguide devices. The basic idea of the Coupled Mode Theory is that the fields of the perturbed fiber at position z can be described by a superposition of the fields of the complete set of bound and radiation modes of the unperturbed fiber. An individual mode of the set does not satisfy Maxwell's equations for the perturbed fiber, and hence the perturbed fields must generally be distributed between all modes of the set. This distribution varies with position along the fiber and is described by a set of *coupled mode equations*, which determine the amplitude of every mode [1-3]. The set of coupled mode equations is obtained by substituting the modal expansion for the fields of the perturbed fiber into Maxwell's equations, and leads to an infinite set of coupled first-order differential equations for the z -dependent amplitude of each mode.
- In view of the above basic idea, coupled mode theory formulations for two categories of multimode fiber Bragg gratings (MMFBGs), independent mode and mode coupling, are derived generally and straightforward, respectively. The problem of propagation and ensuing interaction of optical waves in MMFBGs is cast in these developed coupled-mode formalism.
- The pertinent numerical solution techniques are given and applied to construct the algorithm of both classes. Sequently, a new integrated MMFBG theoretical simulator is successfully developed. It supplies a modeling and simulation tool for the design and analysis of FBGs in MMF structure. Particularly, this newly developed MMFBG simulator is provided with two remarkable advantageous abilities:
 - able to automatically cope with various complicated propagating interactions in FBGs including self-coupling and cross-coupling cases;
 - able to simultaneously calculate mode coupling effects in as many as possible multimode grating structures at any wavelength during the whole spectra range.They will greatly benefit the study of the complex behavior of MMFBGs.

- The multimode fiber Bragg grating spectrum, which comes from mode coupling of both self-coupling and cross-coupling modes, was modeled and simulated using the robust MMFBG simulator based on the coupling equations for MMFBGs. In particular cases, this modeling and simulation does give an insightful and often predictive characteristic description of MMFBG spectral responses.
- An important dynamic quality factor Q has been proposed and it provides a very convenient way to get a feeling of the physical interpretation of the MMFBGs spectra. In this way, we can see that the modeled and simulated MMFBG spectra display an obviously reasonable physical meaning. This together with the analytical proof validate our theoretical model and further verify our numerical MMFBG simulator.

The grating spectrum under actual experimental and ideal theoretical conditions are to be modeled and simulated for the purpose of experimental analysis and device design in the following Chapters 5 and 6 correspondingly.

CHAPTER FIVE:

EXPERIMENTAL STUDY AND ANALYSIS FOR MMFBGS

Fiber Bragg gratings are vital in the field of telecommunication and fiber sensors and have a promising future in communications technology. This is basically because a fiber Bragg grating can be designed to have an almost arbitrary, complex reflection response. In this chapter, we carry out a detailed experimental study on MMFBGs spectral properties. We first describe the experiments, both in system set-up and measurement result aspects. In the subsequent section all the details on the simulations are given and performances on the grating in terms of reflection characteristics are demonstrated. It is closely followed by a comparison between the experimental simulation and results and a discussion of various conditions. Finally, the current limitations that enter the theoretical description and affect the experimental results are also discussed in Section 5.5.

5.1 Experimental Setup

An experimental configuration, shown in Figure 5-1, was developed on a floating optical bench to investigate the properties of fiber Bragg gratings. The inset shows an alternative arrangement for a different mode excitation condition using the mode scrambler. The experiments were performed using a broadband source (BBS) with a single mode fiber (SMF) pigtail, which provides sufficient outpower for the measurements. The experimental setup employs a variety of graded-index MMFBGs which have been fabricated by the phase-mask method in standard graded-index silica multimode fibers. One end of the MMFBGs are connected to one of the output fibers of a 50:50, 2 by 2 multimode optical fiber coupler. The other end of the MMFBGs and the output end of the coupler are angled disposed, equivalent to be placed in

index matching gel. At the input end of the coupler, one optical fiber is connected to the light source through the SMF and the other optical fiber feeds reflected signal to an optical spectrum analyzer (OSA). The reflected light was observed and measured by this Ando AQ-6317B optical spectrum analyser with a resolution of 0.01nm. Reflections just above the noise floor of the spectrum analyser are easily displayed.

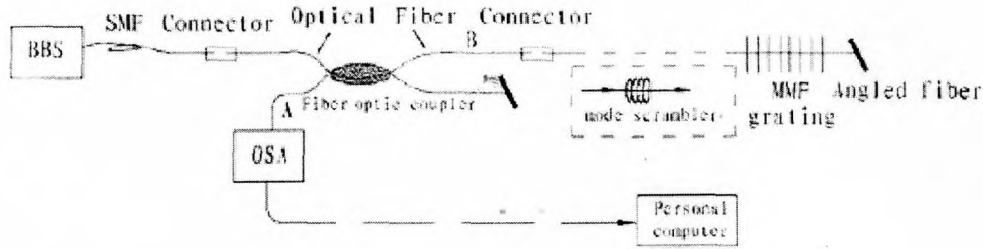


Fig. 5-1 Experimental setup of the reflectivity measure in MMF Bragg gratings

5.2 Experimental Results

The most sensitive method for the detecting gratings is in reflection, and for this reason it is best to measure gratings in reflection for diagnostic purposes. The measurements are made by the following procedure:

First, the output power P_1 at B arm and P_2 at A arm of coupler are measured without and with MMFBG condition, respectively. Then the powers of the two arms, P_1 and P_2 , have the relationship given by

$$P_2 = P_1 \cdot \eta_1 \cdot R(\lambda) \cdot \eta_2 \cdot \eta_c \quad (5-1)$$

where η_1 and η_2 denote the forward and the backward optical coupling of the connector, and η_c denotes the coupling feature of the fiber optic coupler. $R(\lambda)$ is referred to as the reflected signal from MMFBG. In our system, $\eta_1 = \eta_2 = 92.5\%$, $\eta_c = 47\%$.

After processing (5-2) using a computer, the desired $R(\lambda)$ for the MMFBG can be obtained eventually.

$$R(\lambda) = \frac{P_2}{P_1 \cdot \eta_1^2 \cdot \eta_c} \quad (5-2)$$

If the far end of the MMFBGs are absence of angled fiber, an additional 4% reflection from the cleaved far end of the fiber is used to calibrate the actual reflection from the grating. Eq. (5-1) is then substituted with

$$P_2 = P_1 \cdot \eta_1 \cdot R(\lambda) \cdot \eta_2 \cdot \eta_c + 4\% \cdot \eta_2^2 \cdot \eta_c \cdot P_1 \quad (5-3)$$

To investigate the dependence of reflectivity on refractive index modulation experimentally, a set of nominally identical gratings with various refractive index changes were written from Avensys (former Bragg Photonics). Measured reflection spectra with the fixed launching condition are illustrated in Fig. 5-7.

Excitation condition dependence of the MMFBGs can be observed from Fig. 5-9. The reflection spectra of one of the formed gratings were measured using different mode excitation conditions: one is with mode scrambler and the other is without mode scrambler, before coupled to MMFBG.

To penetrate into the mode excitation characteristic, varying modal distribution was applied to the fiber using a scrambler for inducing mode coupling in the optical fiber. A mode excitation test has been done by placing the MMF in an intensity-controlled scrambler; the mixing or scrambling strength was varied from weak to strong by adjusting an accurate graduation on scrambler. At the same time, the corresponding modal distribution in the MMFBG modulated by variation in the status of the mode scrambler. Fig. 5-10 exhibits a spectral tendency under representative modulation of mode excitation condition.

5.3 Modeling and Simulation for Experiments

The simulation we will present is based on the mode solver and grating solver developed in the previous sections. As an application, numerical modeling and

simulations are performed in order to interpret and understand experimental behavior. This section will show how the MMFBG can be modeled and what the MMFBG spectrum will look like under our experimental conditions.

5.3.1 Mode Construction

We used standard graded-index MMF for fabrication of Bragg gratings. Parameters of the best fiber were as follows: core radius $a_1 = 31.25\mu\text{m}$, numerical aperture $NA = 0.27$, core refractive index $n_1 = 1.46$, and cladding radius $a_2 = 62.5\mu\text{m}$. With this condition, we can readily calculate the fields of this structure and explicit relationship between normalized propagation constant and normalized frequency, the propagation constant distribution versus wavelength and the coupling coefficients that will be used in Section 5.3.2.

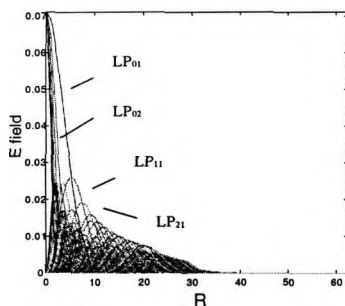


Fig.5-2 Intensity distribution of electrical fields in GI-MMF structure.

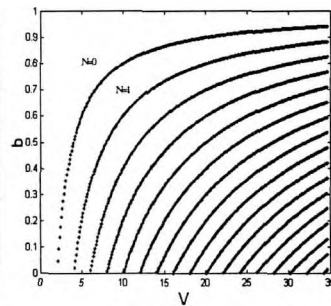


Fig.5-3 The dependence of b on V in graded-index multimode fiber.

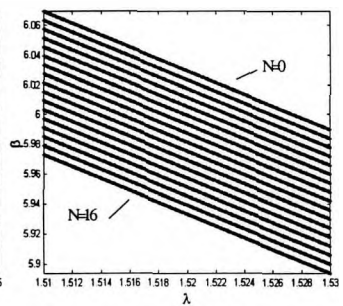


Fig.5-4 The propagation constants as a function of wavelength in GI-MMF.

Figure 5-2 shows the intensity distribution of optical fields. The variation of b with V forms a set of universal curves, which are plotted in Figure 5-3. From Fig. 5-2 and Fig. 5-3 it can be seen that although 81 modes existed in our graded-index MMF, in effect, they are degenerated into only 17 principal modes as appearance. Furthermore, from the calculated propagation constants for our MMF, as illustrated in Fig. 5-4, we can also see 17 principal modes are bound modes to the regime of our

interest at around $1.52\mu\text{m}$. More notably, the differences between every neighboring propagation constant are similar to each other, which will bring out a few interesting phenomena during the grating spectral response in such MMF structures.

5.3.2 FBG Spectral Response Simulation

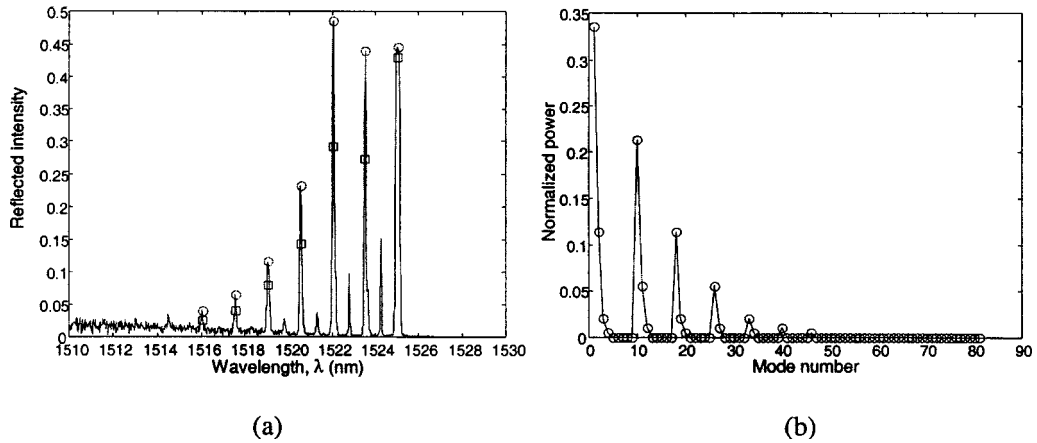


Fig. 5-5 An example for MMFBG without mode scrambler (a) illustration of mode excitation extraction (b) distribution of mode excitation condition.

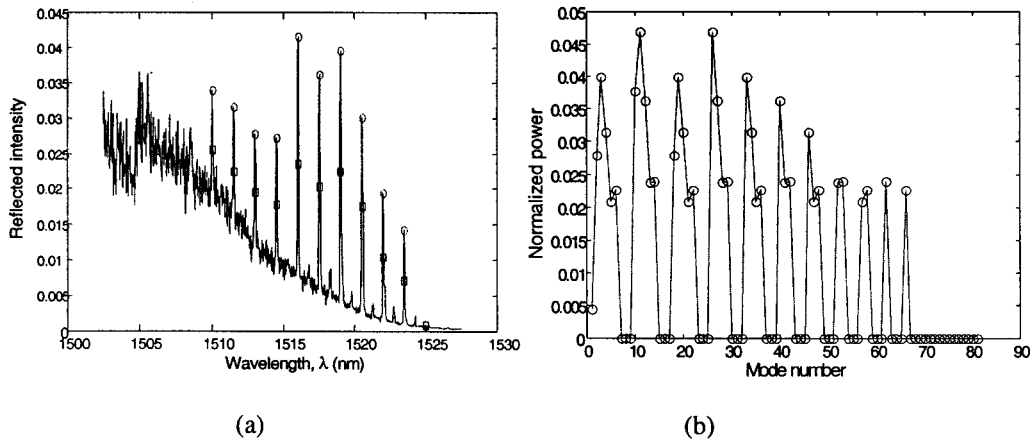


Fig. 5-6 An example for MMFBG with mode scrambler (a) illustration of mode excitation extraction (b) distribution of mode excitation condition.

In order to gain the MMFBG spectra, further necessary parameters describing grating characteristic and mode excitation conditions with which to initialize the input distribution of propagating modes in the MMF need to be clarified. The gratings are approximately 1cm long, have a peak reflectivity ranging from 78% to 99.39%, and are designed to reflect the fundamental (core) mode of the fiber at $\sim 1525\text{nm}$.

In general, we assume the excitation condition as the equally distributed mode population. However, in reality, the excitation condition is far more complicated than ideal situation, and at the same time, the accuracy of the equipment that we are using and the way we choose to use it play very important roles as well. In our simulations, we take the properties of mode excitation and the experimental system's resolution into account.

The approach we extracted the specific mode excitation conditions directly from the experimental data has been illustrated in Fig. 5-5 and Fig. 5-6. Typically, we here just take the most sophisticated circumstances for an example. The other distributions are also obtained from the measured data in a similar manner. Figs. 5-5 and 5-6 clearly tell us the power assignment account for every mode propagating in the MMF. They also tell us that the actual experimental conditions do not satisfy the average mode power distribution (MPD) condition, whereas the power diversity emerged in Fig. 5-6 was alleviated much more than that presented in Fig. 5-5.

The simulated MMFBGs spectral responses for our experiments are presented in Figs. 5-7, 5-9, and 5-11.

5.4 Comparison between Experimental and Simulation Results and Analysis of Various Conditions

In this section we compare experimentally measured reflection spectra with simulations based on our MMFBG model and numerical procedures described previously to examine the accuracy of the above theory and to explain the reflection

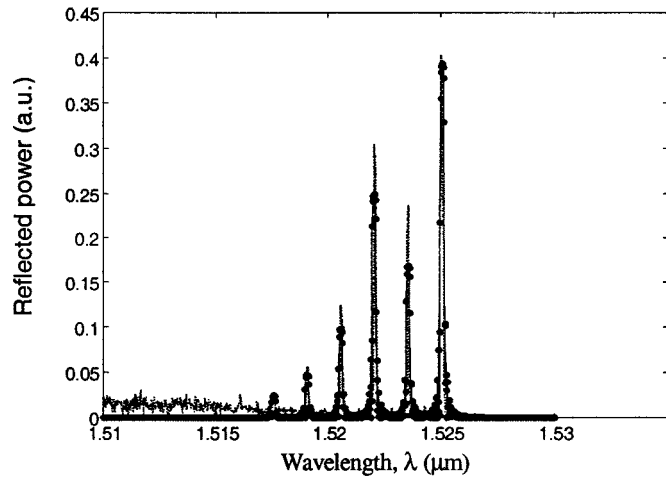
spectra of MMFBGs.

First we examine the resultant reflection response for gratings with the same mode excitation situation but varying in refractive index modulation. Fig. 5-7 (a) shows the multimode reflection through a weak grating, whilst Fig. 5-7 (b) shows the reflection through a relatively stronger grating both of whose parameters are noted above in the Section 5.3. Here the theoretically simulated reflectivity spectra are plotted in solid lines, and the measured spectra with a 0.01-nm spectrum analyzer resolution are plotted in broken lines. A prominent feature observed in Fig. 5-7 is an approximately uniform frequency spacing of 1.5nm with respect to the main reflection peak. This phenomenon can be explained as follows. The difference in propagation constant β corresponds to the separation between the neighboring major peaks. Typically for standard GRIN MMFs, the mode characteristics which are almost equivalently spaced during the wavelength regime in the even spacing in the associated MMFBG spectra. Indeed, one may make a simple estimate of what this spectral spacing should be from mode spacing. The results turn out to be the same value of 1.5nm as measured in Fig. 5-7. Thus our calculations match very well with experiments.

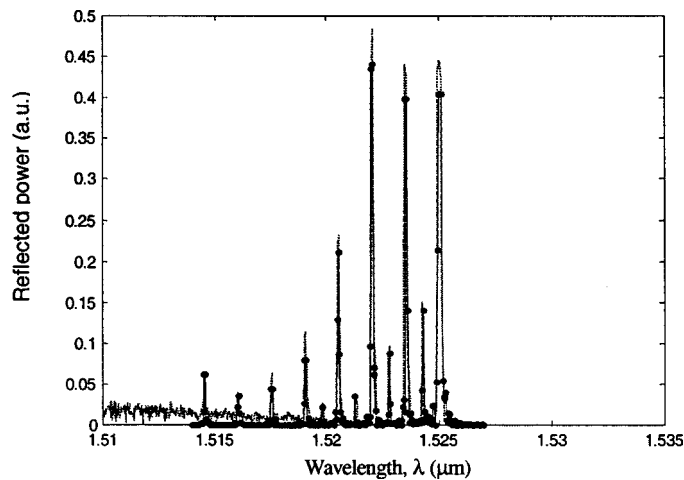
To summarize the principal peaks in Fig. 5-7, the strongest resonance at 1525nm is due exclusively to $LP_{01} - LP_{01}$ Bragg reflection; the reversely second major peak is caused by the next lowest order mode $LP_{11} - LP_{11}$ coupling; the resonances at shorter wavelengths result from couplings of core modes with lower-order higher-sequence or higher-order but lower-sequence parameters, they would be LP_{02} , LP_{21} , LP_{12} , LP_{31} , and so on, alternatively speaking higher order N in terms of principal modes; and at even shorter wavelengths counterpropagating coupling with $N = 5, 6, 7, \dots$ principal modes occur, might comprising degenerate modes like LP_{03} , LP_{22} , LP_{41} , etc.

Also note that several pronounced fine structures between the main reflection peaks come out in Fig. 5-7 (b). This indicates that additional mode interaction events are involved and important in this region. It is well known that optical fiber, being a physical medium, is subjected to perturbation of one kind or the other at all times. It therefore experiences geometrical and optical changes to a larger or lesser extent

depending on the nature and the magnitude of the perturbation. In large index modulation situation, the grating can be caused strong nonuniformity in the local area cross the core by ultraviolet radiation. This photosensitive nonuniformity complicates the reflection response of an MMFBG considerably. Consequently, in practice the situation susceptible to additional mode coupling involvement is not as simple as that indicated in Fig. 5-7 (a).



(a)



(b)

Fig. 5-7 Comparison of experimentally measured and theoretically calculated MMFBG reflection spectra with maximum reflectivity of (a) $R = 91\%$ and (b) $R = 99.39\%$. The dashed lines show the measured response, and the solid lines show the calculated results, with a 0.01nm resolution.

Regarding a uniform grating both longitudinally and transversally, cylindrical symmetry eliminates coupling between modes with different harmonic parameter, because the harmonic functions of different order are orthogonal [7]. However, when the transverse profile of the refractive index is nonuniform, dissimilar mode orders that normally cannot couple owing to the *orthogonality relationship* are allowed to couple as can be evaluated from the generalized MMFBG governing equations and coupling coefficients described in Chapter 4. This changes the coupling interactions in a multimode fiber for the grating and, hence, its spectral response.

The mechanisms contributing to photosensitivity are complicated and still being debated. The lack of a thorough understanding has not, however, prevented the exploitation of the effect in a large number of applications. In this work we still not deal with the issue of the microscopic mechanism for fiber photosensitivity. Instead, our purpose and emphasis will be on the whether or how this transversally photosensitive effect has significant consequences on the reflection spectra of MMFBGs.

Now, we take into account the photosensitivity effect in our simulation. For simplification, we also assume that the silica cladding of the fiber is not significantly modified by the ultraviolet light, in accord with experiment, so that the grating only exists in the core. Our numerical calculations tell us that the transverse grating profile strongly modifies the nature of the mode interaction and influences the spectral properties. Specifically, when orthogonally polarized modes of the different order can overlap with each other, then interactions will take place between symmetric and asymmetric modes in such a multimode fiber grating structure. As seen in Fig. 5-7 (b), for example, the grating destroyed the orthogonality and coupled the fundamental LP_{01} mode to the next lowest order mode LP_{11} . But with an uniform photosensitivity profile, the coupling between them is zero. Also, the wavelength to be reflected is consistent with the phase-matching condition.

For the general case of dissimilar the i th and j th modes, the phase matching condition is

$$\beta_i + \beta_j = 2\pi/\Lambda \quad (5.4)$$

equivalently,

$$(n_{eff,i} + n_{eff,j}) \cdot \Lambda = \lambda_B \quad (5.5)$$

in reciprocal case,

$$2n_{eff,i} \cdot \Lambda = \lambda_{B,i} \quad (5.6)$$

$$2n_{eff,j} \cdot \Lambda = \lambda_{B,j} \quad (5.7)$$

then the wavelength of reflection is related to the average effect

$$\lambda_B = (\lambda_{B,i} + \lambda_{B,j})/2 \quad (5.8)$$

which means the Bragg wavelength is in the middle of those the i th and j th mode reflection. Obviously, the first subpeak from the right side is attributed to the reflection of the lowest-order $N = 0$ (LP₀₁) mode to the next lowest-order $N = 1$ (LP₁₁) mode. Similarly, the second subpeak is attributed to the reflection to the next neighboring modes: the $N = 1$ and the $N = 2$ modes, and the rest can be deduced by a analogy. These wavelengths agree excellently with those of experiment in Fig. 5-7 (b). Therefore, in this way we reproduce the fine structure and explain the main features of our stronger grating.

It can be seen that there is good agreement in terms of both the locations and the strengths of the resonances for Figs. 5-7 (a) and 5-7 (b) (weaker and stronger, respectively) cases. Further, this spectral analysis suggests that it is important to also have the spatial dependence of index perturbation perpendicular to the propagation direction included in the MMFBG model as the gratings get stronger in order to adequately account for the observed spectral properties. On the contrary, these features of subpeaks structure do not occur if the refractive index change is held constant.

However, it is essential to alert that there are more complete and also complex approaches that take photosensitive response characterization into account and in some circumstances need to be used in order to obtain more accurate results. It is fundamentally decided by fibre photosensitivity. Generally speaking, photosensitivity

is one kind of material characteristics: when some material expose to the external light, its physical or chemical characteristics will change temporarily or permanently. It depends on many physical factors such as Germanium doping amount, glass structure, etc. In consequence, in order to intrinsically recognize and resolve this problem, it is a must to penetrate into the photosensitive characteristics of materials meticulously.

An alternative way of looking at the various interaction regimes of identical and nonidentical mode coupling discussed above in the multimode fibre Bragg grating with an uneven, not-well-distributed transverse profile of photosensitivity is coupling coefficient and phase-matching maps. These diagrams are plotted in the root matrix dimension plane, as seen in Fig. 5-8. The shallow in the area in the plots represents

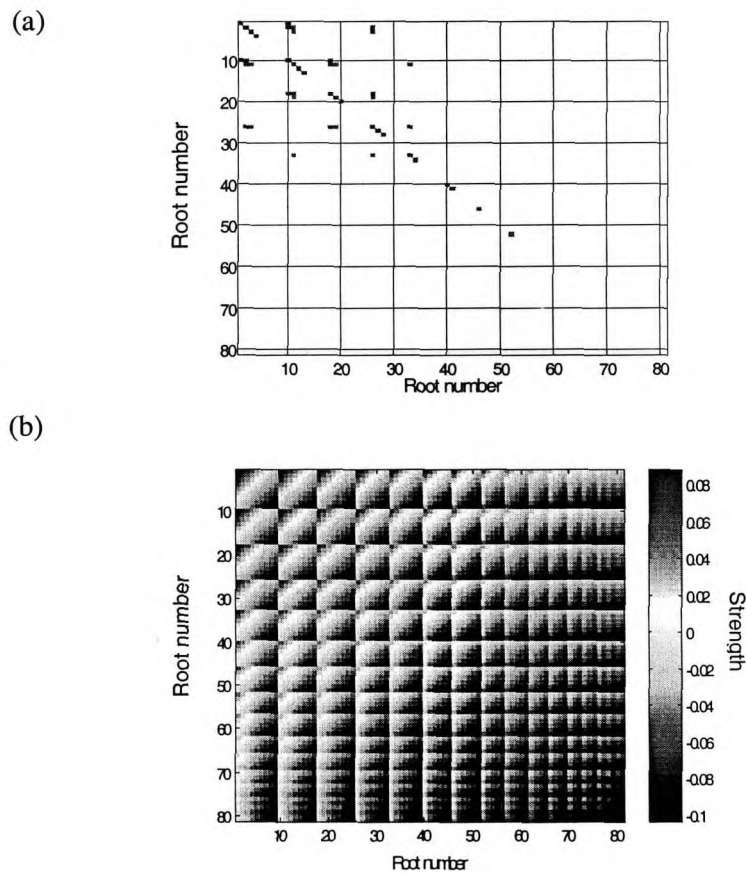
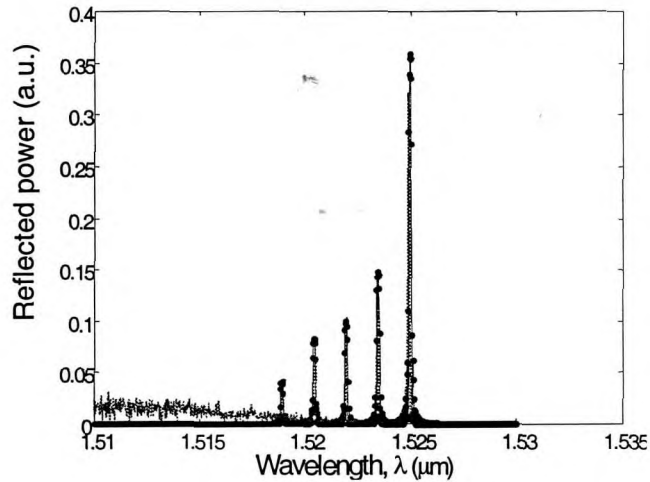


Fig. 5-8 Topographic maps that illustrate (a) coupling coefficient deployment, and (b) phase-matching condition, or Bragg reflection condition.

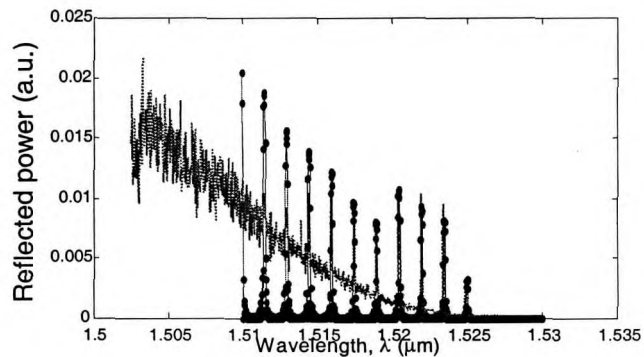
the effects of wave interaction in coupling and phase separately, and the chroma in the shades stands for the intensity (the strong and the weak) of each coupling and how far phase condition is satisfied by the behavior of the guided wave. Figure 5-8 (a) shows the coupling coefficients for a certain wavelength. The relevant detuning factors are displayed in Fig. 5-8 (b) for directly perceiving the phase-match and phase-mismatch states. These figures graphically illustrate the coupling strength deployment and the phase-matching conditions necessary for grating coupling between two modes in the multimode physical configuration and provide a better understanding of the characteristics of the complex MMFBG behavior.

We next consider the spectra of the reflection signal from the same Bragg gratings in a multimode optical fiber but with different excitation conditions. In our experiments, two arrangements of excitation conditions were performed. One was implemented utilizing a BBS with a SMF pigtail connected to the MMF by an alignment welder. The other introduced a mode scrambler just before the grating based on the similar topology shown in Fig. 5-1. The reflection spectrum for the former case is shown in Fig. 5-9 (a). The actually measured response is perhaps initially surprising and may not be expected by simply considering the ideal theoretical and numerical procedures. It shows a few more reflectivity peaks than calculated predictions. Even with a higher frequency resolution, the shorter wavelength resonances are not visible with the forecast. This justified that the resolution itself is not responsible for the disagreement between the two results. The number of Bragg resonances on the measured spectrum is, with certainty, somewhat more than that as anticipated. This discrepancy suggests that the actual launching condition was not ideally core-to-core aligned used for the theoretical prediction. In theory, a physical center alignment for SMF-to-MMF will stimulate only symmetric modes. Alignment variation results in excitation of a greater number of modes. Good agreement on the number of Bragg resonances can be obtained by the use of actually experimental launching situation for the calculation as solid curve depicted in Fig. 5-9 (a). Therefore we infer that the initial disagreement originates from the fact that the

actual fiber-index profiles are not perfectly geometrical symmetric across the fiber face, as assumed for the predictive calculation. So it is not surprising in that our plausible treatment here is just realization of a geometric dimension alignment. In effect, the maximum refractive index has deviated away from the center of the plane. As a result, the core index physical alignment was not approached in real situation.



(a)



(b)

Fig. 5-9 Comparison of experimentally measured and theoretically calculated MMFBG reflection spectra with excitation conditions of (a) SMF-MMF launching without scrambler and (b) SMF-MMF launching with mode scrambler. The dashed lines show the measured response, and the solid lines show the calculated results, with a 0.01 nm resolution.

Fig. 5-9 (b) shows a reflection spectrum obtained with the use of a mode scrambler prior to the same MMFBG. The observed spectra in this condition were very different from the previous case without scrambler. There about nine reflection wavelengths appeared within a range of 15nm. The number of ripples increased substantially up to almost twice that of the former, and the peak modal reflectivities decreased as a spiky, almost random modulation impressed on it. This is considered to be because the presence of a scrambler effectively disturbs the mode population via inducing strong mode coupling, resulting in the generation of higher order waves, but that not associated with the original signal. Therefrom, the scrambler provides a modal power distribution (MPD) incident on the grating which is largely independent of the optical source and the reflectivity spectra of multimode FBGs are dominated by this scrambling modulation on the excited modes. Notice that, for reasons of measurement accuracy, what is actually observed has been posed some limitation. The system's noise limits the visibility of more principal modes in the measured spectra of Fig. 5-9, according to our modal analysis exhibited in Section 5.3. The solid lines in Fig. 5-9 show the simulated numerical results, where the values are computed on the basis of the measured data from the zeroth mode on. Again there is good agreement between theory and experiment. These results show that the reflection spectra of a Bragg grating in MMF depend on the conditions of excitation of modes. Measurements using a SMF-pigtailed BBS correspond to lower order mode excitation, and those using a mode scrambler (MS) correspond to highly multimode excitation.

A more careful comparison is made for clearly indicating the transformation in MPD via scrambled mode coupling behaviors. Several special cases during regulating the scrambler modulation conditions were measured in Fig. 5-10. The scrambler is behaved as the MPD input to the grating and the reflected signals from various excitation conditions take on significantly different spectral shapes. Nevertheless, some of their features also exist in the former gratings. For example, these principal reflection peaks are nearly uniformly distributed over most of the wavelength range

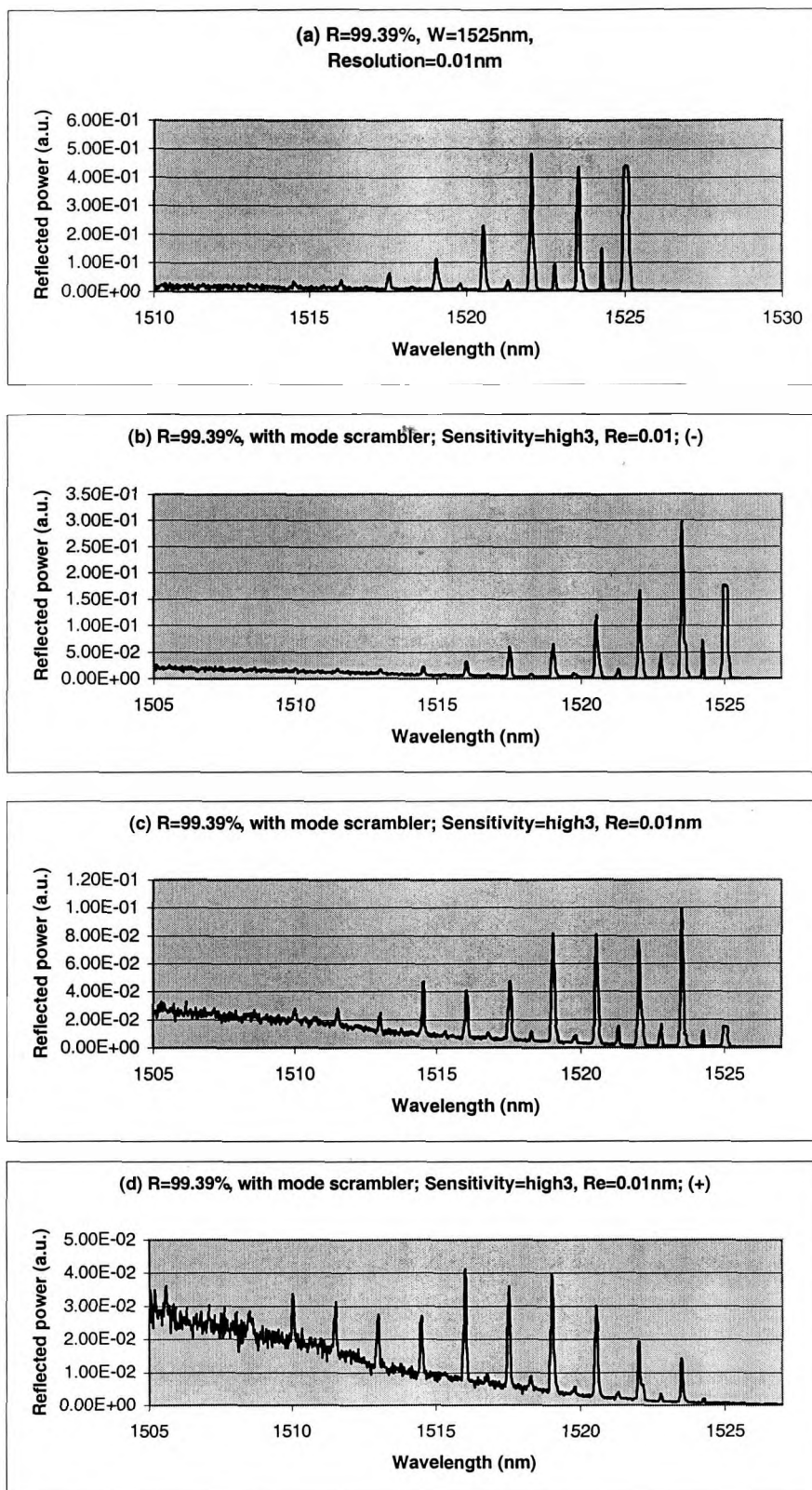


Fig. 5-10 Experimentally measured MMFBG reflectivity spectra for mode scrambling excitation with (a) absent, (b) slight, (c) medium, and (d) strong modulation, respectively.

and the separation between them is 1.5nm, which comes directly from mode spacing. In particular, a few subpeaks between the main reflections show up as well in the plots, which is in consistent with the observation from Fig. 5-7 (b). The above explanation of the mode interaction with the stronger grating also applies to such fine structures; however, the latter responses for subpeaks are insignificant since they do not interfere constructively with the main spectral performance. Thus, in order to restrict our attention to the principal reflection tendency that MMF grating exhibits with scrambler modulation, we do not consider rigorous treatment and only take the significant coupling events into account. As a result, an approximate calculation could be obtained in the absence of the subpeaks effect. Fig. 5-11 shows a plot of the simulation result for a specific case under strong scrambler modulation corresponding to Fig. 5-10 (d). It is comforting to note that this is still a reasonable approximation to the real spectrum in the presence of the small sharp spectral resonances.

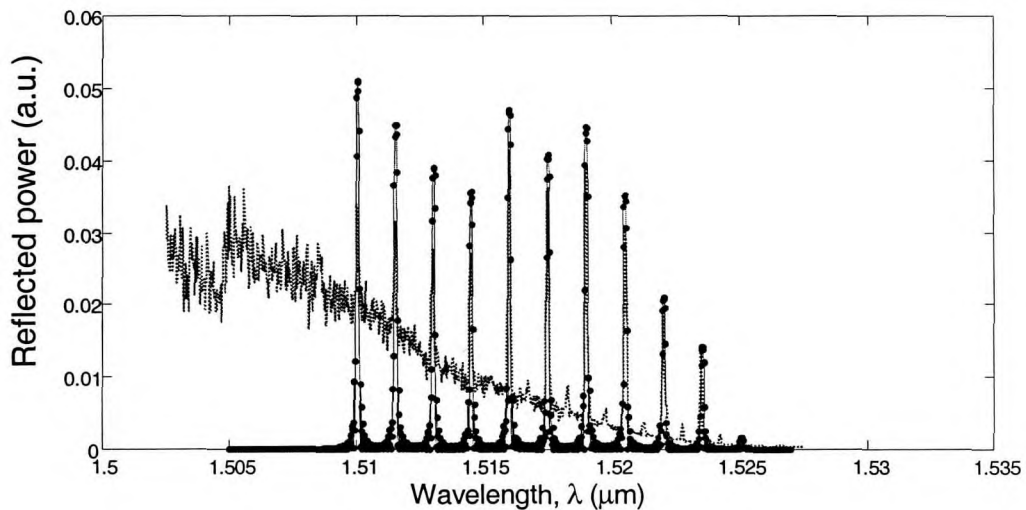


Fig. 5-11 Corresponding calculated reflectivity spectra of Fig. 5-10 (d) assuming a 0.01nm wavelength-resolution simulating. Here, we neglect subpeaks effect with the same explanation as Fig. 5-7 (b).

By studying the envelop of Fig. 5-11, one quickly finds that the reflection spectrum for this condition mimics a ladder raising from right side, bearing a striking similarity to the grating spectra with equal MPD where higher multiplicity grows toward the short wavelength side as a result of mode degeneracy. In this case, mode scrambler acts much like a free gas collision chamber. The various MPD states are described by modulations as far as the power exchanges among the excited modes are concerned. Evolution of the scrambler modulation will run parallel to the energy exchange analysis of an equilibrium gas system. This initial state is a chaotic state of energy level, and the final state is an energy balance of gas molecules. In an analogous approach, the mode scrambler produces mode coupling redistribution effect. The excitation conditions involved are then easily identified, and the most elegant — when appropriate adjust to the scrambler graduation, it can be situated such that in the fiber all modes are excited independently and sufficient exchange of power among all these modes can occur. Finally excitation conditions emerge to an average MPD incident on the grating. In the case of Fig. 5-10 (d) and alternatively Fig. 5-11, we found that it is indeed on the way approaching to its averaging state. By contrast Fig. 5-10 (d) to Fig. 5-11, we also see that for this grating the neglect of subpeak phenomenon causes the theoretical calculation a slightly larger apparent discrepancy with experiment than in Fig. 5-7 (b). Additionally, the various noises, as pointed above, associated with the optical diagnostic system limit the ultimate detection capability. The signal obtained from the MMFBG is obscured by noise and this may lead to an incorrect result for the peak number and peaks absolute reflectivity. But on the whole, the theoretical calculation still shows overall accordance with the measured spectra. Furthermore, it was shown that mode scramblers not only have the ability to excite higher order multimode, but also have the capability of tending to equalize the MPD of the light in a fiber.

5.5 Current Limitations and Future Experiments

We calculated and experimentally observed the reflection properties of MMFBGs.

It turns out that the numerical results are in good agreement with the measured data. Although the simulation results are very optimistic, in this section we still review the approximations that enter the theoretical description and the difficulties that affect the experimental results. The goal is not only to uncover the sources of the discrepancies in this work but also to identify the strategies of the improvement in future experiments.

There are two main assumptions included in our theoretical treatment, as detailed below:

First, the mode power distribution stemmed from the experimental spectra is assumed as grating mode excitation condition for all of the calculations. We feel that this assumption is largely responsible for the disagreement between theory and experiment. Even the more accurate calculation of the spectra can be performed based on spectral shape rather than actual values of reflection, inevitably, however, the difference between calculation and actual situation of launching or mode mixing condition still results in somewhat discrepancy as before.

Second, the photosensitive effect assumption is perhaps another possible culprit responsible for this slight disagreement. Although we are going to make a detailed study of this assumption, the rough estimates indicate that it still places limits on the accuracy of our theoretical simulations.

Deliberatively, some proposals of future experiments then follow from the above discussion of the current limitations of our work:

<1> to measure and quantify the practical far-field patterns for determining mode power distribution as required mode excitation condition in a multimode optical fiber reliably and objectively.

<2> to observe and acquire the actual photosensitive characteristic responses for expressing the UV-induced refractive index change as an explanation of subpeaks

behavior in a multimode strong grating accurately and positively.

In addition to the experimental measures just described, it is also important to pay attention to the following aspects.

<3> Coupling of light from source to MMFBG is a significant element and may call for special optical devices. In the present launching condition, it is confirmed experimentally that the uniform excitation, in which all the modes are equally excited, tends to be realized using a MS. But this is based on the sense of linearly polarized mode. The equal MPD in terms of principal mode also desires to be implemented by means of an incandescent lamp such as a halogen lamp or adopting an incoherent Lambertian launch or an LED launch as a light source [69]. On the other hand, as pointed out in Section 5.4, a large variation in mode excitation condition would occur on account of alignment variations. Therefore an attempt is supposed to be made to attain more precise core index alignment through real-time monitoring of the reflection spectra during aiming and accordingly through adjusting the sighting device. Besides, we are in a need to explore intensively extra excitation fashions with the goal of achieving more valuable and appealing spectra.

<4> Experimentally, maintaining the launched mode distribution and yielding reproducible results must be ensured. They are essential requirements for enabling the realization of practical employments in the future. Due to the MMFs in general susceptible to reflected light and environmental conditions, to avoid this problem becomes a critical factor in real MMFBG operation. Limiting the length of fiber between the fiber face and the grating is one of the effective ways to alleviate this problem.

Hopefully, the above suggestions could improve the overall simulation quality with greater ease, and the comparison of theory and experiment would be expected to match better with each other.

5.6 Summary

In this chapter, we have both measured and calculated optical properties of a number of practical fiber gratings that exhibit substantial multimode coupling. The numerical simulations are compared with experimental measurements. The agreement between theory and experiment has been not only qualitatively good but in many cases quantitatively good as well. These good agreement obtained is, once again, evidence that our theoretical development, including the corresponding numerical software package fulfilled in this thesis, has strong validity and high reliability. Simultaneously, the theoretical simulations provide quantitative explanations for the experimental observed phenomena — these explanations gives physical insight, a more complete understanding of, and a means for visualizing the interaction between multimode propagation and short period fiber gratings. To sum up, we can conclude the following:

1. For present experimental conditions, Bragg gratings formed in standard graded-index optical fibers in multimode propagation show multiple reflection peaks in the reflection spectra. Furthermore, there is a prominent common feature of an uniform frequency spacing of 1.5nm between two main reflection peaks resulted from modes and fields characteristics.
2. For weaker gratings, the reflected signal is spike-like with a gradual decrease in intensity toward shorter wavelengths. On the other hand, as the grating strength increases, not only reflection broadened and enhanced, but also, in particular, a physically distinct phenomenon emerged: there is a separation of the reflected subpeak into every two neighboring principal components. Such a pronounced fine structure arises due to the transversal nonuniformity of photosensitive index profile.
3. For lower order mode excitation, fewer reflection peaks appeared and the reflectivities are relatively higher; for highly multimode excitation, the number of reflection peaks increased and the reflectivities reduced accordingly. It can be seen that the reflection spectra of Bragg gratings in multimode optical fibers strongly

depend on excitation condition of propagation modes because of the build-up input power directly determined by mode excitation condition.

Finally, possible theoretical and experimental causes of the slight disagreement between calculated and measured results were discussed. On the experimental hand, the main current limitation and some reformation on the future experiment have been proposed; on the theoretical hand, a further investigation of more sophisticated modeling and simulations will be performed in next chapter.

CHAPTER SIX: THEORETICAL INVESTIGATION OF OPTICAL CHARACTERISTICS FOR MMFBGs

As interest grows in the application of short period in-core fiber Bragg gratings written in photosensitive multimode fiber structures, there is an increasing need to more fully understand their optical properties. Our objectives in this chapter are to systematically characterize the various impact of physical parameters on MMFBG optical performance. We will begin by examining the reflection and transmission spectral profiles for a number of simple and complex grating structures, such as the grating length, period, and index modulation strength. The dependence of the grating spectral response to mode excitation condition is also investigated. Finally, we look at the impact of optical fiber structure effects on the characteristic of fiber Bragg gratings.

6.1 Theoretical Modeling and Simulation

Through model validation and experimental verification performed in previous chapters, it has been confirmed completely that our developed MMFBG simulator is practically feasible and reliable to the characterization of optical properties in a sophisticated MMFBG structure. Using this approach, the deep-going study with various conditions can be greatly facilitated, which we can explicitly calculate light propagation and obtain the transmission and reflection spectra, etc.

Along with the need to understand the functions of MMFBG devices comes the necessity to consider the intrinsic influence of physical characters, and to model and simulate the complex behavior of these devices. In this section, we present simulations of grating mode propagation under a few different types of cases whose

Table 6-1 Physical characteristics of varying gratings used in the numerical simulations

Grating	Designation	Period (μm)	Length (mm)	Index Modulation
1	Weak uniform grating	0.533	10.0	5E-05
2	Medium uniform grating	0.533	a: 10.0 b: 1.0	2E-04
3	Strong uniform grating	a: 0.533 b: 0.535 c: 0.531	10.0	1E-03

Table 6-2 Physical configurations of varying excitation conditions used in the numerical simulations

Excitation Condition	Designation	Features Specifications
1	Single-mode/Multimode Fiber Launch	Core-to-core index alignment such that only symmetric modes are stimulated.
2	Equal Mode Population Distribution	Optical power is distributed evenly among all the modes of the fiber.
3	Gaussian Mode Population Distribution	All modes are excited independently and with Gaussian profile power.

Table 6-3 Physical properties of varying fibers used in the numerical simulations

Fiber	Designation	Core Index	Normalized core-cladding Index Difference	Core Diameter (μm)	Clad Diameter (μm)
1	Single Mode Fiber (SMF)	1.46	0.0029	9	125
2	Step-index Multimode Fiber (SI-MMF)	1.462	0.0094	50	125
3	Graded-index Multimode Fiber (GI-MMF)	1.462	0.0094	50	125

parameters are listed below in Tables 6-1, 6-2 and 6-3, to explore salient physical affect on grating spectral performance. These topics are presented from Secs. 6.2.1 to 6.2.6, respectively. A uniformity property of the grating is assumed as the longitudinal index modulation here. Notice that

- (i) optical property is fundamentally characterized by transmission and reflection spectra that result from a variety of specific parameters. Every time or every case only one of these parameters is chosen as variable and all the rest may not undergo a change such that other conditions will have no effect on spectra and
- (ii) the number of “step” (the number of wavelength segmentation) assumed in the calculations are 500 (stepsize will give limit to distinguishable spectral capacity). Further reduction in $\Delta\lambda$ will certainly improve the calculation accuracy.

In addition to the reflection and transmission spectra, some representative Q factor diagram, coupling strength profile and phase matching map, mode population distribution will also be provided. They are important in understanding the dynamics of the wave interplaying response for these gratings.

In the following subsections, we used our program to perform numerical simulations and qualitatively discuss the MMFBG response in terms of change in grating characteristics, launching conditions and fiber structures.

6.2 Discussions of MMFBGs Optical Characteristics

In this main part of the chapter, the effects of various physical parameters on the transmitted and reflected Bragg responses are examined. As it will be described during the subsequent sections, and by observing the variety of realizations and shapes of the obtained spectra, we will see that there is a high degree of control over

the characteristics of the multimode gratings and their responses can be tailored to generate optimized device performance such that satisfied for use in a high-capacity fiber optic network.

6.2.1 On the Refractive Index Change

In our simulations, the three parameters which can vary and determine the grating characteristics are the grating strength, length, and period. The purpose of this subsection is to demonstrate how the spectral response of a grating is affected as the refractive index of the grating is altered. Fig. 6-1 shows the spectral response profiles from three different gratings, varying in strength from weak to strong. In the modeling, the number of guided mode is assumed six for all MMFBGs. The step index multimode fibers are taken here. Apparently, considerable modifications in shape occur for both the reflected and transmitted spectra and we observe the following features.

First, with increasing grating strength, the reflectivity response becomes broader and the modal peak reflectivity increases due to the strong index modulation and associated strong reflection. It appears that the reflectivity peak approaches a maximum value (or the transmissivity dip approaches a minimum value) and remains constant for further increase in the index of refraction change, whereas the spectrum keeps broadening and evolves into a square-like as well as flat-topped and saturated shape. This phenomenon can be explained as follows. In strong gratings, the light does not penetrate the full length of the gratings, and the effective length will be reduced as the transmitted signal is depleted by reflection. As a result, the spectrum will broaden appreciably and depart from a symmetric sine or Gaussian-shape spectrum. Then the bandwidth is independent of length and directly proportional to the induced index change, which is referred to as “*strong-grating limit*”. This is in contrast to the weak grating where only a small amount of energy is reflected by each grating period so that the incident wave can propagate well through the entire grating.

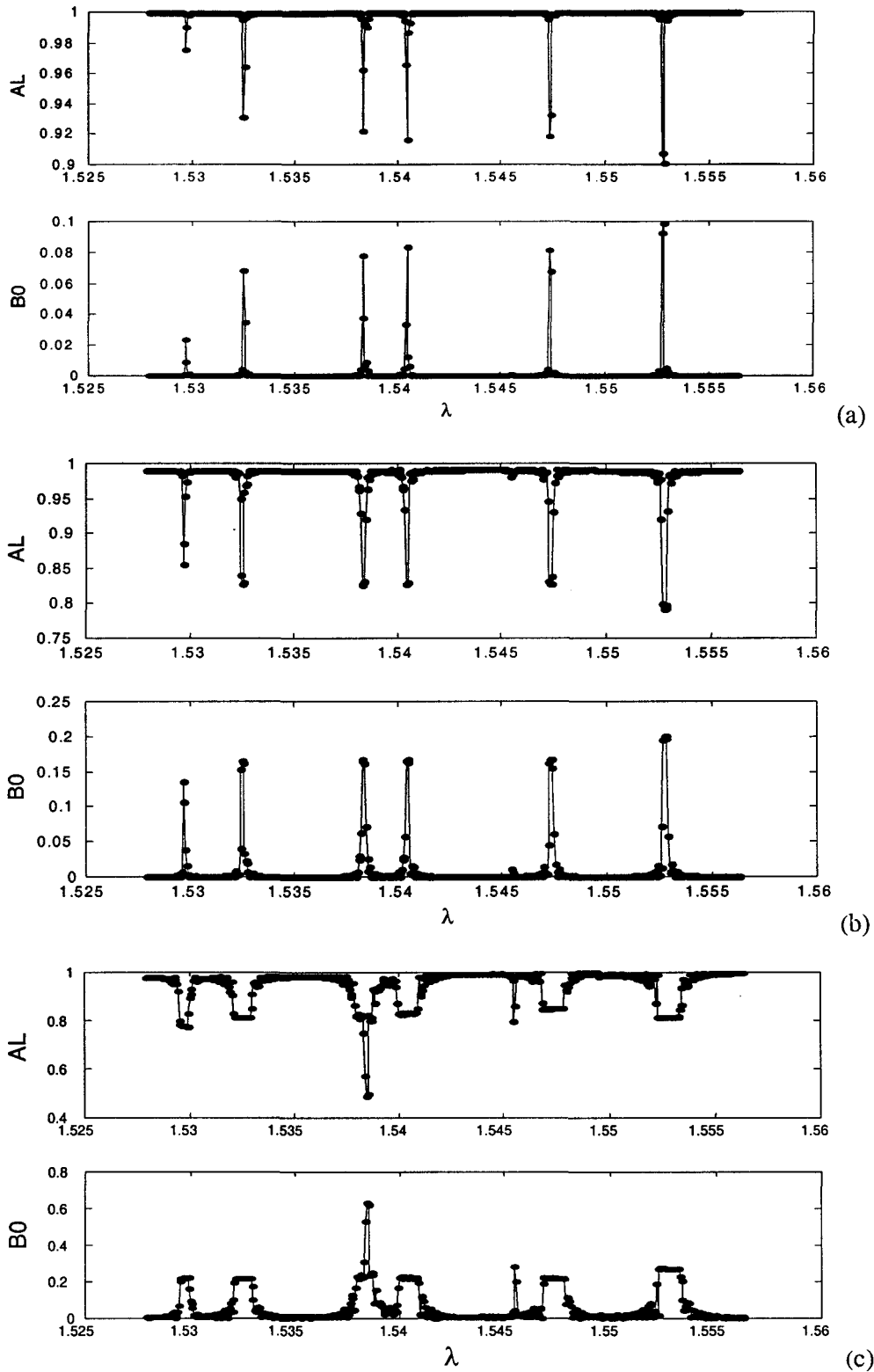


Fig. 6-1 Transmission and reflection response from uniform MMF Bragg grating for different index of refraction change (a) $\Delta n = 5 \times 10^{-5}$, (b) $\Delta n = 2 \times 10^{-4}$, and (c) $\Delta n = 1 \times 10^{-3}$, which, for convenience, are referred to in the text as *weak*, *medium*, and *strong*, respectively.

Next, while for the weaker reflection grating, the bandwidth is much narrower than for the stronger grating, we note that the central peak is bounded on either side by a number of subpeaks and these side-mode structure increases rapidly for stronger gratings. This feature is characteristic of a uniformed-period grating of finite length, similar to the case for single mode Bragg gratings. The abrupt start and end to the grating is responsible for the side structure. This physical picture can be made more rigorous by an effective medium description which will be presented in the latter discussion.

Finally, one of the most important features which is observed in strongly reflecting gratings with large index perturbation is a new Bragg resonance emerged on the wavelength regime of interest. Furthermore, another extraordinary feature along with this effect is that two of the peak reflection regions are sharpened and heightened in comparison with other spectral resonances. The above features result from cross-coupling due to the strong modulation of the refractive index. A theoretical analysis of Q factor on the strong grating is performed in particular in order to gain physical insight into the nature of its response and corresponding interaction. When examining the grating quality factor in Fig. 6-2, we see this effect manifest through Q value selection of these particular reflection wavelengths. At the shortest wavelength, reflected peak is caused by self-coupling of LP_{12} mode traveling in opposite directions; at relatively long wavelength, the peak results from reflection by the MMFBG of higher order core mode LP_{31} into the identical counter-propagating mode; at longer wavelength, in addition to LP_{02} mode self-coupling effect, cross-coupling between LP_{11} and LP_{12} modes, as well as LP_{12} and LP_{11} modes occur. These cross-coupling in Bragg grating also contribute to the main reflection peak for the LP_{02} resonance wavelength, giving rise to this peak; at still longer wavelength, counter propagating coupling with the same core mode LP_{21} leads to the fourth spectral peak; at still longer spectrum zone, once the input wave reaches the resonance wavelength of the grating, it will experience the LP_{01} to LP_{02} cross coupling and then travel-back LP_{02} to LP_{01} wave coupling, coming up with a

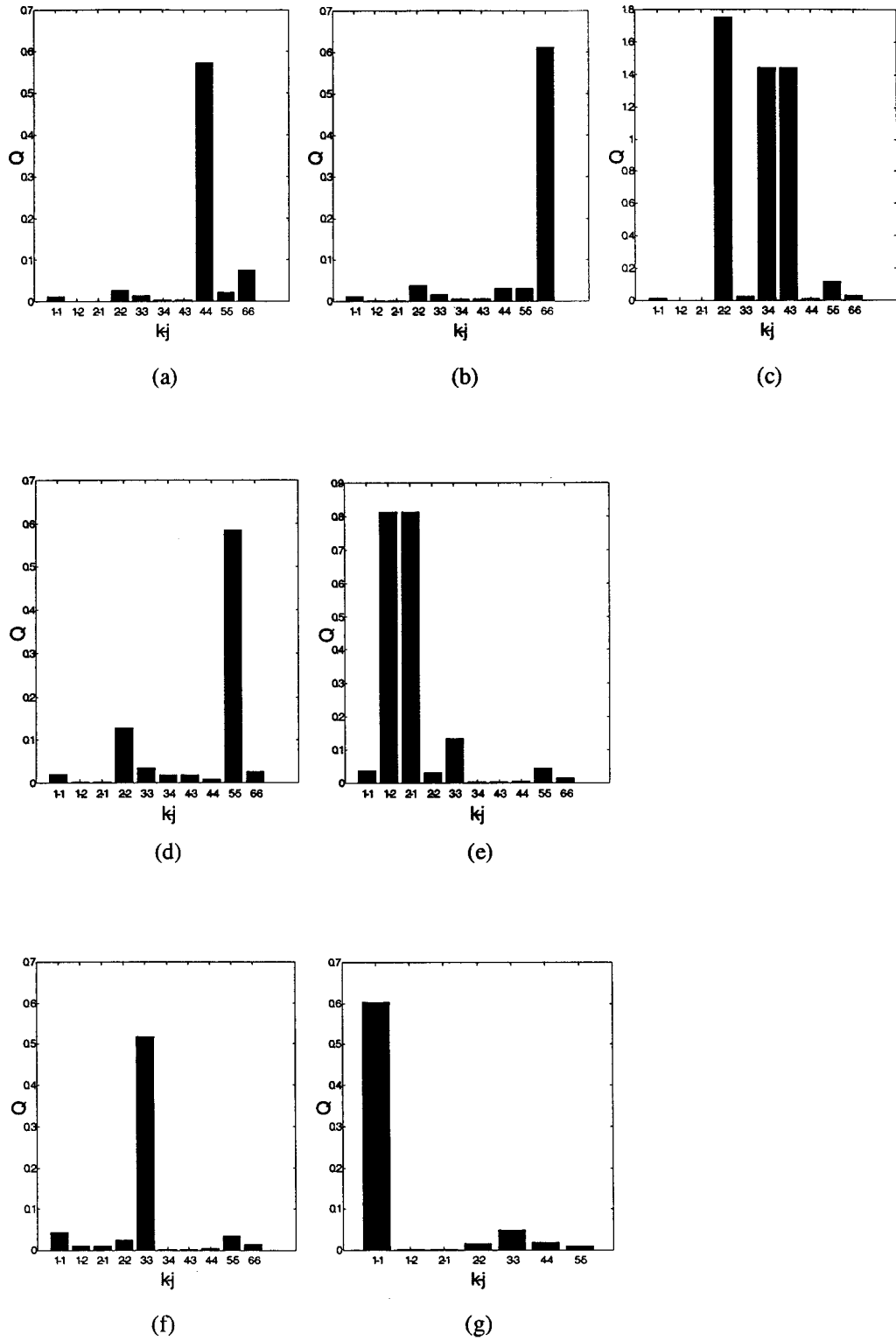


Fig.6-2 Corresponding Q factor diagrams (a) – (g) of the strong uniform grating appearing in Fig.6-1(c)

distinguishing reflection; at even longer wavelength, the grating peak is caused by an identical contra-directional guided mode coupling of LP_{11} mode; and, finally, Bragg reflection of the lowest-order core mode LP_{01} into a counter propagating mode of the same type fundamental mode is phase matched at the longest wavelength. Consequently, factor Q diagrams enable convenient interpretation of grating properties. As is obvious from the above analysis and also from Fig. 6-1 (c), for a strong index modulation grating, one needs to take into account cross-coupling effects in order to fully characterize the optical properties of these multimode fiber Bragg gratings. In the meanwhile, the dependence of the mode coupling on refractive index change for fixed grating length clearly explains why this coupling has not been seen for weaker gratings.

6.2.2 On the Grating Period

The effect of the period of a multimode fiber Bragg grating on its optical properties has also been investigated. The simulations shown in Fig. 6-3 show period-shifted Bragg grating structures. Three different reflection spectra are compared in Figs. 6-3 (a), 6-1 (c) and 6-3 (b), corresponding to three period values, $0.531\mu\text{m}$, $0.533\mu\text{m}$, and $0.535\mu\text{m}$ separately. In these simulations, all the gratings are assumed 10mm in length with a constant index of refraction change over the entire length of the grating.

The additional shaping in the reflected spectra from the initial grating ($\Lambda=0.533\mu\text{m}$) is attributed to the position dependence of the resonance wavelengths. For example, let us first consider the MMF grating with a diminished perturbation period. It is evident that the reflection of the long wavelength side shifted to shorter wavelengths. The interaction between the wave and the grating is similar to the original case, the only difference being the effect of the shift in the resonance wavelength. As the launching modes propagate through the grating, each grating segment that they interact with is slightly different due to the changing grating period. Thus, the frequencies that are reflected vary and since the launching condition is kept

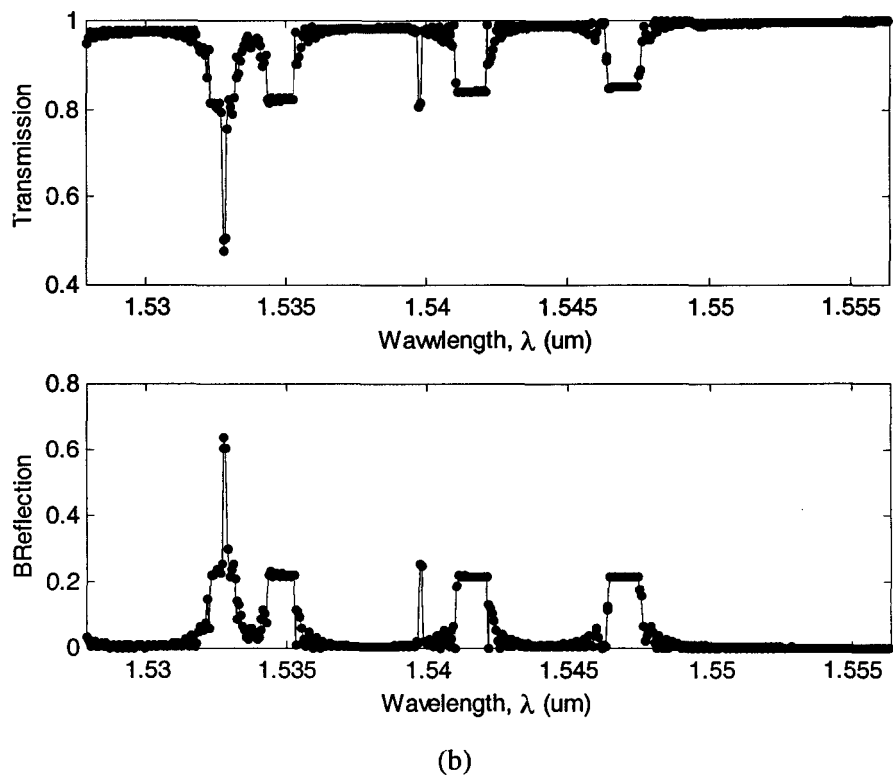
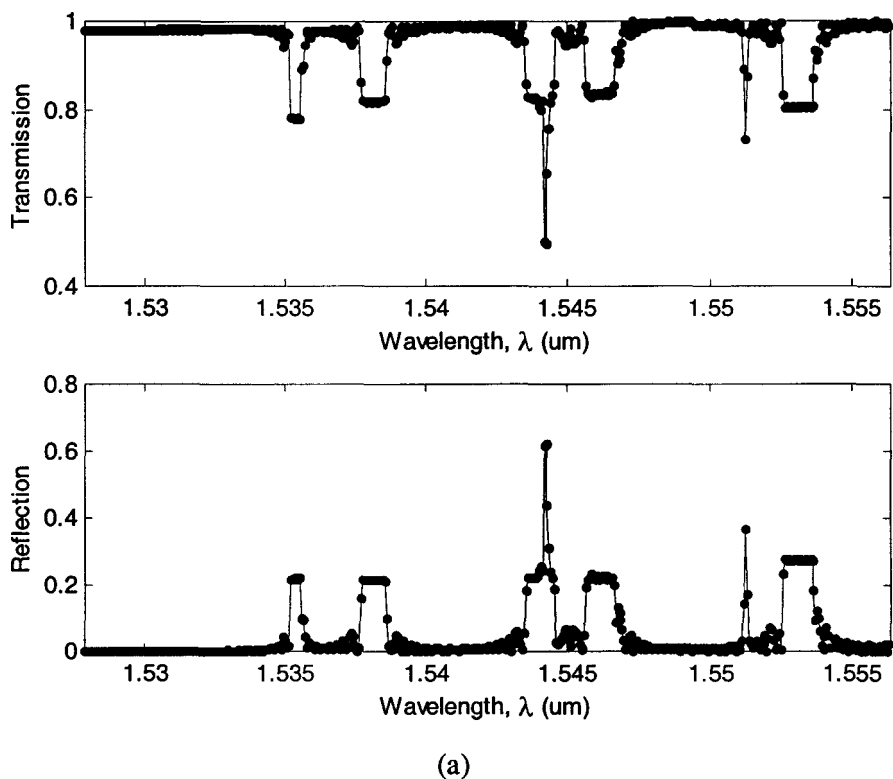


Fig. 6-3 Spectral profile from varying period MMF Bragg gratings for the following period values of (a) $\Lambda = 0.535\mu\text{m}$, and (b) $\Lambda = 0.531\mu\text{m}$ over the 10mm length of the gratings.

the same over this range of frequencies, the reflected signal components will not experience any variation in intensity, and the overall reflected spectrum will have the similar square-like shape depicted in Fig. 6-1 (c). From this interpretation, one would expect that the reflected spectral shape should be independent of the period of the grating. And again, grating interaction from a positive change of the grating period is identical to that from the corresponding negative change of the grating period but with an opposite translation. We can also explain this behavior by considering the phase-matching condition of both the positively and negatively periodic alteration gratings. The displacement for both gratings are “mirror” images of one another. Thus, the response will be the same, except that the positively periodic alteration grating will take place red shift whereas the negatively periodic alteration grating will take place blue shift accordingly. Based on this relationship, we know that a longer grating period Λ is required for Bragg gratings to get the Bragg reflection towards a longer resonance wavelength, and vice versa.

6.2.3 On the Length of the Grating

Grating length is also an important parameter that will influence the performance of the multimode Bragg grating. A set of numerical simulations were performed for the strong grating case when the grating lengths were varied. The index of reflection change is assumed uniform over the grating length. The variation can be seen in Fig. 6-4 by contrast to Fig. 6-3 (a) assuming an unanimous Bragg grating of 10mm in length. Reducing the length of the grating, the peaks in the spectrum responsible for the Bragg reflection switch from the steep rise and fall, square-like shape to the gradual rise and drop-off, smooth and slick appearance, where the cross-coupling reflection vanished, the peak reflectivity decreased, and the bandwidth of the reflection broadened. This variation can be understood in the following way. By shortening the length of the grating, the number of boundaries for reflecting the light is decreased. Therefore, as the wave propagates inside the grating, less of its power is reflected back and coupled to its backward wave. This results in broader bandwidth

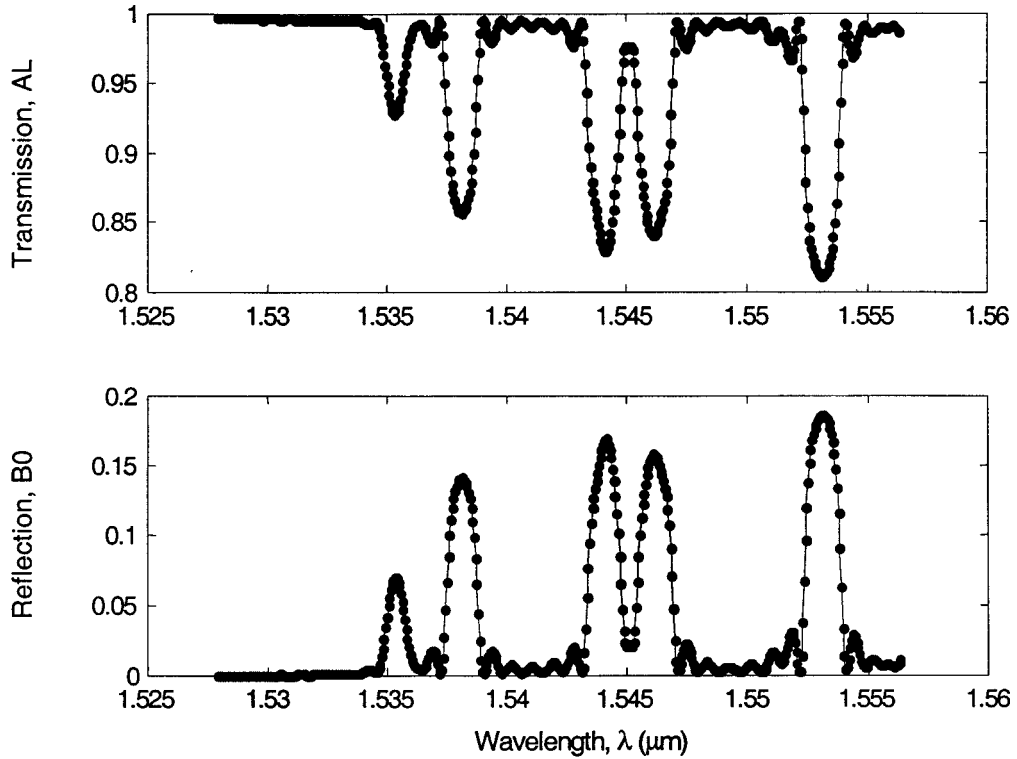


Fig. 6-4 Reflected and transmitted spectra from uniform MMF Bragg grating 1mm in length for comparison with the spectral response of 10mm grating length in Fig. 6-3 (b).

and lower reflectivity. Actually, in principle there exists a weighting factor, $\frac{\nu \bar{\delta}_{neff} L}{\lambda}$,

favorable to evaluate the bandwidth in the reflection spectrum of the grating. Relatively speaking to the “*strong-grating limit*” which has been discussed in Section 6.2.1, it is found a reverse situation said to be “*length-limited*” whose width is an inverse function of the grating length. It is apparent that the weighting factor stands in between, the bandwidth will have bearing on both length and the induced index change.

Subsequently, this set of graphs also tell us that the strength of the reflection from two contra-directional modes at Bragg wavelength is determined by coupling coefficient and the length of the grating, namely, KL , rather than either of them. According to this relationship, theoretically, Bragg gratings may be constructed with

a maximum reflection by either increasing the grating length or enhancing the change of the index of refraction. However, in practice, such devices are not easy to manufacture. Currently, typical values for the index change are ranging between 10^{-6} to 10^{-3} , dependent on the UV-exposure and the dopants in the fiber. An index change as high as 10^{-2} may be obtained by using more sophisticated and much costly techniques. On the other hand, the error associated with the spacing between the periods of a grating (during manufacturing) is cumulative, therefore, with increasing grating length, the total error will increase, resulting in out-of-phase periods (leading to broadening of the Bragg grating). Furthermore, even if a long perfect Bragg grating is constructed, the effects of the environment have to be considered very carefully. For example, any strain or temperature fluctuations on any part of the grating will cause the periods to move out of phase, resulting in broadening the spectral responses of the Bragg grating [4]. Ultimately, to obtain an optical spectral performance of MMFBGs with desired reflection peak and bandwidth, it is a prerequisite to have both the choice of K and L a thoughtful and comprehensive consideration.

So far, we have examined the effects of several important parameters all associated with grating structure. The following we will highlight the effects of structural property of optical fibre and excitation condition of propagation mode on multimode gratings spectra.

6.2.4 On the Mode Excitation Condition

This section will be concerned with presenting a set of numerical simulations of MMF reflection gratings based on different excitation conditions. For the present simulation we choose a both transversally and longitudinally uniform, strong grating in a standard graded index MMF structure. The physical parameters were stated in Table 6-3. It supports 30 linear polarization modes to guide in the fibre core. Three reflection response characteristics under three varieties of the excitation of modal power distribution were calculated and are illustrated in Fig. 6-5. As can be seen,

excitation situations differentiated between completely identical fibre gratings give existence to a serious variation in the spectral response.

The first plot Fig. 6-5 (a) is the reflection response of the strong MMFBG assuming single-mode/multimode fibre launch. In this arrangement merely symmetric modes were excited and assigned optical power. The reflected signal also primarily comprises only few main reflection peaks. By examining the spectrum in each of the reflected components, we find that the prevalent reflection peak consists of the lowest

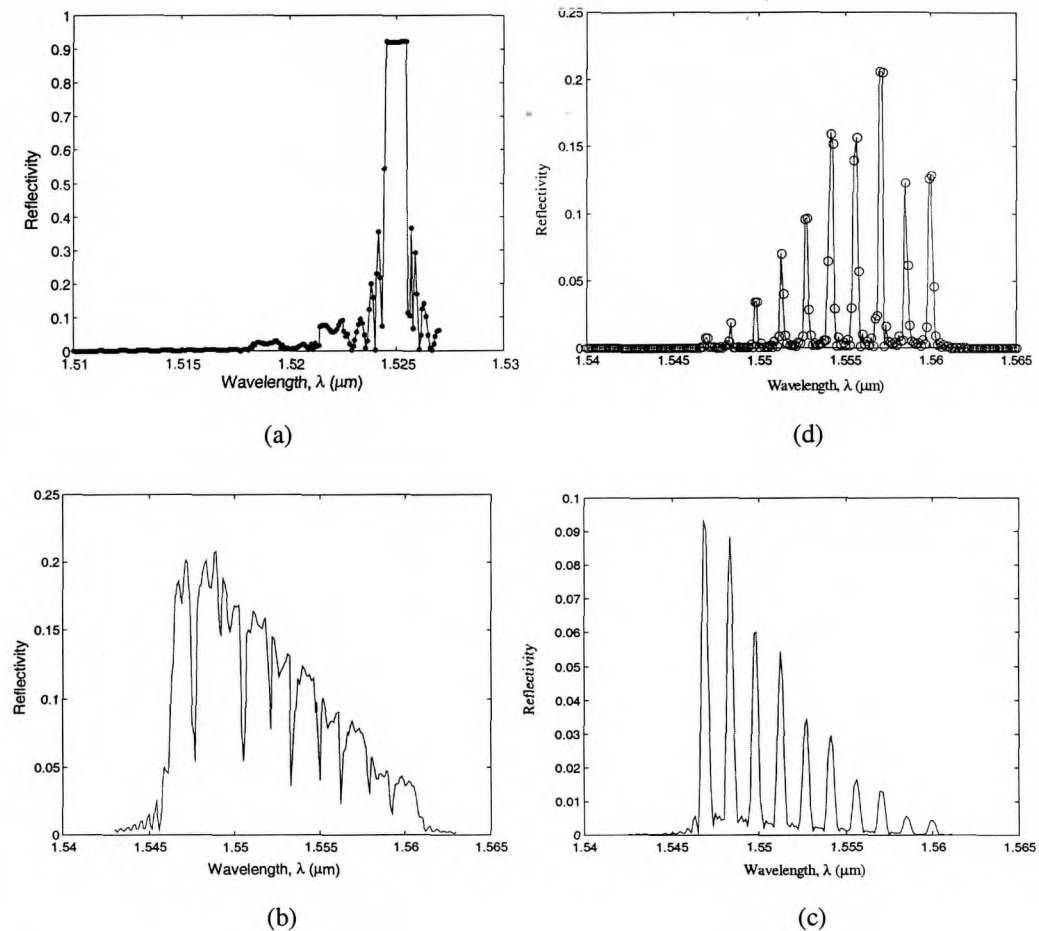


Fig. 6-5 Calculated grating reflectivity spectra in graded-index MMF under three different excitation conditions. Plots are modes for fairly strong grating of (a) single-mode/multimode fibre launch, (b) equal mode population distribution, and (c) equal MPD excitation for a weak Bragg grating, (d) Gaussian mode population excitation. The accompanying sidelobe structure may be viewed as a “Fabry-Perot” effect.

order core mode LP_{01} while the lateral principal peaks in a subordinate place are successively composed of LP_{02} , LP_{03} in order of away from the fundamental mode. Specifically, the reflection spectrum of such a strong Bragg grating with uniform modulation of the index of refraction is accompanied by a series of pronounced sidelobes at adjacent wavelength. A small sidelobe structure has been noted previously in a significantly weaker grating. It has been pointed out that this can result from a space averaged index change. Thus the structure seen in Fig. 6-5 (a) can be physically understood as a kind of *Fabry-Perot effect*. This physical description can be made more rigorous by an “*effective medium picture*” developed by *Sipe et al.*[70] where the grating is replaced by an effective medium with no grating, but rather a frequency-dependent refractive index as depicted in Fig. 6-6. Qualitatively, in the region outside the bandgap, the boundaries of the uniform grating act like abrupt interfaces and behave as partially reflecting mirrors, whilst the wavelengths into the band stop as a transparent region, thus forming a Fabry-Perot-like cavity. The nulls in the reflection spectrum are analogous to Fabry-Perot resonances. It is very important to minimize and, if possible, eliminate the reflectivity of these sidelobes in devices where high rejection of the nonresonance light is required.

Fig. 6-5 (b) illustrates the grating reflectivity if all modes of the designated MMF are excited independently and optical power is distributed evenly among all modes. Clearly, under equal MPD excitation, it is possible to span a very large spectral area, with a reduction in the maximum reflectivity of the grating, and still further along with a notable feature of the large ripple associated with individual resonances. Each resonance is in fact due to the principal modes of the GRIN fibre [8]. The different ordered modes have different resonance peak positions and the shorter the Bragg wavelength, the higher the principal mode order. On the other hand, this resonance area exhibits a gradual ascending from right side (or descending from left side) growth envelope which is a result of GRIN fibre mode degeneracy. For instance, the mode groupings LP_{03} , LP_{22} , and LP_{41} form a single principal mode in GRIN fibres, and thus, a simplified representation of the total set of guided modes is the set of principal modes with associated multiplicity [7] and the higher the mode order, the

higher the mode degeneracy. Equivalently, with reciprocity relation, the same ordered linear polarized modes are distributed among different principal modes are distributed among different principal modes making contribution to different peaks at each corresponding Bragg wavelength of the principal mode. Eventually, in Fig. 6-5 (b) we see 10 principal modes with higher multiplicity and growing in intensity toward the short wavelength side. The low reflectivity of the grating in GRIN MMF is caused by

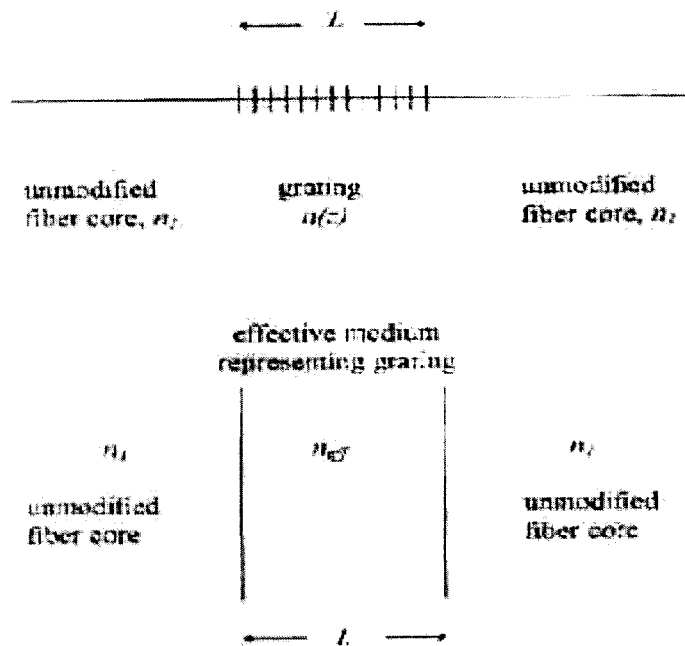


Fig. 6-6 Effective medium picture for a (non)uniform grating (J. E. Sipe and L. Poladian, et al., 1994).

the reduction of the fraction of optical power spreaded among all the guided modes that resonate with the grating at a particular wavelength.

Additionally, the short wavelength features of being introduced characteristic sidelobes originate from Fabry-Perot resonances and the fluctuating peak tops are due to strong modulation of refractive index. If we weaken the grating strength, then we get the result shown in Fig. 6-5 (c). The explanations made in Fig. 6-5 (b) are valid for this one too.

We note that for all of the GRIN MMFBGs discussed here the cross-coupling coefficients, taken an example, LP_{01} - LP_{02} and LP_{02} - LP_{01} , and so forth, are smaller than either the LP_{01} or LP_{02} , etc. self-coupling coefficients by several orders of magnitude. The latter enhances the interaction with identical counter-propagating modes and becomes the dominant interaction in the MMF Bragg grating, while the former diminishes the overlap efficiency between the nonidentical guided modes and turns to be of insignificance. Hence, these cross-coupling coefficients in the reflectivity or transmittivity calculations can be neglected since these contribute little to the growth and decay of the mode amplitudes.

The Gaussian launching grating spectral characteristics was considered last in Fig. 6-5 (d), with the MPD incident on the grating altered to a Gaussian profile. For a given Gaussian excitation condition imposed on a same grating, the reflected spectrum has a similar Gaussian shape as intuitively expected due to the Gaussian nature. A further useful Gaussian profile with which to visualize the impact of launching condition on the performance of MMFBG lightwave reflection and transmission is shown in Fig. 6-7. Here, in order to highlight the Gaussian excitation dependence of the grating response SI multimode fibre with equitable background spectrum (i.e., reference spectrum with equal MPD excitation) was adopted to substitute the GI multimode fibre whose background spectrum is irregular. We can see that the modes involved in the fiber propagating are changing when wavelength is arrived at a very special point. The calculated reflectance and transmittance from three evolution of excited Gaussian profiles referred to as type A to type C (see Fig. 6-7) with their corresponding spectra are shown in Figs. 6-8 (a)–(c), respectively. For both types of gratings with strong and weak index modulations, Gaussian-like responses arise from three types of Gaussian excitations and the spectral responses are evolving along with Gaussian variation.

As may be apparent by now, the operation of a MMFBG is indeed affected by the mode excitation condition intensely.

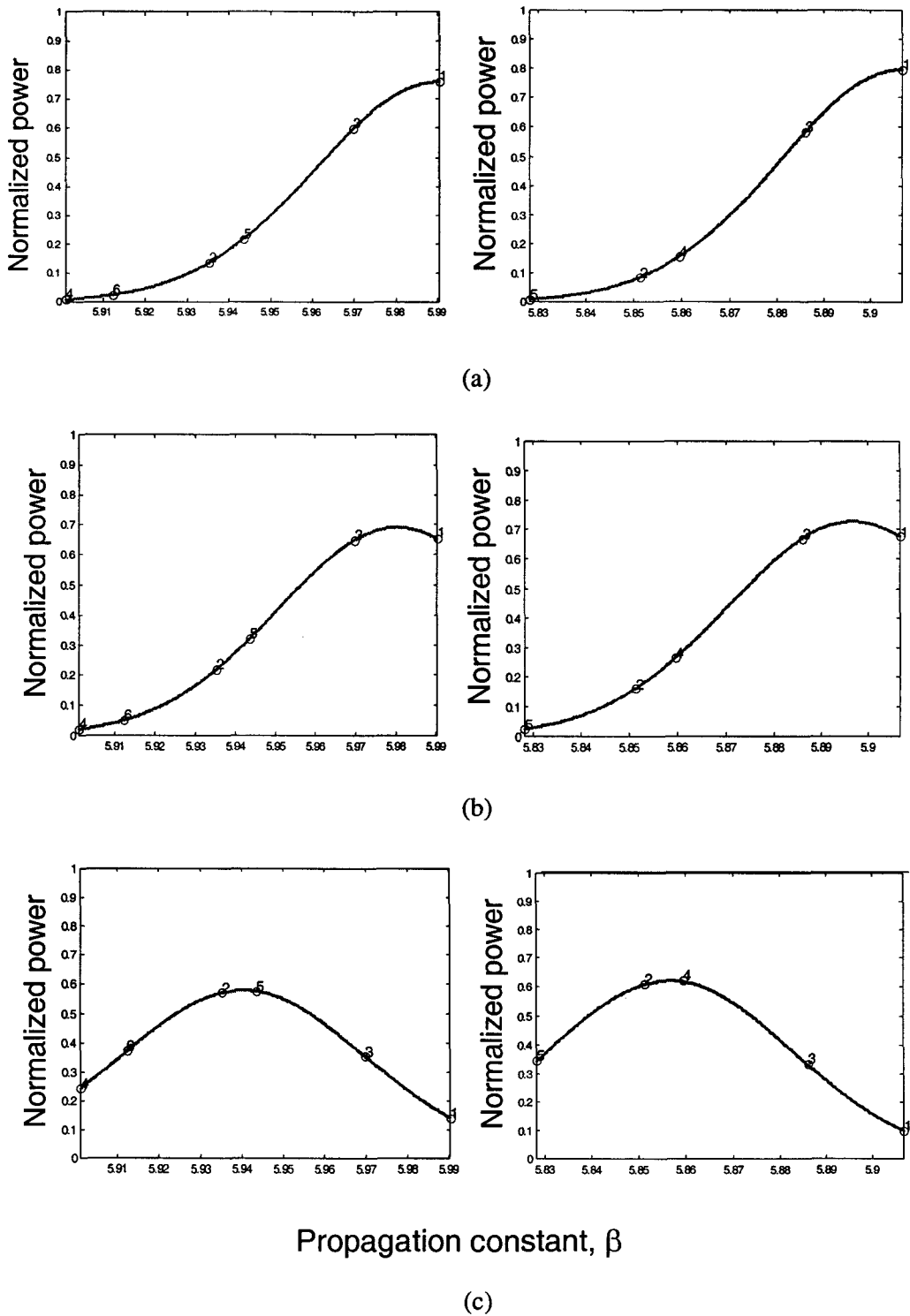


Fig. 6-7 Plots of three types of Gaussian excitation profiles showing the intensity of gaussian distribution evolves from lower order to higher order, with mode changing occurrence.

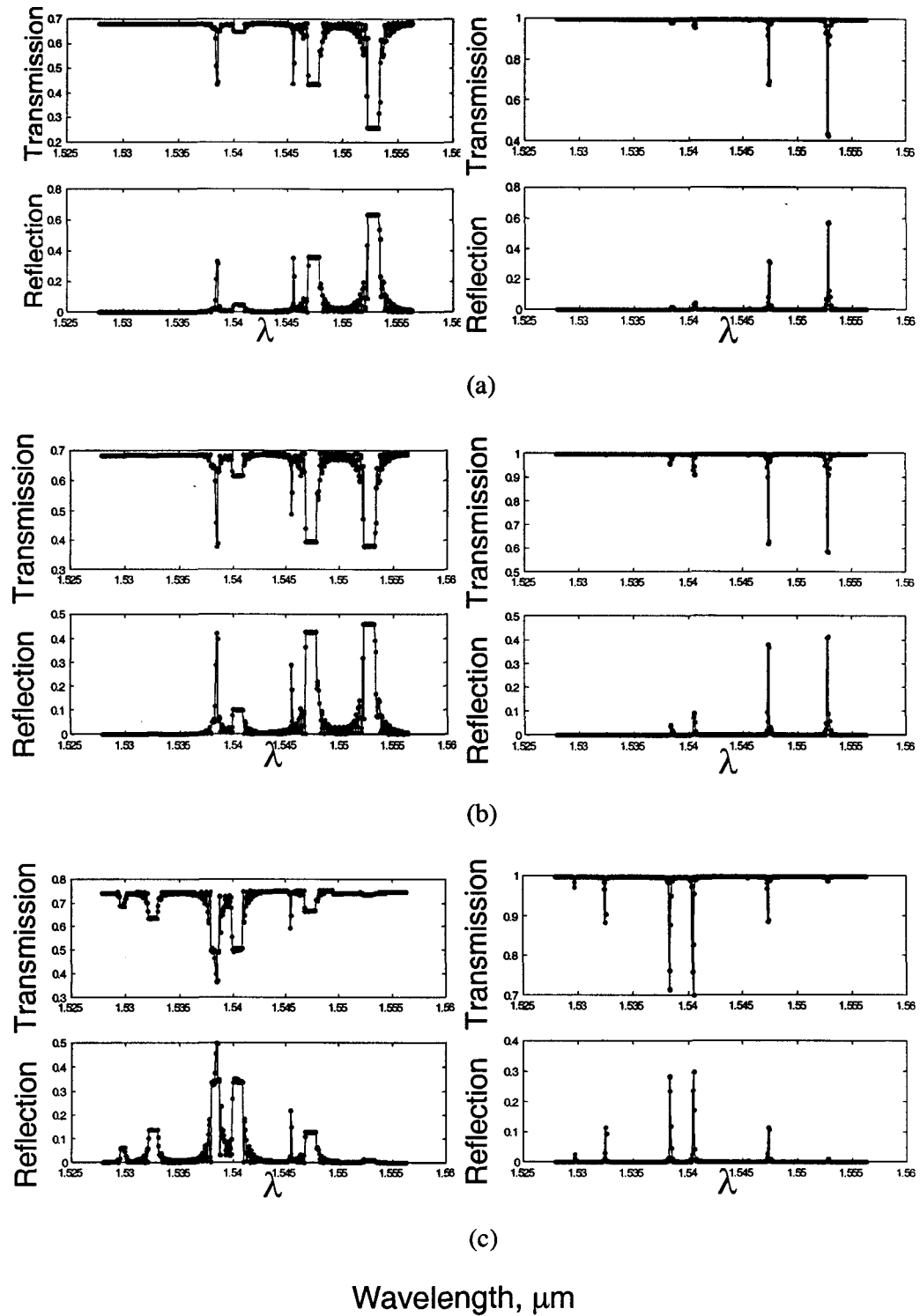
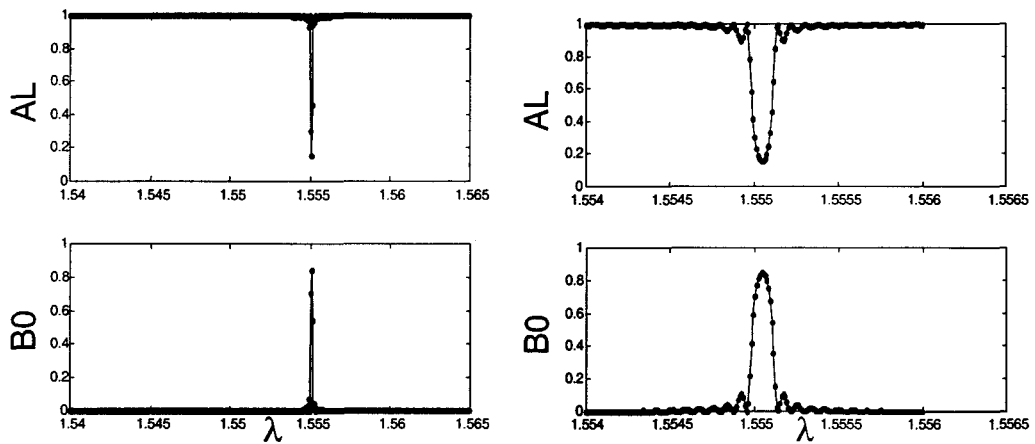


Fig. 6-8 Comparison of transmission and reflection spectra of a Bragg grating in step-index MMF for different Gaussian mode excitation. Here, (a)-(c) spectral response correspond to three type Gaussian profiles appearing in Fig. 6-7 (a)-(c).

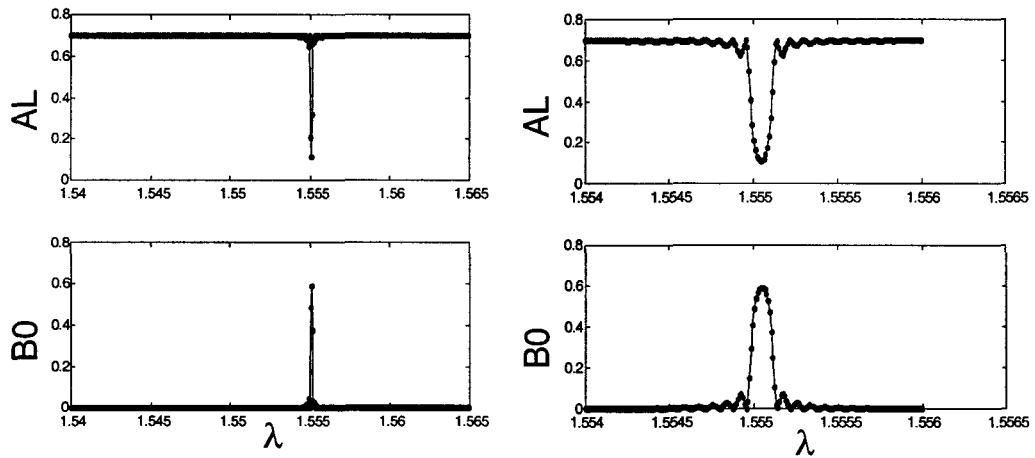
6.2.5 On the Optical Fiber Structure

In this section we focus on the simulation and analysis on the grating spectral characteristics for different fiber structures. The first set of simulations was performed for a SMF structure and an MMF structure. We are going to apply both equalized and Gaussian MPD excitations to SMF and MMF Bragg gratings, and we will discuss what information can be obtained in each case.

In Figs. 6-9 and 6-10 a comparison between a common step-index single-mode fiber grating and a multimode one is presented. There are several interesting features of the plots for this case. The first one is that in figure 6-9 the sine spectrum with only single main grating peak arises mathematically through the Fourier transform of a harmonic signal having finite extent. The side lobes of the resonance are due to multiple reflections to and from opposite ends of the grating region. At the same time, we schematically observed that the multiple peaked spectrum in Fig. 6-10 arises due to the dispersion of the Bragg condition for each mode of the step-index MMF. A second interesting feature of the plots is the fact that the MMFBG spectrum is considerably wider compared to the width of a single peak, which is what a single mode fiber with comparable length and index modulation has to be. The FBG's spectral width is determined by the fiber NA, which is an important parameter connected with fiber structure. Since the numerical aperture is related to the maximum acceptance angle, it is commonly used to describe the light acceptance or gathering capability of a fiber and to determine how many modes a fiber can support. In general, MMFBG width is much larger than a comparable single mode FBG with an exception for single-mode/multimode fiber launch which will be touched later on. It is also interesting to note that for Fig. 6-9 (a)-(b) drawn on the same scale, it has almost an identical shape, but the peak-to-peak amplitude of Fig. 6-9 (a) is descended to that of Fig. 6-9 (b). This is an obvious result from FBG model and the fact that the mechanism of reflection by a Bragg grating in SMF does not depend on the condition of excitation of modes. Besides, the dropoff problem of reflectivity may be overcome by increasing the index of refraction modulation. On the other hand, a comparison of



(a)



(b)

Wavelength, μm

Global view

zoom view

Fig. 6-9 The single mode fiber Bragg grating spectra with (a) equal MPD excitation, and (b) Gaussian profile excitation, indicating the resemblance of the spectral shape under different excitation conditions.

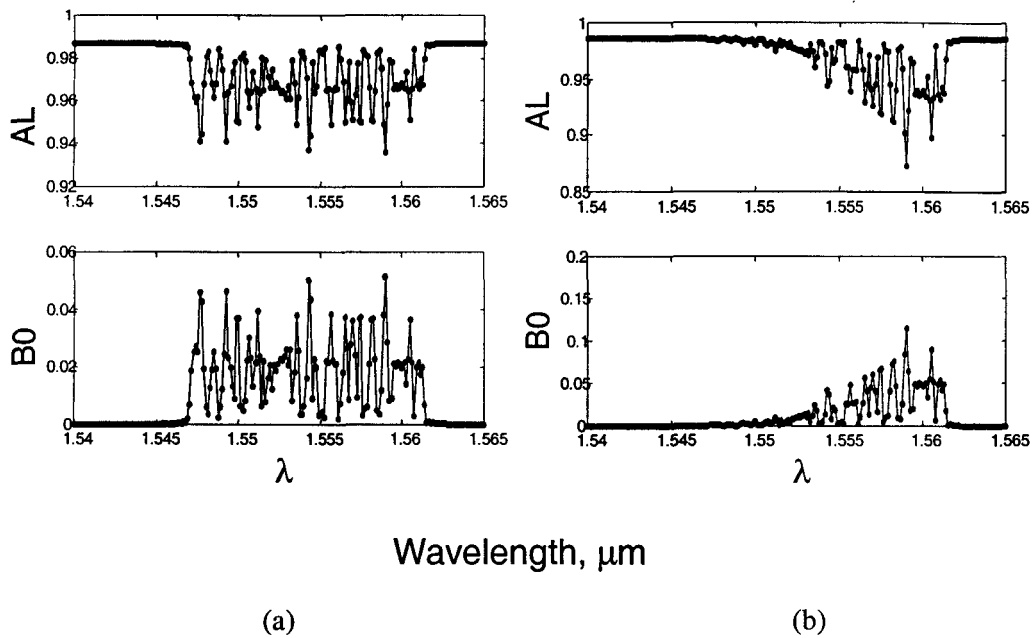


Fig. 6-10 The multimode fiber Bragg grating spectra with (a) equal MPD excitation, and (b) Gaussian profile excitation, indicating the transformation of the spectral shape under different excitation conditions.

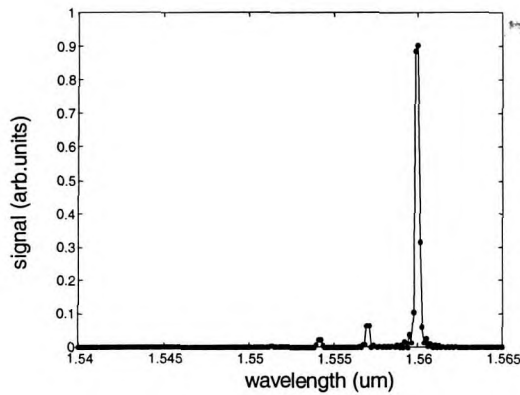
Figs. 6-10 (a) and (b) shows that the spectrum does change in shape drastically when Gaussian excitation was exerted. It is clarified that mode excitation can strongly modify the MMFBG performance causing large change in spectral shape. This feature affords MMFBGs added flexibility in grating design and performance characteristics compared to single mode FBGs.

The dependence of grating spectra upon the fiber structure for the varying index profile MMF was also paid attention to. Here, we examine the spectral response from step-index and standard graded-index MMF gratings with consistent uniform modal population distribution. The plot of Fig. 6-10 (a) calculated for SI-MMF grating structure was compared with that of the previously analyzed GI-MMF structure, referring back to Fig. 6-5 (c). The spectral behavior of the reflectivity can be explained if one examines the relationship between the propagation constant and

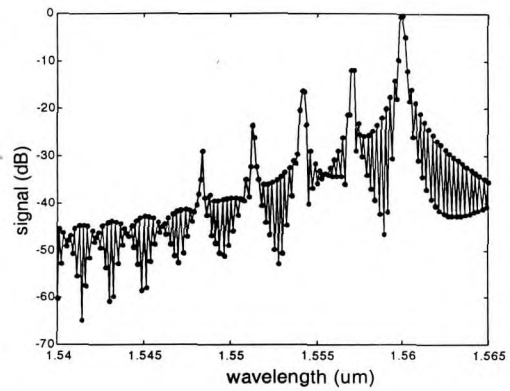
wavelength in each case separately, as shown in both Figs. 3-7 and 3-13. The significant differences in reflection characteristics between SI-MMFBG and GI-MMFBG are primarily owing to their dispersive properties. Modal dispersion occurs in multimode fibers as a result of the differences in the group velocity of the modes. It is much smaller in graded-index fibers than in step-index fiber since the group velocities are equalized and the differences between the delay times of the modes are reduced. This physical picture was nicely elucidated in Sec. 3.2.3 and in Fig. 3-16 that in a graded-index fiber with a higher degeneracy than that in SI fiber, the dispersion compensation effect of light propagation in MMF exhibits much more extraordinary in comparison with conventional step-index fiber. Fig. 6-5 (c) is a typically possible situation of launching or mode mixing in a GI multimode fiber, where the equal MPD is determined from linear polarization mode considerations. From another average point of view, we can readily predict that for the case when each mode power of a mode group is equal, in other words, the mode power distributions are made up in terms of the principal mode number, the resulting Bragg resonances in GI-MMF will be built into an equi-height contour and almost evenly spaced grating spectrum. Again, as one can see, it is advantageous to treat modes having approximately the same group velocity as a mode group.

Subsequently, we examine the reflection responses both from MMF Bragg gratings but with two different fiber index profiles referred to as SI MMF and GI MMF structures. For comparison purpose, in both cases, the excitation condition is set by single-mode/multimode fiber launch. Moreover, the GRIN fiber was assumed to have the same peak core and cladding indexes with SI fiber and a concordant core radius of $25\mu\text{m}$, giving $V = 20.26834$ according to conventional definition of normalized frequency V . A reflection comparison between these two kinds of coupling was made in Fig. 6-11. Figure 6-11 (a) demonstrates the calculated reflection spectrum as a function of the wavelength from GI MMFBG, while, in Fig. 6-11 (b) calculated reflectivity spectrum from SI MMFBG is plotted versus light wavelength. It is evident from the below figures that the GI and SI multimode FBGs

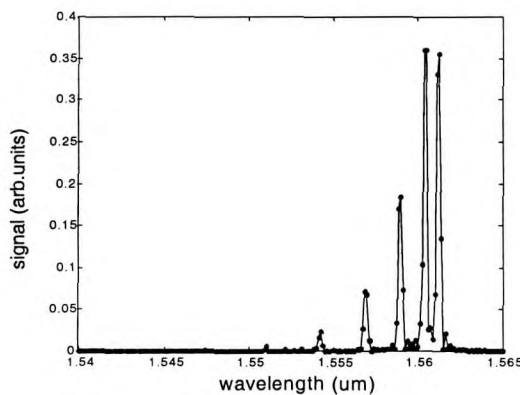
cases behave quite differently. Considering the former first, only one outstanding main peak was observed corresponding to the fundamental mode reflected by the grating and to the back-propagating fundamental mode. The peak second only to this strongest peak is just insignificant, and the further peripheral peaks are almost indistinguishable. When the fibre structure changed, however, there is a notable



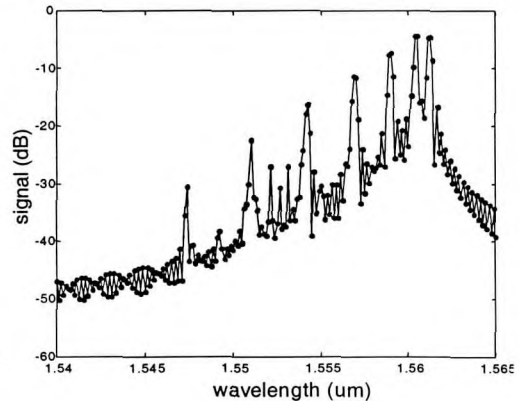
(a)



(a)



(b)



(b)

Fig. 6-11 Reflection spectra under single-mode/multimode fiber launch from (a) parabolic-index profile MMFBG, and (b) step-index profile MMFBG.

Fig. 6-12 Response in decibels from (a) the same MMFBG as Fig. 6-11 (a), and (b) the same MMFBG as Fig. 6-11 (b).

difference in the reflected response between the two profiles: the structure of the reflected spectrum from the SI profile contains considerable more peaks, not present in the GI profile. To examine this difference more closely, in Fig. 6-12 we plot the calculated grating reflection in decibels. The distinguishment between modal peaks is particularly noticeable in the reflectivity spectra by decibel description. This differentiated tendency exhibited in each MMF grating spectrum may be due to the mode power distribution caused by single-mode/multimode launching status.

For understanding such reflection features in multimode fibres, behaviors of modes along a fibre must be clarified. Figures 6-13 (a) and 6-14 (a) show the radial distribution of the electric fields supported in graded-index and step-index multimode fibers respectively. So for our mode coupling system there are 57 linear-polarized modes involved in SI MMF while 30 linear-polarized modes, alternatively, 10 principal modes in GI MMF, as is evident upon examination of mode solution. As a rule, the input wave will interact, at any given regime, only with a fraction of the grating modes with which it overlaps. Under single-mode-to-multimode stimulating circumstances, physically there is a fundamental mode stimulation field whose index profile confined close to the fibre axis, so that at the interfaces between the SMF and MMF only the symmetric guided modes have an appreciable source-to-fibre optical power efficiency factor and were excited. The other higher order modes do not feel the power flow in this case. The result of the power distribution in a parabolic-index optical fiber is illustrated in Fig. 6-13 (b). The ordinate represents the relative intensity normalized to one unit by total energy. It expresses the interaction between modes through the direct change of the optical power. A notable feature of the distribution in GI MMF structure is that as power is launched into successively symmetric modes, the majority of the power is concentrated in the lowest order mode LP_{01} . The remarkable decrease in intensity for higher modes is definitely responsible for the GI MMFBG spectral characteristics. Likewise, when an index profile is step-type, the reflection response should also coincide with its power distribution as well. However, in this case the distribution pattern presented in Fig. 6-14 (b) is much

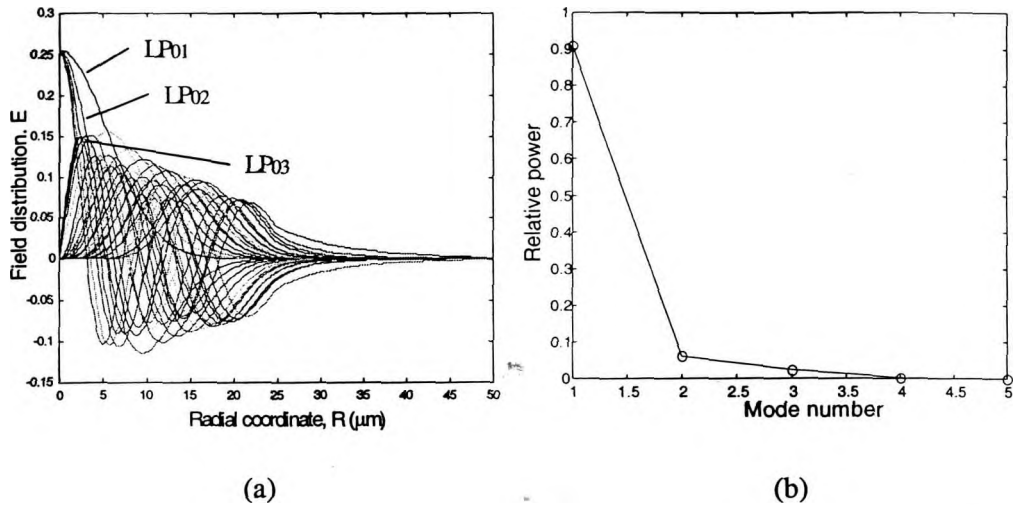


Fig. 6-13 Corresponding excitation characteristics of GI uniform MMFBGs appearing in Figs. 6-11 (a) and 6-12 (a), in which (a) is radial distributions of the electric field amplitude of the core modes in GI MMFBGs, and (b) is the associated mode power distributions as a function of the mode number in GI MMFBGs.

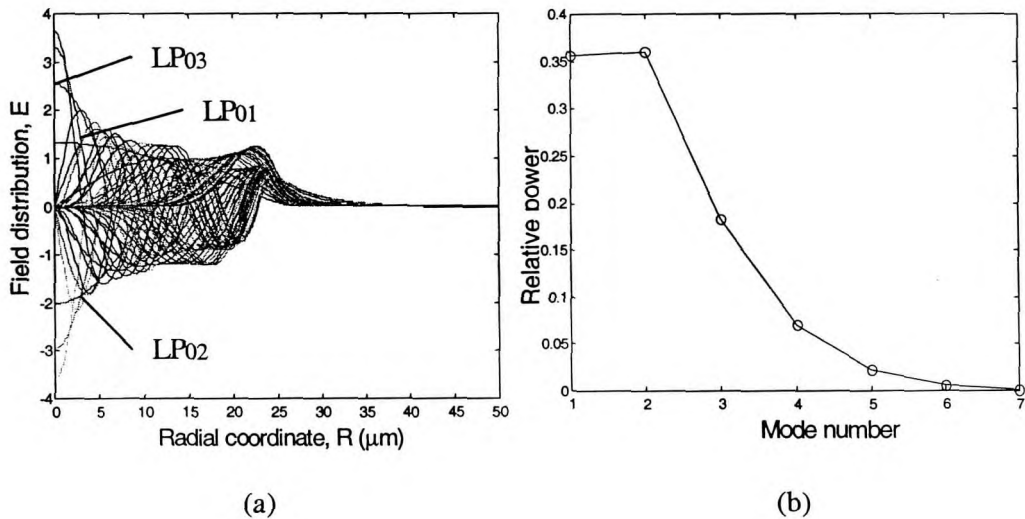


Fig. 6-14 Corresponding excitation characteristics of SI uniform MMFBGs appearing in Figs. 6-11 (b) and 6-12 (b), in which (a) is radial distributions of the electric field amplitude of the core modes in SI MMFBGs, and (b) is the associated mode power distributions as a function of the mode number in SI MMFBGs.

different from the case of Fig. 6-13 (b) due to the parabolic-index profile. For higher mode groups in SI MMF, a gradual decline in the attenuation is observed as mode number increases. This is responsible for the spectral structure of MMFBG with step-type profile modeled and simulated in former Figs. 6-11 (b) and 6-12 (b). Therefore, the different structural properties of multimode fibers associated with mode power determination thus give rise to the considerable differences between the grating responses.

The important point to note in the above analysis is that for higher single-mode/multimode excitation in graded-index MMFBGs, only one principal reflection is dominant and no appreciable higher order reflection was observed. In other words, the reflection property was almost equal to conventional gratings in single mode fibers, suggesting unique potential applications, as a result of which, Fig. 6-11 (a) is of particular interest. In contrast to the case of Bragg reflection from a strong grating, wherein we recall the spectral analysis of GI MMFBG with identical SMF/MMF excitation mode in previous section and plot of Fig. 6-5 (a), the big value of grating depth enhances the interaction with both lower and higher order modes and this also applies equally to sidelobes. According to these results, to obtain a maximum reflection, there would be an expansion in the bandwidth and the number of side lobes. The latter undesired spectral structure can be overcome by apodization. So, apparently, this type grating combined with selective mode launching has strong ability to achieve the goal of enabling optimized performance grating-based devices.

6.3 Summary

This chapter presents a systematically theoretical study on the optical properties of various MMFBGs. The effects of varying grating characteristics (including period, length, index modulation strength), mode excitation conditions and fiber-optic structures on MMFBG device performance have been simulated and analyzed by directly applying our own well-established MMFBGs simulation software package.

To our knowledge, this is the first detailed analysis and systematical investigations on optical response from multimode fiber Bragg gratings.

Although the performed numerical simulations to determine the transmission and reflection is straightforward, one would also like to achieve some general physical insight into the dynamics of the spectra in order to predict the spectrum response without a detailed calculation. This will also provide insight into the design of more complicated grating structures.

Thus, qualitative conclusions based on the throughout preceding physical modeling and computer simulations are summarized as follows:

1. As gratings get stronger, the reflection (or transmission) responses are shown to experience considerable broadening and modifications in the spectral shape. In this case, it is crucial to take into account the mode cross coupling effect for it plays an important role in the optical characterization of multimode FBGs.

2. An improvement of the reflectivity can be achieved by enlarging both the refractive index modulation strength and the length of grating zone. However, the increase on index modulation leads to a widening of the wavelength region of the reflectivity central maximum. The enlargement of the length of grating results in a narrower and steeper central maximum of each peak modal reflectivity.

3. A movement of the reflection, either red shift or blue shift, can be achieved by variation of the grating period. Even a slightly small change in period value can alter grating peaks position visibly. It indicates that Bragg reflection wavelength is highly susceptible to grating periods.

4. The spectral properties of Bragg gratings in multimode optical fibers strongly depend on excitation conditions of propagating modes. The number of reflection peaks and the modal reflectivities are tightly related to mode excitation situation. Specifically, for standard graded-index multimode fiber, these distinctions result in distinct results when analyzing the transmission or reflection of a MMFBG. Such results are of potential significance in sensor applications.

5. The calculated spectra for fiber Bragg gratings show a substantially spectrum dependence on the physical structure of fibers. Two interesting points may be noted. On one hand, with respect to the spectral shape, a distinguishing quality of SMFBGs from MMFBGs, reversely whose spectral shape is serious influenced by excitation mood, is that the launching condition does not affect the reflected signal shape. On the other hand, in terms of MMF structure, graded-index types are provided with obvious better spectral performance than step-index types. Typically, under SMF/MMF mode excitation, the reflectivity of graded-index MMFBG almost amounts to conventional single mode fiber gratings. This is an unique and novel property which could lead to a range of new concept and applications.

Our theoretical simulation results described above not only allows us to deeply comprehend and clearly visualize the sophisticated interactions within a multimode fiber grating, and will also allow us to confidently predict and rationally evaluate the behavior of more complex grating structures. This new investigation is already proving to be useful in device design and making us believe that there is great potential in the development of novel devices and applications based on good performance MMFBGs.

CHAPTER SEVEN: CONCLUSIONS

In this chapter we will summarize the previous works with a special emphasize on the results. We will also try to briefly draw lines into the future.

7.1 Thesis Summary and Conclusions

Fiber Bragg gratings (FBGs) have emerged as important components and received intensive research attention in both fiber telecommunication and sensing fields. Bragg gratings in single mode fiber structure (SMFBGs) have been studied extensively. On the other hand, fewer studies have been reported on multimode fiber Bragg gratings (MMFBGs) despite of their potential applications in future optical access networks. In addition, the adaptability of present theoretical studies are restricted to either very special cases or solely self-mode coupling gratings. Thus, a generalized theoretical derivation and a complete numerical implementation, which can account for arbitrary couplings for multimode gratings, are necessary for a precise and quantitative study of MMFBGs.

Motivated by the lack of such a study, we carried out our thesis research work on Bragg gratings in optical fibers in multimode propagation both theoretically and experimentally. This work successfully accomplished mathematical-physical models covering mode solver, mode excitation simulator, and grating solver three main parts and further developed the numerical softwares corresponding to these three aspects, and ultimately, integrated them into a complete software package, namely, MMFBG simulator. This applies to simulate and analyze the experimentally investigated results. Overall, our simulation and theoretical modeling work explain the experiments very well. Furthermore, the physical effect of grating characteristics, excitation conditions and fiber structures on FBG optical properties in single-mode, few-mode and

multimode propagations were explored in detail and sublimated systematically.

This thesis contains seven chapters in total. Apart from Chapter 1, 2, and 7 dealt with introduction and summary, the other Chapters 3, 4,5 and 6 are all key contents of this work, among which, the former Chapters 3 and 4 are devoted to the theoretical models development and numerical softwares implementation, and the latter Chapters 5 and 6 are contributed to practical applications of MMFBGs model and simulator in both experimental and theoretical respects. In each chapter, we all made a careful and thorough research as well as analytic and illuminating discussion with physical significance. Many of our investigations are first undertaken and most of the results have not been reported to date in the literature. More concretely, we summarize the main achievements of this thesis as follows.

In respect of fundamental theory and mathematical-physical model establishment

A straightforward theory has been presented that can accurately model the transmission and reflection through varieties of fiber gratings that exhibit substantial mode coupling. There are two parts to the theory. The first is the multiplex modal analysis. The second part of the theory is the multimode coupled-mode theory. We focus on the detailed derivation of the coupled-mode theory formulations for Bragg gratings for MMF. The principles we developed here are general for various applications, even though the expressions for specific problems may need to be changed. Through this derivation, we can get a theoretical understanding about MMFBGs mechanism from both physical sense and mathematical framework. This forms the basis of our whole thesis work.

1. Modes and fields: We begin with Maxwell's electromagnetic equations and study the modal properties of the scalar wave equation. Since we are interested mainly in low Δ fibers, where $\Delta = (n_1 - n_2)/n_1$ is the normalized core-cladding index

difference, linearly polarized (LP) approximation should be sufficient to describe a mode guided by the fiber core. We use this description to find, analyze and compare the mode propagation characteristics between step index fiber and graded index fiber. It is concluded with advantageous dispersion property of GI over that of SI. This superiority will impact and benefit the grating spectrum performance physically.

2. Multimode coupled-mode theory: The fiber grating characteristics can be understood and modeled by several approaches. Coupled-mode theory is often the foundation for many of these computations. The coupled-mode theory formalism for both two possible categories of multimode fiber Bragg grating, independent mode and mode coupling, are considered and derived precisely. Explicit expressions for the coupling coefficients, which play a central role in this theory, are also formulated. An important dynamic quality factor Q has been proposed for characterization of their fiber gratings. It is thus worthwhile to pause and consider some of the basic properties of Q factor:

- (1) The most useful feature of Q factor is the ability to readily visualize an arbitrary mode coupling strength at any given wavelength.
- (2) This allows us to explicitly examine and study the dynamics of the sophisticated grating behavior. So, it is particularly meaningful for multimode interaction FBG structures.

Based on the developed physical modal, we can deal with diverse complex situations. These coupled mode equations not only have the generality to the MMF Bragg grating problem, but also have the flexibility for some specific issues.

3. Technical background review: In addition, a relatively thorough introduction of the field of fiber Bragg gratings is reviewed and offers us a summary of the theoretical concepts on which integrated and fiber optical gratings is based. We will find helpful definitions and a number of important formulas we commonly encountered independent of the specific application. This technical background not

only served as a good starting point and solid base board, but also depicted a clear backdrop blueprint for our research carry-out.

In respect of numerical methods and software development

A series of numerical methods were studied and employed to realize individual programming and comprehensive treatment for MMFBGs problem. Our developed MMFBGs software tool that integrates mode solver, grating solver, and excitation simulator three subroutine can make the design process more efficient, cheaper, and faster.

4. Applied numerical methods: We scrutinized and chosen the feasible methods used for root searching of all lower- and higher-order core modes in both typical step-index optical fibers and graded-index fibers. Also, we intensively delved into the methods dealt with initial condition and boundary condition problems. These include bracketing method, bisection method, Runge-Kutta method, shooting method and Newton-Raphson method. Although these methods are already existed in mathematics, particular implementation and deliberately combining them together in algorithm to treat such a sophisticated problem as MMFBGs problem (Note that the sets of Eqs. (4.56)-(4.57) and (4.58) and (4.63) each describe a large number, typically several-hundred, of coupled first-order differential equations) is still fairly challenging and highly valuable.

5. Numerical implementation and programming: Based on our MMFBG theoretical model and utilizing the above numerical techniques, we succeeded in developing individual software, i.e., fiber optical mode solver, fiber optical grating solver, and mode excitation condition simulator three units in MMF structure.

(1) The mode solver is used to calculate SI and GI modes, the associated propagation constants and mode field profiles, and the coupling coefficients.

- (2) The grating solver is more general and requires only the propagation constants and coupling coefficients associated with the fiber modes. Such numerical treatments are based on solving coupled mode equations that describe the interaction of guided light modes. In practice the difficulty of solving the coupled-mode equations lies in the strength and the spectral density of the resonances.
- (3) The excitation simulator is capable of determining the mode power distribution of excited modes inside the multimode fiber grating, such as average excitation, Gaussian excitation and single-mode/multimode fiber launch conditions.

6. Software integration and testification: The mode solver, grating solver and excitation simulator were further integrated by appropriate numerical methodology and computational algorithm into a complete software package, that is MMFBGs simulator, and applied to model and simulate the measured spectrum responses from a number of practical MMFBGs encountered in a wide range of experimental situations. It should be pointed out that insofar there already are very few simulation products for MMFBGs. However, they all have some obvious limitations mainly in two cases. First, one case can deal with MMFBGs no matter how many modes involved, but is restricted to self-coupling for uniform fiber gratings. Second, the other case take the cross coupling into account but with restriction to two-mode coupling calculation, which will definitely lead to the following disadvantages:

- a. theoretically speaking, it can work on cross-coupling problems; but the coupled modes have to be selected by the user himself via editing mode parameters. That is to say, it does not have the ability of insight the complex mode interactions in grating fiber automatically.
- b. in theory, it can process multimode FBGs; however the multimode is restricted to no more than two modes at a time and hence the so called MMFBG spectra it outputs is displayed one by one in every separate window,

which results in high complexity and low efficiency in dealing with more than ten modes (in effect, when coping with five or six modes, it already becomes quite harder. So strictly speaking, it only can manage few modes problem.). That means, it does not possess the capability of calculation the fiber gratings in real multimode structures simultaneously.

In contrast to the existing approaches, our MMFBGs simulator developed in this thesis seems to offer the best advantages as of now also primarily in two aspects:

- (1) First, our MMFBGs simulator can handle not only self-coupling but also cross-coupling for any complicated mode interactions in FBGs automatically.
- (2) Second, our MMFBGs simulator can effectively solve FBG's problem in single mode, few mode and as well as multimode fiber structures, in which an arbitrary large number of fiber grating modes is permitted, i.e., the number of modes has no limitation, for example, we have usually settled hundreds modes simultaneously in MMFBGs.

The above most significant advantages over the extant apparently constitute the exclusive novelty of our MMFBGs simulator. These new features, complied with the modal validation and experimental verification, sufficiently ensure that our MMFBGs software can excel as a powerful and reliable computer-aided simulation and modeling tool for designing and analyzing the optical fiber devices based on Bragg gratings.

In respect of experimental research and theoretical deployment

The transmission and reflection of multimodes guided by the core of an optical fiber through an ultraviolet-induced fiber grating when substantial coupling occurs is analyzed both experimentally and theoretically, adopting the apparently novel numerical model developed, implemented and validated in this thesis for the study of the behavior of MMFBGs. In this part, MMFBG physical modeling and spectral response computational simulation results are presented for the first time.

7. MMFBG characteristics are studied experimentally.

It is found that the spectra of MMFBGs depend strongly on fabrication conditions (e.g. modulation depth of the grating) and experimental conditions (e.g. mode excitation). Good agreement is obtained between the theoretical simulations and experimental measurements. Our simulations based on the developed MMFBG numerical model can provide quantitative explanations for the observed experimental phenomena. These explanations give a complete understanding of the nature of the interaction between the wave propagation and multimode fiber gratings.

8. MMFBG characteristics are also studied theoretically.

The optical properties (in terms of both transmission and reflection) of gratings that support multimode counter-propagating interactions are accurately modeled and simulated under various physical conditions by means of our developed MMFBGs simulator. Finding such a characteristic relationship between spectra and physical parameters is important because it will enable us to predict the possible performance and exploitations with the increased complexity of fiber optic components and networks assisted by MMFBGs. From another point of view, the results presented here, some important part of which have been identified through experimental evaluations, meantime confirm and complement our previous experimental study of multimode fiber gratings. It is considered that spectral simulations provide operating principles and basic criteria in design MMFBG-based devices. It can help find optimized grating parameters to meet the application requirements. Therefore, it possesses profound significance as a theoretical guidance to practical applications.

9. Principal results have been obtained for the characterization of optical properties for MMFBGs.

Various simulation results and spectral characteristics have been analyzed under both ideal and actual conditions. Theoretical and experimental investigations

unanimously certified that:

(1) The optical characteristics of MMFBGs are determined by four grating parameters: the magnitude of the perturbation in the refractive index, the photosensitivity profile of the grating, the period of fiber grating, and its length.

- a. The magnitude of refractive index perturbation and grating length in the main greatly influence reflectance and bandwidth. (The reflectivity increases as the induced index of refraction change increases. Similarly, as the length of the grating increases so does the resultant reflectivity. Meanwhile, the reflection bandwidth increases as the refractive index modulation intensity increases. Contrarily, the increase on grating length decreases the bandwidth of fiber gratings.)
- b. The period of the grating, on the other hand, decides the center wavelength. (With the increase of the period parameter, Bragg wavelength of reflection spectrum occurs red shift, while the decrease of grating period leads to the spectrum taking place blue shift.)
- c. It is also possible, for a strongly reflecting grating with a large index change, not only to produce more prominent cross-coupling effect due to longitudinal perturbation, but also to induce more complex nonuniform grating profile in transversal direction. Such photosensitivity profile will affect on gratings index modulation, which in turn will change the mode coupling efficiency and make important impact on spectral properties.

(2) The optical characteristics of MMFBGs are also determined by both physical structures of fibers and mode excitation conditions.

- a. On one hand, SMFBGs are provided with strong shaping maintenance function compared with multimode FBG, for there are additional modifications in the shapes of the MMFBG spectra when excitation conditions are altered.
- b. On the other hand, MMFBGs offer added flexibility in grating response may be turned by the spatial periodicity length, core size, numerical aperture, index profile, and mode coupling characteristics of the grating. Specifically,

GI-MMFBG has much better ability to closely behave as a SMFBG performance compare to SI-MMFBG by properly design, because the dispersion effect of graded-index fiber is much lower than that of step-index fiber.

- c. Furthermore, the effect of mode excitation has a relatively decisive impact on grating spectral characteristics. For example, high multimode excitation results in more multiple peaks and a wider spectrum of MMFBG reflected response that occurs for the lower-order mode excitation. It is further brought to light via this work that combining different excitation conditions with appropriate MMF grating structure provides great flexibility in designing functional grating-based optical devices.

On the whole, the MMFBG spectral response took on significantly different shapes under various conditions. In principle, it should be possible to generate arbitrary spectral shapes by approximately tailoring the grating characteristics, mode excitation and fiber structures. One can clearly see that the Bragg grating characteristics, mode excitation conditions and fiber physical structures three major aspects play an important role in determining MMFBG spectral characteristics, and as a result, become most active areas of research and development in the fiber Bragg gratings field today in view of both theoretical and experimental points. The fact suggests that these three respects are also the direction of our future research. Up to this point, we will further discuss in the following.

7.2 Future Work and Suggestions

This thesis is mainly a study of both theoretical and experimental issues in the field of multimode fiber Bragg gratings. The numerical model and optical characteristics of MMFBGs are investigated in detail. Overall, our work in this thesis has gained successful achievements. However, because of time and some conditions limited, it is impossible to cover more massive topic emerged in this field in a thesis

of this size. Hence, in concise we put in a nutshell here a few future work suggestions. A list of technical references is provided as well, to allow the interested reader to seek out specific topic in more detail.

Based on our work, this research can move forward in several directions.

1. Concerning software work suggestions

There are several aspects can be further committed to refining and extending our software to improve the overall functionality and applicability. Further investigations include:

(1) grating type: Apart from the most commonly encountered uniform Bragg gratings, which we have studied thoroughly in this thesis, there are some other special grating types such as chirped gratings, blazed gratings, phase-shifted gratings, and superimposed multiple gratings [4, 27]. These fiber Bragg gratings are distinguished either by their grating pitch (spacing between grating planes) or tilt (angle between grating planes and fiber axis). From the coupled mode equations, we know that the refractive index modulation type in the core region of fiber decides the spectrum characteristics of fiber gratings. Therefore, supplement of these distinct types will enable our software to be adaptable to any type of grating.

(2) output function: In the present work we put the most attention on the reflectivity and transmission of the fiber grating, However, in the results of the calculations we obtain the complex values of input, transmitted and reflected waves. Therefore, our method makes it possible to define the phase characteristics of a fibre grating such as dispersion and group delay [27] too so that one can characterize the grating performance in more ways.

(3) cladding and radiation-mode coupling: Bragg grating written in highly photosensitive fiber, such as, fiber which has been hydrogenated, have a very pronounced transmission structure on the short-wavelength side of the Bragg peak. This feature is only observable in the transmission spectrum (viewed in reflection,

only the main peak appears), therefore, this structure must be due to light leaving the fiber from the side, and to analyze it one must take it into account cladding-mode and radiation-mode coupling. Especially, the cladding and radiation-related problems become very serious with large excess losses at wavelengths shorter than the peak reflection wavelength. Consequently, exploring coupling from a core mode to cladding and radiation modes may be the possible subject of future investigations. More detailed descriptions on the effect of this type of interaction can be found in [4, 31, 71, 72].

2. Concerning experimental research suggestions

It is announced from the results of our work that considerable effort should be directed at modifying the multimode fiber grating structure and mode excitation condition to improve or specialize the MMFBG spectral characteristics. Accordingly, experiments are expected to proceed to further steps as follows:

(1) fiber grating structure: One of the exciting fields wherein MMFBG is expected to proceed a great revolution is structures and smart intelligent systems of interest. As a typical example, a novel fiber structure consisting of concentric shells of alternating high and low refractive index has been designed in [7] with the goal of enabling narrow-band high-reflectivity grating to be written in multimode fiber. It has been shown that modal effective index degeneracy is required for narrow-band grating operation. This is almost consistent with the investigation conclusion in our theoretical work.

(2) mode excitation condition: Structural design of fiber is undoubtedly promising and fascinating and becomes one interested direction for people to pursue. Nevertheless, the fiber grating structure is usually related with some detailed problems of fabrication techniques, so quantities of interest are to propose, implement and measure the various physical configuration of excitation condition of mode propagation [8, 73-77]. In practice, the mode excitation has determinant impact on the performance of MMFBG lightwave transmission and reflection. The research on

mode excitation condition will be very meaningful and valuable.

(3) material photosensitivity characteristics: At first, the observation of photo-induced refractivity in fibers was only a scientific curiosity, but over time it has become the basis for a technology that now has an important role in optical communications and sensor systems. Furthermore, this technology could be extended to more other types of applications with the discovery of large photosensitivity in different material systems. Evidently, material photosensitivity characteristics is a necessary step to be pursued. Although fiber photosensitivity was observed more than 20 years ago, its physical explanation and mechanism are not clear yet due to the physical complication and shortage of enough and detailed experimental data. A great deal of research has been directed in either underlying mechanism or the laboratory surveys and its uses is on-going in many universities and industries [78-82]. Despite the apparent experimental and theoretical difficulties in investigating photosensitivity, there might very well be enticing reasons for pursuing it.

3. Concerning application exploitation suggestions

MMFBG has a broad range of potential applications. The most promising applications are in the fields of lightwave communications and optical fiber sensors.

(1) Telecom: Bragg gratings in MMF will be useful for spectral control of a laser having a relatively large beam diameter and difficult to couple with SMF. For instance, a solid state laser, such as Cr^{3+} : LiSrAlF_6 laser and Ti^{3+} : Al_2O_3 laser [15], is difficult to couple with SMF, and therefore it can be a candidate to be tuned with a Bragg grating in MMF. Another laser tuned with a MMFBG will be a semiconductor laser. Especially, a vertical-cavity surface-emitting laser (VCSEL) for optical communication has a large emitting area and therefore is suitable for coupling with MMF [8].

(2) Sensor: Bragg gratings in multimode fibers can be used for bending or displacement sensors. The sensing applications were proposed by *Wanser et al.*[12]. Micro-bending was used to disturb the mode population in an optical fiber via mode

coupling before passing the light to MMFBG. As a result, when MMF with a Bragg grating is bent, the reflection and transmission spectra change. Some of the other characteristics of bending sensors are reported in [83]. Also, a displacement sensor is possible by translating the displacement into bending using a deformer [8, 84]. In addition, a new proposed MMFBGs based fiber optic sensor can be utilized for fiber optic sensing of strain and temperature, and may be further for sensing of many other physical parameters such as pressure, and flow-rate [11].

(3) Hot topics currently: As mentioned just now, the novel concentric shell fiber in [7] may find application wherever a large coupling area for light collection and narrow-band filtering are required simultaneously. Two such applications are local area networks (LANs) employing multimode fiber and collection fibers with intrafiber filtering for *in vivo* Raman spectroscopy. Recently, a wavelength locking scheme based on fiber Bragg grating was demonstrated [85]. When the laser operates in the scheme, its wavelength is locked with the reflection spectra of the fiber grating. This results in two effects: reduction of the wavelength chirp and increase of the extinction ratio. The FBG application in a wavelength locking mechanism can surmount direct modulation technique for semiconductor lasers and provide stable wavelength necessary for dense wavelength-division multiplexing (DWDM) system applications.

The above list is far from complete and in fact, the applications and possibilities in designs of new fiber grating structures and explorations of efficient mode excitation conditions are seemingly endless and continually attract considerable research interest. The ability to make so wide applications of MMFBGs assures their long viability as components in advanced systems research and provide good performance in the practical system.

In conclusion, advantages of multimode fiber Bragg gratings over competing technologies include all-fiber geometry, low insertion loss, high return loss or extinction, potentially low cost, and the flexibility for achieving desired spectral

characteristics. From what was revealed in this work, it is important to refer that the versatility and variety of controllable parameters are most key features of this type of devices that can shape in various manners its spectral properties. Many facts prove that MMFBGs have broad application prospective and huge marketing potential. Therefore, they resolutely assume an important role in building devices for present and future networks.

In the end we close the whole thesis with a concluding remarks of *Alexander Bell's* well-known saying for mutual encouragement:

“I have heard articulate speech produced by sunlight! I have heard a ray of sun laugh and cough and sing!....Can imagination picture what the future of this invention is to be.”

— Alexander Graham Bell*

February 26, 1880

* In February of 1880 Alexander Graham Bell and Sumner Tainter became the first people to communicate by speech modulated onto a beam of light.

Appendix A

Bessel Functions and Modified Bessel Functions ^[52]

This appendix lists the definitions and some recurrence relations for integer-order Bessel functions of the first kind $J_\nu(z)$ and modified Bessel functions $K_\nu(z)$. Detailed mathematical properties of these and other Bessel functions can be found in Refs. 24 through 26 of Chap. 2. Here, the parameter ν is any integer and n is a positive integer or zero. The parameter $z = x + jy$.

C.1 BESSEL FUNCTIONS OF THE FIRST KIND

C.1.1 Various Definitions

A Bessel function of the first kind of order n and argument z , commonly denoted by $J_n(z)$, is defined by

$$J_n(z) = \frac{1}{2\pi} \int_{-\pi}^{\pi} e^{jz \sin \theta - jn\theta} d\theta$$

or, equivalently,

$$J_n(z) = \frac{1}{\pi} \int_0^{\pi} \cos(z \sin \theta - n\theta) d\theta$$

Just as the trigonometric functions can be expanded in power series, so can the Bessel function $J_\nu(z)$:

$$J_\nu(z) = \sum_{k=0}^{\infty} \frac{(-1)^k (\frac{1}{2}z)^{\nu+2k}}{k!(\nu+k)!}$$

In particular, for $\nu = 0$,

$$J_0(z) = 1 - \frac{z^2}{(1!)^2} + \frac{(\frac{1}{2}z^2)^2}{(2!)^2} - \frac{(\frac{1}{2}z^2)^3}{(3!)^2} + \dots$$

For $\nu = 1$,

$$J_1(z) = \frac{1}{2}z - \frac{(\frac{1}{2}z)^3}{2!} + \frac{(\frac{1}{2}z)^5}{2!3!} - \dots$$

and so on for higher values of ν .

C.1.2 Recurrence Relations

$$J_{\nu-1}(z) + J_{\nu+1}(z) = \frac{2\nu}{z} J_\nu(z)$$

$$J_{\nu-1}(z) - J_{\nu+1}(z) = 2J'_\nu(z)$$

$$J'_\nu(z) = J_{\nu-1}(z) - \frac{\nu}{z} J_\nu(z)$$

$$J'_\nu(z) = -J_{\nu+1}(z) + \frac{\nu}{z} J_\nu(z)$$

$$J'_0(z) = -J_1(z)$$

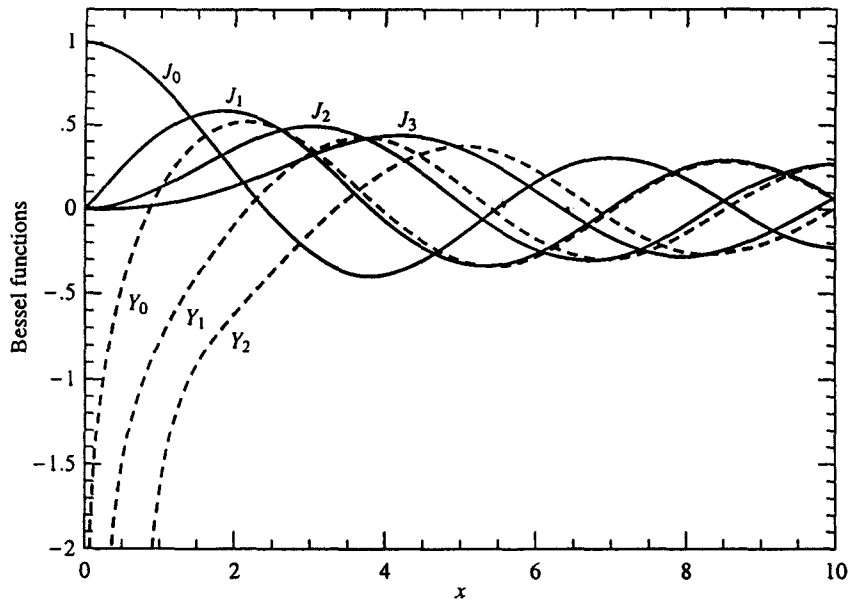


Fig. A-1 Bessel functions $J_0(x)$ through $J_3(x)$ and $Y_0(x)$ through $Y_2(x)$.

C.2 MODIFIED BESSEL FUNCTIONS

C.2.1 Integral Representations

$$K_0(z) = \frac{-1}{\pi} \int_0^\pi e^{\pm z \cos \theta} \{\gamma + \ln(2z \sin^2 \theta)\} d\theta$$

where Euler's constant $\gamma = 0.57722$.

$$K_\nu(z) = \frac{\pi^{1/2} (\frac{1}{2}z)^\nu}{\Gamma(\nu + \frac{1}{2})} \int_0^\infty e^{-z \cosh t} \sinh^{2\nu} t dt$$

$$K_0(x) = \int_0^\infty \cos(x \sinh t) dt = \int_0^\infty \frac{\cos(xt)}{\sqrt{t^2 + 1}} dt \quad (x > 0)$$

$$K_\nu(x) = \sec(\frac{1}{2}\nu\pi) \int_0^\infty \cos(x \sinh t) \cosh(\nu t) dt \quad (x > 0)$$

C.2.2 Recurrence Relations

If $L_\nu = e^{j\nu\pi} K_\nu$, then

$$L_{\nu-1}(z) - L_{\nu+1}(z) = \frac{2\nu}{z} L_\nu(z)$$

$$L'_\nu(z) = L_{\nu-1}(z) - \frac{\nu}{z} L_\nu(z)$$

$$L_{\nu-1}(z) + L_{\nu+1}(z) = 2L'_\nu(z)$$

$$L'_\nu(z) = L_{\nu+1}(z) + \frac{\nu}{z} L_\nu(z)$$

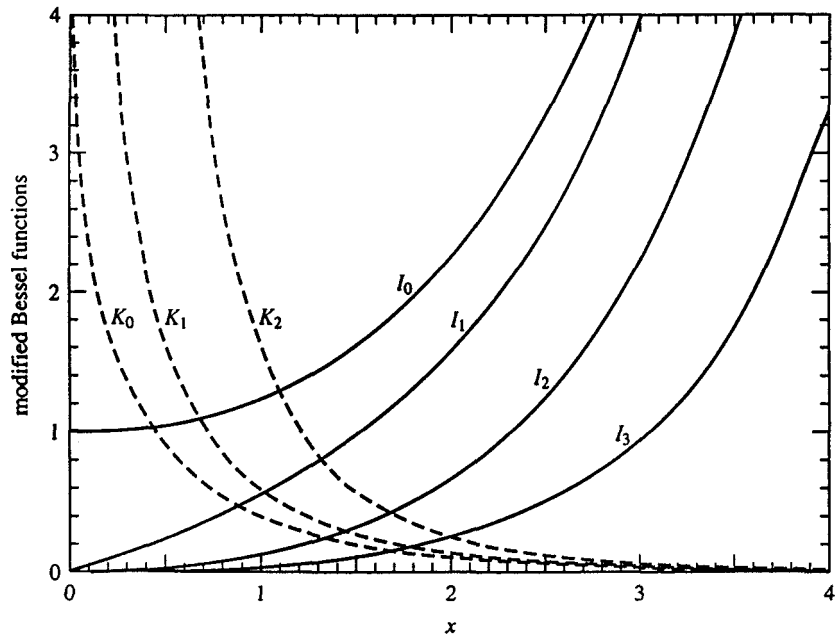


Fig. A-2 Modified Bessel functions $I_0(x)$ through $I_3(x)$ and $K_0(x)$ through $K_2(x)$.

C.3 ASYMPTOTIC EXPANSIONS

For fixed ν ($\neq -1, -2, -3, \dots$) and $z \rightarrow 0$,

$$J_\nu(z) \approx \frac{(\frac{1}{2}z)^\nu}{\Gamma(\nu+1)}$$

For fixed ν and $|z| \rightarrow \infty$,

$$J_\nu(z) \approx \left(\frac{2}{\pi z}\right)^{1/2} \cos\left(z - \frac{\nu\pi}{2} - \frac{\pi}{4}\right)$$

For fixed ν and large $|z|$,

$$K_\nu(z) \approx \left(\frac{\pi}{2z}\right)^{1/2} e^{-z} \left[1 - \frac{\mu-1}{8z} + \frac{(\mu-1)(\mu-9)}{2!(8z)^2} + \dots\right]$$

where $\mu = 4\nu^2$.

C.4 GAMMA FUNCTION

$$\Gamma(z) = \int_0^\infty t^{z-1} e^{-t} dt$$

For integer n ,

$$\Gamma(n+1) = n!$$

For fractional values,

$$\Gamma\left(\frac{1}{2}\right) = \pi^{1/2} = (-\frac{1}{2})! \approx 1.77245$$

$$\Gamma\left(\frac{3}{2}\right) = \frac{1}{2}\pi^{1/2} = (\frac{1}{2})! \approx 0.88623$$

Appendix B

Bracketing and Bisection ^[55]

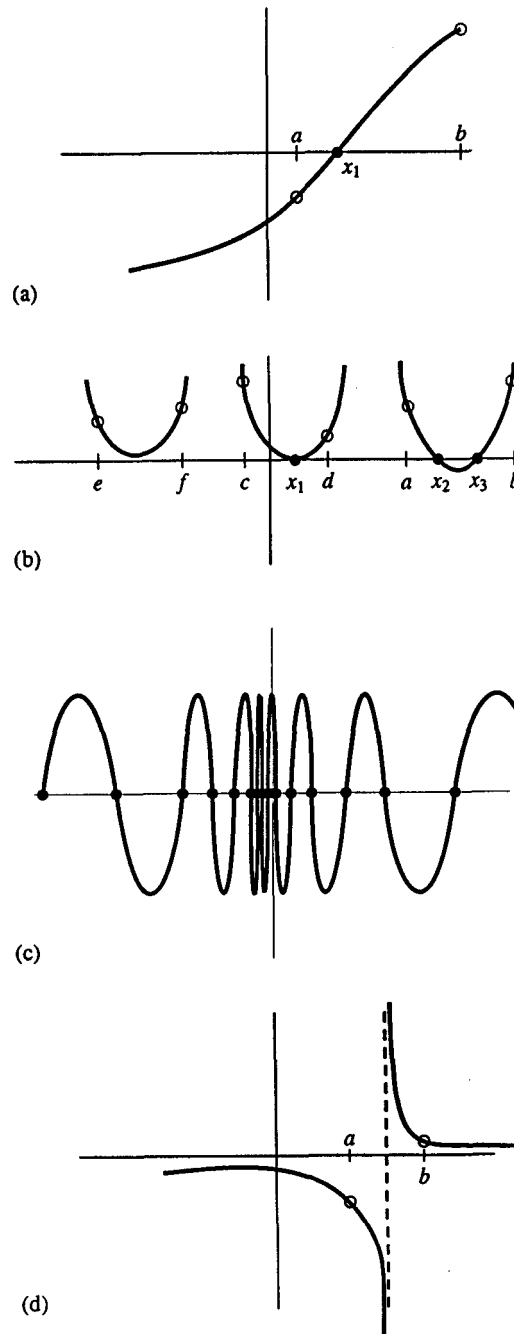


Fig. B-1 Some situations encountered while root finding: (a) an isolated root x_1 bracketed by two points a and b at which the function has opposite signs, (b) not necessarily a sign change in the function near a double root, (c) a pathological function with many roots, and (d) the function has opposite signs at points a and b , but the points bracket a singularity rather than a root.

Appendix C

Normalized Cutoff Frequencies V_c for Various LP_{lm} Modes

Sibackupcalculate5

1.527900000000	0.000011106942	0.000000000062		1
1	0	1	5.900330046954	1.434800000000
1.527900000000	2.443538267185	2.985439631599		2
1	0	1	5.956579616272	1.448478367382
2	1	1	5.901043234742	1.434973427898
1.527900000000	3.887440680057	7.556097520479		4
1	0	1	5.979506660255	1.454053601724
2	0	2	5.900330854598	1.434800196397
3	1	1	5.943694464776	1.445345048531
4	2	1	5.901919992578	1.435186631589
1.527900000000	5.220273676553	13.625628629057		5
1	0	1	5.988721113267	1.456294306409
2	0	2	5.927667553550	1.441447739050
3	1	1	5.965723750429	1.450701972432
4	2	1	5.936408104625	1.443573203657
5	3	1	5.902626211585	1.435358364869
1.527900000000	5.553481925677	15.420580749412		6
1	0	1	5.990214708381	1.456657508171
2	0	2	5.934409816584	1.443087274284
3	1	1	5.969400325285	1.451596015572
4	1	2	5.900647615296	1.434877223995
5	2	1	5.942694512334	1.445101887258
6	3	1	5.911322018859	1.437472948998
1.527900000000	6.442037256675	20.749922008194		7
1	0	1	5.993277495480	1.457402294801
2	0	2	5.948997403525	1.446634579193
3	1	1	5.977004545946	1.453445155488
4	1	2	5.917901429317	1.439072882909
5	2	1	5.955912475371	1.448316136836
6	3	1	5.930579500082	1.442155845351
7	4	1	5.901840989381	1.435167420157
1.527900000000	7.108453754923	25.265057392941		9
1	0	1	5.994951878714	1.457809459323
2	0	2	5.957293540848	1.448651974447
3	0	3	5.900472616949	1.434834669150
4	1	1	5.981192737768	1.454463609977
5	1	2	5.930022969350	1.442020512194
6	2	1	5.963285428358	1.450109038735
7	2	2	5.901866013806	1.435173505418
8	3	1	5.941622855927	1.444841289528
9	4	1	5.916627253897	1.438763038057
1.527900000000	7.663800836797	29.366921633043		10
1	0	1	5.996064749117	1.458080079177
2	0	2	5.962902081070	1.450015819087
3	0	3	5.908406598387	1.436763997930
4	1	1	5.983986532735	1.455142985027
5	1	2	5.938554088761	1.444095048709
6	2	1	5.968231261248	1.451311730953
7	2	2	5.912034096451	1.437646106927
8	3	1	5.949103647613	1.446660414870
9	4	1	5.926885351797	1.441257528831
10	5	1	5.901977798095	1.435200688321
1.527900000000	8.441286751420	35.627661009847		11
1	0	1	5.997307326759	1.458382240308
2	0	2	5.969237460297	1.451556411231
3	0	3	5.921287137093	1.439896195076
4	1	1	5.987114267551	1.455903565177
5	1	2	5.948393147332	1.446487640500
6	2	1	5.973789660836	1.452663382753
7	2	2	5.925074496642	1.440817178044
8	3	1	5.957562104857	1.448717281919
9	3	2	5.900730692159	1.434897426031
10	4	1	5.938615361002	1.444109948454

Sibackupcalculate5

11	5	1	5.917150887976	1.438890371641	
1.527900000000		8.	663425584169	37.527471426218	12
1	0	1	5.997608760174	1.458455540727	
2	0	2	5.970784479275	1.451932604225	
3	0	3	5.924668614427	1.440718478514	
4	1	1	5.987874210922	1.456088362763	
5	1	2	5.950820083072	1.447077805351	
6	1	3	5.900378990923	1.434811901844	
7	2	1	5.975143143075	1.452992512870	
8	2	2	5.928390594952	1.441623563080	
9	3	1	5.959628434284	1.449219757109	
10	3	2	5.904517763436	1.435818338900	
11	4	1	5.941496212594	1.444810493310	
12	5	1	5.920919469040	1.439806788192	
1.527900000000		8.	774495000544	38.495881257285	13
1	0	1	5.997751868442	1.458490340770	
2	0	2	5.971520205170	1.452111512779	
3	0	3	5.926298637602	1.441114855875	
4	1	1	5.988235153347	1.456176134157	
5	1	2	5.951977078195	1.447359155138	
6	1	3	5.901488381730	1.435081675554	
7	2	1	5.975786361480	1.453148926114	
8	2	2	5.929980978760	1.442010301223	
9	3	1	5.960611223898	1.449458744848	
10	3	2	5.906412402540	1.436279063667	
11	4	1	5.942868140691	1.445144108958	
12	5	1	5.922718268233	1.440244207296	
13	6	1	5.900389837767	1.434814539502	
1.527900000000		9.	774119747916	47.766708423303	14
1	0	1	5.998847983684	1.458756886224	
2	0	2	5.977180158104	1.453487859594	
3	0	3	5.939197971438	1.444251623487	
4	1	1	5.991002775268	1.456849144633	
5	1	2	5.960929560312	1.449536155617	
6	1	3	5.916098699698	1.438634508032	
7	2	1	5.980725631110	1.454350022326	
8	2	2	5.942444202815	1.445041018782	
9	3	1	5.968173360309	1.451297651017	
10	3	2	5.922052446137	1.440082297448	
11	4	1	5.953456223690	1.447718843145	
12	4	2	5.900540495880	1.434851175462	
13	5	1	5.936670292426	1.443636960609	
14	6	1	5.917919442842	1.439077263309	
1.527900000000		9.	996258580666	49.962592805766	15
1	0	1	5.999052035924	1.458806506186	
2	0	2	5.978238258095	1.453745160772	
3	0	3	5.941664886660	1.444851510261	
4	1	1	5.991518549130	1.456974566826	
5	1	2	5.962611937504	1.449945264053	
6	1	3	5.919237180735	1.439397701371	
7	2	1	5.981647406044	1.454574172952	
8	2	2	5.944810529405	1.445616445133	
9	3	1	5.969587288065	1.451641479842	
10	3	2	5.925112264779	1.440826362229	
11	4	1	5.955441245918	1.448201546633	
12	4	2	5.904095094240	1.435715557232	
13	5	1	5.939296887205	1.444275677114	
14	6	1	5.921245247846	1.439886008749	
15	7	1	5.901407257334	1.435061948305	
1.527900000000		10.	218397413415	52.207822849244	17
1	0	1	5.999244127044	1.458853217529	
2	0	2	5.979235496532	1.453987662072	
3	0	3	5.944002421193	1.445419935166	

Sibackupcalculate5

4	0	4	5.900346863173	1.434804089248	
5	1	1	5.992004236939	1.457092672909	
6	1	2	5.964199701053	1.450331365021	
7	1	3	5.922253871582	1.440131278645	
8	2	1	5.982515749038	1.454785330382	
9	2	2	5.947049204856	1.446160830195	
10	2	3	5.900835910064	1.434923012168	
11	3	1	5.970919932362	1.451965542737	
12	3	2	5.928022911085	1.441534152351	
13	4	1	5.957313451071	1.448656816072	
14	4	2	5.907566902724	1.436559806752	
15	5	1	5.941776699654	1.444878700144	
16	6	1	5.924390326401	1.440650806425	
17	7	1	5.905255232815	1.435997671421	
1.527900000000		11.106952744413	61.682199633310		19
1	0	1	5.999909955761	1.459015128988	
2	0	2	5.982700276149	1.454830202363	
3	0	3	5.952204578495	1.447414477031	
4	0	4	5.910718150570	1.437326104633	
5	1	1	5.993688779416	1.457502307883	
6	1	2	5.969730745037	1.451676364681	
7	1	3	5.933066283404	1.442760563508	
8	2	1	5.985529833523	1.455518273859	
9	2	2	5.954882542101	1.448065685040	
10	2	3	5.912840865928	1.437842291350	
11	3	1	5.975550289261	1.453091519763	
12	3	2	5.938299843419	1.444033223148	
13	4	1	5.963827248261	1.450240794618	
14	4	2	5.920186825505	1.439628629185	
15	5	1	5.950420685652	1.446980682747	
16	5	2	5.900967347298	1.434954974133	
17	6	1	5.935384650712	1.443324327465	
18	7	1	5.918776234254	1.439285611708	
19	8	1	5.900668924229	1.434882405748	
1.527900000000		11.662299826286	68.004618619099		20
1	0	1	6.000256989103	1.459099518070	
2	0	2	5.984510744566	1.455270459105	
3	0	3	5.956532259062	1.448466851395	
4	0	4	5.917806115804	1.439049705252	
5	1	1	5.994567370758	1.457715957432	
6	1	2	5.972628812984	1.452381096087	
7	1	3	5.938868296338	1.4444171455457	
8	2	1	5.987103189963	1.455900871409	
9	2	2	5.959004802018	1.449068106681	
10	2	3	5.919943336667	1.439569419313	
11	3	1	5.977969911419	1.453679906149	
12	3	2	5.943750925996	1.445358778366	
13	3	3	5.900847860571	1.434925918206	
14	4	1	5.967235759643	1.451069652003	
15	4	2	5.927009308827	1.441287671813	
16	5	1	5.954952278565	1.448082643054	
17	5	2	5.909013116346	1.436911486623	
18	6	1	5.941163788844	1.444729656883	
19	7	1	5.925913861476	1.441021288773	
20	8	1	5.909252604314	1.436969723591	
1.527900000000		11.884438659036	70.619941120192		21
1	0	1	6.000383428863	1.459130264785	
2	0	2	5.985171100295	1.455431039682	
3	0	3	5.958116769600	1.448852161318	
4	0	4	5.920490146924	1.439702388715	
5	1	1	5.994887575751	1.457793822589	
6	1	2	5.973687051487	1.452638430946	
7	1	3	5.941004469574	1.444690914764	

sibackupcalculate5

8	1	4	5.900995700377	1.434961868832	
9	2	1	5.987676810985	1.456040360460	
10	2	2	5.960512609536	1.449434764514	
11	2	3	5.922603926426	1.440216402474	
12	3	1	5.978852460248	1.453894518052	
13	3	2	5.945750391364	1.445844994033	
14	3	3	5.903673485701	1.435613033487	
15	4	1	5.968479700682	1.451372144675	
16	4	2	5.929525666541	1.441899581659	
17	5	1	5.956607300751	1.448485099495	
18	5	2	5.912030595161	1.437645255508	
19	6	1	5.943276546003	1.445243422036	
20	7	1	5.928527067929	1.441656749601	
21	8	1	5.912402840524	1.437735775470	
1.527900000000	12.	328716324535	75.998623105423		22
1	0	1	6.000617642772	1.459187219246	
2	0	2	5.986395289524	1.455728729250	
3	0	3	5.961061855396	1.449568326188	
4	0	4	5.925566402428	1.440936796170	
5	1	1	5.995480843162	1.457938089109	
6	1	2	5.975650398197	1.453115863537	
7	1	3	5.944988834482	1.445659804085	
8	1	4	5.905956847553	1.436168285068	
9	2	1	5.988739876436	1.456298869102	
10	2	2	5.963313271912	1.450115809531	
11	2	3	5.927611546210	1.441434119587	
12	3	1	5.980488563676	1.454292373965	
13	3	2	5.949471077158	1.446749763755	
14	3	3	5.909365945482	1.436997285085	
15	4	1	5.970786671845	1.451933137399	
16	4	2	5.934223691279	1.443042013665	
17	5	1	5.959678188786	1.449231856053	
18	5	2	5.917708450023	1.439025955586	
19	6	1	5.947199371298	1.446197346595	
20	7	1	5.933383626845	1.442837732813	
21	8	1	5.918265839671	1.439161497609	
22	9	1	5.901888504787	1.435178974614	
1.527900000000	12.	439785740909	77.374134639866		23
1	0	1	6.000672603929	1.459200584307	
2	0	2	5.986682735532	1.455798628311	
3	0	3	5.961754734836	1.449736815648	
4	0	4	5.926774387051	1.441230545219	
5	1	1	5.995620083900	1.457971948674	
6	1	2	5.9761111680132	1.453228034774	
7	1	3	5.945928578267	1.445888324248	
8	1	4	5.907288906530	1.436492205629	
9	2	1	5.988989429469	1.456359553622	
10	2	2	5.963971848636	1.450275957502	
11	2	3	5.928799673338	1.441723039832	
12	3	1	5.980872729570	1.454385792676	
13	3	2	5.950347168233	1.446962805307	
14	3	3	5.910755521412	1.437335192207	
15	4	1	5.971328522758	1.452064900823	
16	4	2	5.935332469223	1.443311638344	
17	5	1	5.960399737162	1.449407317019	
18	5	2	5.919055131277	1.439353431888	
19	6	1	5.948121549343	1.446421595247	
20	6	2	5.901748957021	1.435145040387	
21	7	1	5.934526080507	1.443115546512	
22	8	1	5.919646428838	1.439497219394	
23	9	1	5.903522111277	1.435576223339	
1.527900000000	13.	106202239158	85.886268566850		24
1	0	1	6.000975615966	1.459274268603	

Sibackupcalculate5

2	0	2	5.988268619719	1.456184272269
3	0	3	5.965585958957	1.450668465289
4	0	4	5.933528024471	1.442872846394
5	1	1	5.996387898361	1.458158660296
6	1	2	5.978658413886	1.453847331247
7	1	3	5.951138751098	1.447155296759
8	1	4	5.915135245228	1.438400222075
9	2	1	5.990365861953	1.456694264614
10	2	2	5.967611397091	1.451160996827
11	2	3	5.935424750152	1.443334078560
12	3	1	5.982992227646	1.454901197037
13	3	2	5.955195848244	1.448141872584
14	3	3	5.918656501350	1.439256495918
15	4	1	5.974319015004	1.452792107308
16	4	2	5.941483609864	1.444807428668
17	4	3	5.901433721674	1.435068383713
18	5	1	5.964383683025	1.450376104439
19	5	2	5.926560542056	1.441178543924
20	6	1	5.953216033887	1.447660435509
21	6	2	5.910554038674	1.437286197078
22	7	1	5.940842067485	1.444651422987
23	8	1	5.927286830726	1.441355157601
24	9	1	5.912577424446	1.437778229537

References

1. L. Martinage, Next-Generation Metro DWDM Networks, *Fiberoptic Product News*, 17, August 2000.
2. C. R. Giles, "Lightwave Applications of Fiber Bragg Gratings", *Journal of Lightwave Technology*, Vol. 15, No. 8, August 1997.
3. Ajoy Ghatak, K. Thyagarajan, *Introduction to Fiber Optics*, Cambridge University Press.
4. A. Othonos, "Fiber Bragg gratings", *Rev. Sci. Instrum.*, Vol. 68, pp. 4309-4341, Dec. 1997.
5. Jinping Wen, *Introduction of Fiber Gratings*, Final Report for ENEE 785B.
6. G. Meltz, W. W. Morey, and W. H. Glenn, "Formation of Bragg gratings in optical fibers by a transverse holographic method", *Opt.Lett.*, Vol. 14, pp.823-825, Aug. 1989.
7. T. Szkopek, V. Pasupathy, J. E. Sipe, and P. W. E. Smith, "Novel multimode fiber for narrow-band Bragg gratings", *IEEE Journal on Selected Topics in Quantum Electronics*, Vol. 7, No. 3, May/June, 2001.
8. T. Mizunami, T. V. Djambova, T. Niiho, and S. Gupta, "Bragg gratings in multimode and few-mode optical fibers", *Journal of Lightwave Technology*, Vol. 18, No. 2, pp. 230-235, 2000.
9. J. Lim, Q. P. Yang, B. E. Jones and P. R. Jackson, "DP Flow Sensor Using Optical Fiber Bragg Gratings", *Proc. EurosensorsXIV, the 14th European Conference on Solid-State Transducers*, Copenhagen, 2000, pp. 845-848.
10. Lim, P. R. Jackson, B. E. Jones, K. F. Hale and Q. P. Yang, "An Intrinsically Safe Optically Powered Hydraulic Valve", *Proc. 7th Int. Conference on Actuators2000*, Bremen, 2000, pp. 216-219.
11. J. Lim, Q. P. Yang, B. E. Jones and P. R. Jackson, "Strain and Temperature Sensors Using Multimode Optical Fiber Bragg Gratings and Correlation Signal Processing", *IEEE Instrumentation and Measurement Technology Conference*,

Budapest, Hungary, May 21-23, 2001.

12. K.H. Wanser, K. F. Voss and A. D. Kersey, "Novel fiber devices and sensors based on multimode fiber Bragg gratings", Proc. SPIE, Vol. 2360, pp. 265-268, 1994.
13. T. Mizunami, S. Gupta, T. Yamao, and T. Shimomura, "Multimode fiber Bragg gratings—Spectral characteristics and applications", Int. Conf. Integrated Optics Optical Fiber Commun./Eur. Conf. Optical Communication, Vol. 3, Sept. pp. 182-185, 1997.
14. S. Okude, M. Sudoh, K. Shima, T. Sakai, A. Wada, and R. Yamauchi, "A novel technique for suppressing undesired coupling of LP₀₁ Mode to cladding modes in fiber Bragg gratings", Tech. Dig. 11th Int. Conf. Optical Fiber Sensors, Sapporo, Japan, May, pp. 380-383, 1996.
15. N. J. Vasa, P. Husayin, M. Kidosaki, T. Okada, M. Maeda, and T. Mizunami, "Fiber grating butt-coupled cw Cr³⁺: LiSrAlF₆ Laser performance", Tech. Dig. Conf. Lasers Electro-Optics, San Francisco, CA, May, pp. 67-68, 1998.
16. http://www.crc.ca/en/html/crc/home/tech_transfer/bragg.
17. Andreas Othonos, Kyriacos Kalli, Fiber Bragg Gratings – Fundamentals and Applications in Telecommunications and Sensing, Artech House, Boston, London, 1999.
18. K.O. Hill, B. Malo, F. Bilodeau, and D.C. Johnson, "Photosensitivity in Optical Fibers," Ann. Rev. Mat. Sci., Vol. 23, 1993.
19. I. Bennion, J.A.R. Williams, L. Zhang, et al., "UV-written in-fiber Bragg Gratings," Optical and Quantum Electronics 28, 1996.
20. Lam. D. K. W., Garside. B. K., 1981, Appl. Opt. 20: 440-45.
21. Parent. M., Bures. J., Lacroix. S., Lapieere. J., 1985, Appl. Opt., 24: 354-57.
22. Meltz. G., Morey. W. W., Glenn. W. H., Farina. J. D., 1988, Proc. OFC'88, Pap. ThBB5-1, pp. 163-66.
23. Hill, K. O., et al. "Bragg Gratings Fabricated in Monomode Photosensitive Optical Fiber by UV Exposure through a Phase Mask", Applied Physics Letters, Vol. 62, 1993, pp. 1035-1037.

24. Anderson, D. Z., et al., "Production of in-fiber Gratings Using a Diffractive Optical Element", *Electronics Letters*, Vol. 29, 1993, pp. 566-568.
25. Fujiwara T., Wong D., and Fleming S., "Large Electro-Optic Modulation in a Thermally poled Germanosilicate Fiber", *IEEE Photon. Technol. Lett.* 7(10), 1177-1179 (1995).
26. Fujiwara T., Takahashi M., and Ikushima A. J., "Second Harmonic Generation in Germanosilicate glass poled with ArF Laser Irradiation", *Appl. Phys. Lett.* 71(8), 1032-1034 (1997).
27. T. Erdogan, "Fiber grating spectra", *Journal of Lightwave Technology*, Vol. 15, No. 8, Aug. 1997.
28. A. Othonos, A. T. Alavie, S. Melle, S. E. Karr, and R. M. Measures, *Opt. Eng.* (Bellingham) 32, 2841 (1993).
29. A. D. Kersey and W. W. Morey, *Electron. Lett.* 29, 112 (1993).
30. A. T. Alavie, S. E. Karr, A. Othonos, and R. M. Measures, *IEEE Photonics Technol. Lett.* 5, 1112 (1993).
31. T. Erdogan and J. E. Sipe, "Tilted fiber phase gratings", *J. Opt. Soc. Amer. A*, Vol. 13, pp. 296-313, 1996.
32. Snyder A. W. and Love J. D., in *Optical Waveguide Theory*, Chapman-Hall, London, 1983.
33. A Arraf, CM de Sterke, L Poladian and TG Brown, Effective-medium approach for counterpropagating waves in nonuniform Bragg gratings, *Journal of the Optical Society of America A*, 14, 1137 - 1143, 1997.
34. Skaar Johannes, "Synthesis and Characterization of Fiber Bragg Gratings", 2000.
35. Yariv A., in *Optical Electronics*, 4th ed., Saunders College Publishing (1991).
36. Kenneth O. Hill and Gerald Meltz, "Fiber Bragg Grating Technology Fundamentals and Overview," *Journal of Lightwave Technology*, Vol. 15, No. 8, August 1997.
37. J. L. Zyskind, J. W. Sulhoff, P. D. Magill, K. C. Reichmann, V. Mizrahi, and D. J. DiGiovanni, "Transmission at 2.5Gbit/s over 654 km Using an Erbium-doped Fiber Grating Laser Source", *Electron. Lett.*, Vol. 29, No. 12, p. 1105, 1993.

38. J. T. Keinglebotn, P. R. Morkel, L. Reekie, J. L. Archambault, and D. N. Payne, "Efficient Diod-Pumped Single Frequency Erbium: Ytterbium Fiber Lasers", *IEEE Photon. Technol. Lett.*, Vol. 5, p. 1162, Oct. 1993.
39. C. R. Giles and V. Mizrahi, "Single-Frequency 1559 nm Erbium-Doped Fiber Lasers Pumped by a 650 nm Semiconductor Laser", *Appl. Opt.*
40. C. R. Giles, J. Stone, L. W. Stulz, K. Walker, and C. A. Burrus, "Gain Enhancement in Reflected-Pump Erbium-Doped Fiber Amplifiers", in *Tech. Dig. Optic. Amplifiers and Their Applications*, 1991, Vol. 13, paper ThD2, pp. 148-151.
41. R. J. Nuyt, Y. K. Park, and P. Gallion, "Dispersion Equalization of a 10 Gb/s Repeated Transmission System Using Dispersion Compensating Fiber", *J. Lightwave Technol.*, Vol. 15, pp. 31-42, Jan., 1997.
42. Mizrahi, V., T. Erdogan, D. J. DiGiovanni, P.J. Lemaire, W. M. MacDonald, S. G. Kosinski, S. Cabot, and J. E. Sipe. 1994, Four Channel Fibre Grating Demultiplexer, *Electron. Lett.* 30: 780-781.
43. C. R. Giles, R. D. Feldman, T. H. Wood, M. Zirngibl, G. Raybon, et al, "Access PON Using Downstream 1550-nm WDM Routing and Upstream 1300-nm SCMA Combining through a Fiber-Grating Router", *IEEE Photon. Technol. Lett.*, Vol. 8, pp. 1549-1551, Nov. 1996.
44. W. W. Morey, G. Meltz, et al, "Mode-Coupling Characterization of UV-written Bragg Gratings in Depressed-Cladding Fiber", *Electron. Lett.*, Vol 30, pp. 730-731, 1994.
45. T. A. Strasser, J. R. Pedrazzani, et al., "Reflective-Mode Conversion UV-Induced Phase Grating in Two-Mode Fiber", in *Conf. Optic. Fiber Commun., OFC'97*, 1997. *OSA Tech. Dig.*, paper FB3, Vol. 6, pp. 348-349.
46. K. O. Hill, F. Bilodeau, et al., "Birefringent Photosensitivity in Monomode Optical Fiber: Application to the External Writing of Rocking Filters", *Electron. Lett.*, Vol. 27, pp. 1548-1550, 1991.
47. B. Malo, F. Bilodeau, et al., "Rocking Filter Written in Photosensitive Birefringent Fiber: Suppression of Sidelobes in Filter Wavelength Response", in

Conf. Optic. Fiber Commun. OFC'92, 1992, OSA Tech. Dig. Vol. 5, postdeadline paper PD23, pp. 404-407.

48. A. D. Kersey, "A Review of recent Developments in Fiber Optic Sensor Technology", Optic. Fiber. Technol. Vol. 2, pp. 291-317, 1996.

49. G. Meltz, "Overview of Fiber Grating-Based Sensors", in Proc. SPIE. Distributed and Multiplexed Sensors VI, 1996, Vol. SPIE-2838, pp. 22-23.

50. A. D. Kersey, M. A. Davis, et al., "Progress toward the Development of Practical Fiber Bragg Grating Instrumentation Systems", in Proc. SPIE. Fiber. Optic. And Laser Sensors, XIV, 1996, Vol. SPIE-2839, pp. 40-64.

51. Bahaa E. A. Saleh, Malvin Carl Teich, Fundamentals of Photonics, A Wiley-Interscience Publication, John Wiley & Sons, Inc.

52. Gerd Keiser, Optical Fiber Communications, 3rd ed., McGraw-Hill Higher Education, 2000.

53. Ajoy Ghatak, K. Thyagarajan, Introduction to Fiber Optics, Cambridge University Press.

54. Dietrich Marcuse, Theory of Dielectric Optical Waveguides, Second Edition, Academic Press, Inc., 1991.

55. Robert D. Walker, Numerical Methods for Engineers and Scientists, TAB Professional and Reference Books, 1987. (including numerical recipes).

56. Jinsong Zhang, Fiber Bragg Gratings in Multimode Structure, Report of EE750.

57. Libo Fan, Farhad Ansari, "Fiber-Optic Bragg Grating Principle and Its Applications (I)", Optical Communication Technology, Vol. 22, No. 1, 1996.

58. A. Yariv: IEEE J. QE-9, 919, 1973.

59. Kogelnik H. and Shank C. W., 'Coupled Wave Theory of Distributed Feedback Lasers', J. Appl. Phys. 43, 2327-2335, 1978.

60. Gloge D., "Weakly Guiding Fibers", Appl. Opt. 10(10), 2252-2258, 1971.

61. Raman Kashyap: Fiber Bragg Gratings, Academic Press, 1999.

62. Kogelnik H., "Coupled Wave Theory for Thick Holograms", Bell Syst. Tech. J. 48(9), 2909-2947, 1969.

63. Hermann A. Haus and Weiping Huang, "Coupled-Mode Theory", Proceedings of The IEEE, Vol. 79, No. 10, Oct. 1991.
64. Genxiang Chen, et al.: Optical Fiber Communication Techniques.
65. Laurene V. Fausett, Applied Numerical Analysis Using MATLAB, Prentice Hall.
66. Robert J. Schilling, Sandra L. Harris, Applied Numerical Methods for Engineers, Brooks/Coles Thomson Learning.
67. Paul F. Hultquist, Numerical Methods for Engineers and Computer Scientists, The Benjamin/Cummings Publishing Company, Inc.
68. Edward R. Champion, Jr., Numerical Methods for Engineering Applications, Marcel Dekker, Inc.
69. C. Pask, J. Opt. Soc. Am., 68, (1978), pp. 572.
70. J. E. Sipe, L. Poladian, et al., "Propagation through Nonuniform Grating Structures", J. Opt. Soc. Amer. A. Vol. 11, pp. 1307-1320, 1994.
71. V. Mizrahi and J. E. Sipe, "Optical Properties of Photosensitive Fiber Phase Gratings", J. Lightwave Technol., Vol. 11, pp. 1513-1517, 1993.
72. T. Erdogan, "Cladding-Mode Resonances in Short and Long Period Fiber Grating Filters", J. Opt. Soc. Amer. A, Vol. 14, No. 8, Aug. 1997.
73. D. Golge, "Optical Power Flow in Multimode Fibers", Bell Syst. Tech. J. Vol. 51, pp. 1767-1783, 1972.
74. D. B. Kect, "Spatial and Temporal Power Transfer Measurements on a Low-loss Optical Waveguide", Appl. Opt. Vol. 13, pp. 1882-1888, 1974.
75. M. Tateda and M. Ikeda, "Mode Conversion in Bent Step-Index Multimode Fiber", Appl. Opt. Vol. 15, pp. 2308-2310, 1976.
76. R. Olshansky, S. M. Oakes, D. B. Kect, "Measurement of Differential Mode Attenuation in Graded-Index Fiber Optical Waveguides", Presented at the Topic Meeting on optical Fiber Transmission II, Williamsburg, VA. TuE5-1, 1977.
77. R. Olshansky, S. M. Oakes, "Differential Mode Attenuation Measurements in Graded-Index Fibers", Appl. Opt. Vol. 17, pp. 1830-1835, 1978.
78. H. Kawazoe, Y. Watanabe, et al., Mater. Res. Soc. Symp. Proc. 61, 350 (1986).
79. T. E. Tsai and D. L. Griscom, Proc. SPIE 1516, 14 (1991).

80. K. O. Hill, Y. Fujii, et al., "Photosensitivity in Optical Fiber Waveguides: Application to Reflection Filter Fabrication", *Appl. Phys. Lett.* Vol. 32, pp.647-649, 1978.
81. B. Poumellec, P. Niay, et al., "The UV-Induced Reflective Index Grating in Ge:SiO₂ Preforms: Additional CW Experiments and the Microscopic Origin of the Change in Index", *J. Phys. D. Appl. Phys.* Vol. 29, pp. 1842-1856, 1996.
82. F. Bilodeau, B. Malo, et al., "Photosensitization of Optical Fiber and Silica-on-Silicon/Silica Waveguides", *Opt. Lett.* Vol. 18, pp. 953-955, 1993.
83. T. Mizunami, T. Niiho, et al., "Multimode Fiber Bragg Gratings for Fiber Optic Bending Sensors", *Proc. SPIE*, Vol. 3746, pp. 216-219, April, 1999.
84. T. V. Djambova and T. Mizunami, "Simultaneous Sensing of the Temperature and Displacement Using a Multimode Fiber Bragg Grating", *Japanese Journal of Applied Physics*, Vol. 39, 2000, pp. 1566-1570.
85. G. E. Shtengel, R. F. Kazarinov, L.E. Eng, "Simultaneous Laser Wavelength Locking and Spectral Filtering Using Fiber Bragg Grating", (0-7803-4223-2), 1998 IEEE.

FINISHED PAPERS SUBMITTED FOR PUBLICATIONS

1. Jinsong Zhang, Honggang Yu, Changqing Xu, and Weiping Huang, "Multimode Optical Fiber Bragg Gratings: Modeling, Simulation, and Experiments", Accepted by the International Society for Optical Engineering – SPIE Photonics North 2004. SPIE Paper Number: #5579B-64.